

# A Submillimeter Perspective on the GOODS Fields (SUPER GOODS). III. A Large Sample of ALMA Sources in the GOODS-S

L. L. COWIE,<sup>1</sup> J. GONZÁLEZ-LÓPEZ,<sup>2,3</sup> A. J. BARGER,<sup>4,5,1</sup> F. E. BAUER,<sup>3,6,7</sup> L.-Y. HSU,<sup>1</sup> AND W.-H. WANG<sup>8</sup>

<sup>1</sup>*Institute for Astronomy, University of Hawaii, 2680 Woodlawn Drive, Honolulu, HI 96822, USA*

<sup>2</sup>*Núcleo de Astronomía de la Facultad de Ingeniería y Ciencias, Universidad Diego Portales, Av. Ejército Libertador 441, Santiago, Chile*

<sup>3</sup>*Instituto de Astrofísica and Centro de Astroingeniería, Facultad de Física, Pontificia Universidad Católica de Chile, Casilla 306, Santiago 22, Chile*

<sup>4</sup>*Department of Astronomy, University of Wisconsin-Madison, 475 N. Charter Street, Madison, WI 53706, USA*

<sup>5</sup>*Department of Physics and Astronomy, University of Hawaii, 2505 Correa Road, Honolulu, HI 96822, USA*

<sup>6</sup>*Millennium Institute of Astrophysics (MAS), Nuncio Monseñor Sótero Sanz 100, Providencia, Santiago, Chile*

<sup>7</sup>*Space Science Institute, 4750 Walnut Street, Suite 205, Boulder, Colorado 80301, USA*

<sup>8</sup>*Academia Sinica Institute of Astronomy and Astrophysics, P.O. Box 23-141, Taipei 10617, Taiwan*

## ABSTRACT

We analyze the  $> 4\sigma$  sources in the most sensitive 100 arcmin<sup>2</sup> area (rms  $< 0.56$  mJy) of a SCUBA-2 850  $\mu\text{m}$  survey of the GOODS-S and present the 75 band 7 ALMA sources ( $> 4.5\sigma$ ) obtained from high-resolution interferometric follow-up observations. The SCUBA-2—and hence ALMA—samples should be complete to 2.25 mJy. Of the 53 SCUBA-2 sources in this complete sample, only five have no ALMA detections, while 13% (68% confidence range 7–19%) have multiple ALMA counterparts. Color-based high-redshift dusty galaxy selection techniques find at most 55% of the total ALMA sample. In addition to using literature spectroscopic and optical/NIR photometric redshifts, we estimate FIR photometric redshifts based on an Arp 220 template. We identify seven  $z \gtrsim 4$  candidates. We see the expected decline with redshift of the 4.5  $\mu\text{m}$  and 24  $\mu\text{m}$  to 850  $\mu\text{m}$  flux ratios, confirming these as good diagnostics of  $z \gtrsim 4$  candidates. We visually classify 52 ALMA sources, finding 44% (68% confidence range 35–53%) to be apparent mergers. We calculate rest-frame 2–8 keV and 8–28 keV luminosities using the 7 Ms *Chandra* X-ray image. Nearly all of the ALMA sources detected at 0.5–2 keV are consistent with a known X-ray luminosity to 850  $\mu\text{m}$  flux relation for star-forming galaxies, while most of those detected at 2–7 keV are moderate luminosity AGNs that lie just above the 2–7 keV detection threshold. The latter largely have substantial obscurations of  $\log N_H = 23 - 24 \text{ cm}^{-2}$ , but two of the high-redshift candidates may even be Compton thick.

*Keywords:* cosmology: observations — galaxies: distances and redshifts — galaxies: evolution — galaxies: starburst

## 1. INTRODUCTION

Deep imaging with the Submillimeter Common-User Bolometer Array (SCUBA; Holland et al. 1999) on the 15 m James Clerk Maxwell Telescope (JCMT) revolutionized studies of the distant universe by revealing the presence of distant, dusty, extremely luminous galaxies (e.g., Smail et al. 1997; Barger et al. 1998; Hughes et al. 1998; Eales et al. 1999). These so-called submillimeter galaxies (SMGs; see Casey et al. 2014 for a review) are some of the most powerfully star-forming galaxies in the universe and are significant contributors to the total star formation history from  $z \sim 2$  to at least  $z \sim 5$  (Barger et al. 2000, 2012, 2014; Chapman et al. 2005; Wardlow et al. 2011; Casey et al. 2013; Swinbank et al. 2014; Cowie et al. 2017).

SMGs have subsequently been detected by a wide range of single-dish submillimeter and millimeter cam-

eras and telescopes. The second generation camera SCUBA-2 (Holland et al. 2013) is by far the most powerful of these, covering 50 arcmin<sup>2</sup> per pointing (16 times larger than SCUBA) with a sensitivity 5 times fainter than the Large APEX BOLometer CAMERA (LABOCA; Siringo et al. 2009) on the 12 m Atacama Pathfinder Experiment (APEX). The angular resolution on the sky of SCUBA-2 ( $\sim 14''$  FWHM PSF at 850  $\mu\text{m}$ ) is also much better than that of LABOCA ( $\sim 19''$  at 870  $\mu\text{m}$ ), or than that of the space-based *Herschel* ( $\sim 35''$  at 500  $\mu\text{m}$ ) and *Planck* ( $\sim 4.8'$  at 850  $\mu\text{m}$ ) satellites, yielding more accurate positions and suffering less source blending. The natural limit of single-dish submillimeter observations is the depth at which confusion—the blending of sources and/or where the noise is dominated by unresolved contributions from fainter sources—becomes important.

The lack of positional accuracy is a major concern when trying to determine the properties of SMGs. His-

torically, moderately deep radio interferometric images were used to identify counterparts (e.g., Barger et al. 2000; Ivison et al. 2002; Chapman et al. 2003). Using the deepest Karl G. Jansky Very Large Array (VLA) 1.4 GHz image of the sky (11.5  $\mu\text{Jy}$  at  $5\sigma$ ; Owen 2018), Cowie et al. (2017) showed that 75% of the 154 SCUBA-2 sources with 850  $\mu\text{m}$  fluxes  $> 2$  mJy in the Great Observatories Origins Deep Survey-North field (GOODS-N; Giavalisco et al. 2004) had one or more radio counterparts (66% had single radio counterparts); however, 39 had no viable radio counterparts at all within the match radius.

Millimeter/submillimeter interferometry with the IRAM Plateau de Bure Interferometer, the Submillimeter Array (SMA; Ho et al. 2004), and now the Atacama Large Millimeter/submillimeter Array (ALMA) have become essential tools for obtaining precise positions and resolving single-dish submillimeter sources into multiple SMG counterparts (e.g., Wang et al. 2011; Barger et al. 2012, 2014; Smolčić et al. 2012; Chen et al. 2013; Karim et al. 2013; Hodge et al. 2013; Miettinen et al. 2015; Simpson et al. 2015). Even SCUBA-2’s angular resolution at 450  $\mu\text{m}$  ( $\sim 7''$  FWHM PSF) is insufficient for making accurate counterpart identifications at other wavelengths, yet such identifications are critical for estimating photometric redshifts, modeling spectral energy distributions (SEDs), and determining basic properties.

Fully mapping the SMG population requires a “wedding cake” approach. The bottom layer of the cake corresponds to the most wide-field (and shallowest) submillimeter surveys (e.g., South Pole Telescope, *Herschel*, *Planck*). Because these surveys primarily trace the most extreme (and rare) star-forming galaxies in the universe, they are intriguing for probing the upper bound of parameter space. However, they generally lie at a characteristic star formation rate (SFR) limit of  $\sim 1000 M_{\odot} \text{yr}^{-1}$  above which galaxies become quite rare (Karim et al. 2013; Barger et al. 2014).

Thus, to assess how “typical” massive galaxy formation occurs, it is critical to characterize fainter SMGs (defined here as sources with 850  $\mu\text{m}$  fluxes  $\sim 2\text{--}5$  mJy), which comprise the knee of the luminosity distribution and produce 20–30% of the extragalactic background light (EBL) at this wavelength. This middle layer of the wedding cake is best probed by SCUBA-2 surveys, which can find sources down to the JCMT confusion limit of  $\sim 1.65$  mJy at 850  $\mu\text{m}$  (Cowie et al. 2017). This corresponds to SFRs  $\gtrsim 220 M_{\odot} \text{yr}^{-1}$  over  $z = 1 - 8$  for a Kroupa (2001) initial mass function (IMF) and an Arp 220 template. At these fluxes, the SFRs are higher than found in any extinction-corrected UV-selected sample (Reddy & Steidel 2009; van der Burg et al. 2010). Thus, one can only discover these galaxies with submillimeter observations (Barger et al. 2014; Cowie et al. 2017). Moreover, with a sky density of only  $\sim 1$  per 1 arcmin<sup>2</sup> at 2 mJy (e.g., Hsu et al. 2016), the most efficient approach to studying these galaxies in detail

is by targeting single-dish discovered SMGs with small field-of-view interferometers like ALMA, rather than by direct ALMA imaging searches.

Finally, the deepest but smallest area component—the top layer of the wedding cake—comes from direct submillimeter interferometric imaging surveys (e.g., Aravena et al. 2016; Hatsukade et al. 2016; Dunlop et al. 2017; Ueda et al. 2017). Such observations are best suited to probing the faintest SMGs, which begin to overlap with UV-selected samples.

We are writing a series of papers on our deep SCUBA-2 observations of the GOODS fields, which we call the SUBmillimeter PERspective on the GOODS fields (SUPER GOODS) series. In the first two papers in the series (Cowie et al. 2017 or Paper I, and Barger et al. 2017 or Paper II), we presented our SCUBA-2 observations of the GOODS-N/CANDELS/*Chandra* Deep Field-North (CDF-N) complemented with targeted SMA submillimeter interferometry, Karl G. Jansky Very Large Array (VLA) radio interferometry, and *Herschel* imaging.

In this third paper in the series, we present our SCUBA-2 observations of the GOODS-S/CANDELS/*Chandra* Deep Field-South (CDF-S) complemented with targeted ALMA observations and *Herschel* imaging. We made observations with SCUBA-2 to near the confusion limit for a  $4\sigma$  detection. This sample represents an order of magnitude increase in the surface density of sources compared to the wider and shallower LABOCA LESS survey (Weiß et al. 2009) and provides the deepest SMG sample that can be generated with single-dish submillimeter telescope observations of blank fields. In ALMA Cycles 3 and 4, we targeted our SCUBA-2 850  $\mu\text{m}$  sample with band 7 observations. The SCUBA-2 sample contains an unbiased, complete sample to 2.25 mJy, which means the ALMA sample above that flux should be as well, since the SCUBA-2 fluxes are upwardly Eddington biased and may also be composed of blends; thus, the ALMA fluxes are expected to be lower relative to the SCUBA-2 fluxes.

We chose the GOODS-S field due to the unparalleled breadth and depth of the multiwavelength ancillary coverage (e.g., see Guo et al. 2013, hereafter G13, for a detailed summary of the imaging data). Our SCUBA-2 region boasts deep ground-based coverage in  $U'UBVRIzYJHK_s$  plus many medium and narrowbands (e.g., Hildebrandt et al. 2006; Nonino et al. 2009; Cardamone et al. 2010; Retzlaff et al. 2010; Hsieh et al. 2012; Fontana et al. 2014; Straatman et al. 2016, hereafter S16); deep *HST* imaging from GOODS-S (Giavalisco et al. 2004), CANDELS (Grogin et al. 2011; Koekemoer et al. 2011), HUDF (e.g., Beckwith et al. 2006; Koekemoer et al. 2013; Teplitz et al. 2013), HDUV (Oesch et al. 2015), and ERS (Windhorst et al. 2011); ultradeep *Spitzer* (3.6–70  $\mu\text{m}$ , e.g., Magnelli et al. 2011; Ashby et al. 2015) and *Herschel* (100–500  $\mu\text{m}$ , Elbaz et al. 2011; Oliver et al. 2012; Magnelli et al. 2013) imaging; hundreds of hours of VLT and Keck multiobject

spectroscopy (e.g., Szokoly et al. 2004; Le Fèvre et al. 2005; Popesso et al. 2009; Treister et al. 2009; Balestra et al. 2010; Silverman et al. 2010; Cooper et al. 2012; Suh et al. 2015) plus 3D-HST (Brammer et al. 2012; Momcheva et al. 2016) for redshifts of many 1000s of galaxies; and photometric redshift estimates from multiple codes and template SED sets (e.g., Santini et al. 2009, 2015; Rafferty et al. 2011; Dahlen et al. 2013; Hsu et al. 2014; Skelton et al. 2014; S16). Such extensive coverage allows immediate characterization of ALMA-detected sources with sufficient sensitivity to constrain tightly the dust SEDs (da Cunha et al. 2015; Scoville et al. 2016).

In addition, the SCUBA-2 data are well-matched to the deepest portion of the deepest X-ray image ever taken, the 7 Ms *Chandra* exposure (Luo et al. 2017). These unique X-ray data make it possible for us to investigate the SFR versus X-ray luminosity relation for SMGs and to see which of the SMGs contain active galactic nuclei (AGNs).

In Section 2, we describe the SCUBA-2 observations and reductions, construct the SCUBA-2 source catalog, and compare with previous single-dish observations. We also present the ALMA observations and reductions, construct the ALMA source catalog, and compare with the Franco et al. (2018, hereafter, F18) ALMA 1.13 mm observations. In Section 3, we compare the SCUBA-2 and ALMA fluxes, astrometry, and relative positional offsets, and we determine the fraction of SCUBA-2 sources with multiple ALMA counterparts. In Section 4, we describe the ancillary data and identify multiwavelength counterparts to the ALMA sources. We search the literature for optical/NIR spectroscopic and photometric redshifts, which we critically assess. We examine how well various color-based selections proposed in the literature do at finding high-redshift dusty galaxies. We estimate FIR photometric redshifts, which we compare with the spectroscopic and photometric redshifts. Finally, we show that the  $4.5 \mu\text{m}$  and  $24 \mu\text{m}$  to  $850 \mu\text{m}$  flux ratios drop rapidly with increasing redshift. In Section 5, we tabulate candidate high-redshift ( $z > 4$ ) sources. In Section 6, we study the flux dependence of the redshifts and construct the star formation history. In Section 7, we visually inspect the morphologies and merger properties of all ALMA counterparts that are bright enough to do this. In Section 8, we calculate the X-ray luminosities, examine whether the origin of the X-ray emission is predominantly due to AGN activity or star formation, and use the X-ray photon indices to determine the column densities. In Section 9, we summarize our results.

We assume the Wilkinson Microwave Anisotropy Probe cosmology of  $H_0 = 70.5 \text{ km s}^{-1} \text{ Mpc}^{-1}$ ,  $\Omega_M = 0.27$ , and  $\Omega_\Lambda = 0.73$  (Larson et al. 2011) throughout.

## 2. DATA

**Table 1.** CDF-S SCUBA-2 Observations

Weather	Scan	Exposure
Band	Pattern	(Hr)
1	CV DAISY	8.5
2	CV DAISY	45.0
3	CV DAISY	5.5
1	PONG-900	6.0
2	PONG-900	32.1
3	PONG-900	12.0

### 2.1. SCUBA-2 Observations

We made observations from late 2011 through early 2017 using SCUBA-2, which obtains simultaneous data at  $450 \mu\text{m}$  and  $850 \mu\text{m}$ . The mean aimpoint of our SCUBA-2 observations is R.A. 03:32:26.49, Decl.  $-27:48:29.0$  (J2000.0). In the central region, we used the CV DAISY scan pattern—whose field size ( $5.5'$  radius; by this radius the noise is twice the central noise) is well matched to the deepest portion of the X-ray image—to obtain the maximum depth. To cover the outer regions, we used the larger field PONG-900 scan pattern ( $10.5'$  radius; by this radius the noise is twice the central noise), which finds brighter but rarer sources. Detailed information on the SCUBA-2 scan patterns can be found in Holland et al. (2013).

We summarize our SCUBA-2 GOODS-S observations in Table 1, where we give the weather conditions (band 1,  $\tau_{225 \text{ GHz}} < 0.05$ ; band 2,  $0.05 < \tau_{225 \text{ GHz}} < 0.08$ ; band 3,  $0.08 < \tau_{225 \text{ GHz}} < 0.12$ ), scan patterns used, and exposure times. Including the poorer weather band 3 observations, we have 109 hr of exposure time in the final  $850 \mu\text{m}$  reductions, roughly equally divided between the two scan patterns. We did not use the small amount of band 3 data in the  $450 \mu\text{m}$  reductions, and with predominantly band 2 (rather than band 1) weather, the  $450 \mu\text{m}$  observations are not very deep (central rms of  $3.6 \text{ mJy}$  at  $450 \mu\text{m}$  versus  $0.30 \text{ mJy}$  at  $850 \mu\text{m}$ ). Thus, we primarily focus here on the  $850 \mu\text{m}$  results.

Our reduction procedures follow Chen et al. (2013) and are described in detail in Paper I. The galaxies are expected to appear as unresolved sources at the  $\sim 14''$  resolution of the JCMT at  $850 \mu\text{m}$ . We therefore applied a matched-filter to our maps, which provides a maximum likelihood estimate of the source strength for unresolved sources (e.g., Serjeant et al. 2003).

In Figure 1, we show the  $850 \mu\text{m}$  matched-filter S/N image of the CDF-S made from all of the observations, including the band 3 data. In Figure 2, we show the rms

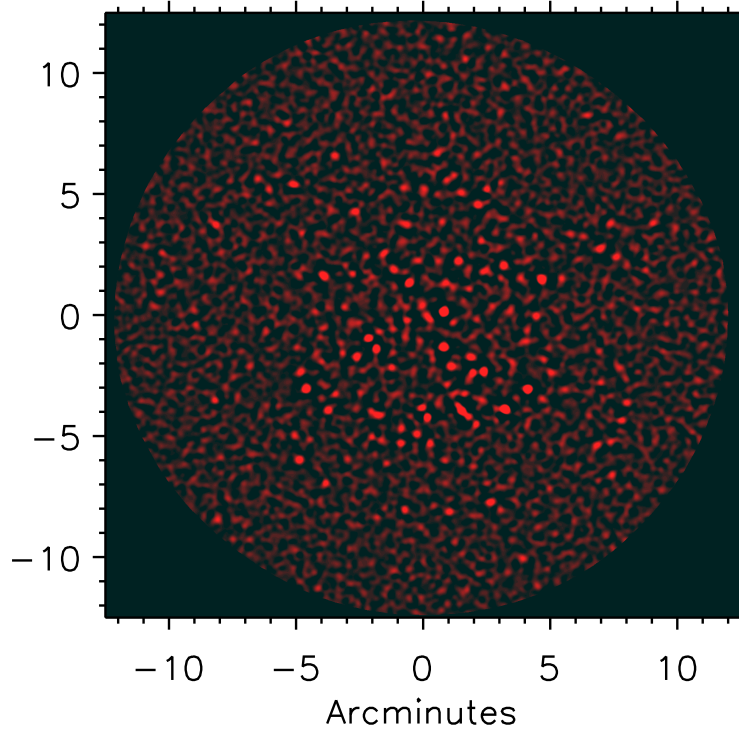


**Figure 1.**  $850\ \mu\text{m}$  matched filter S/N image of the CDF-S region. The more sensitive central region (radius less than  $\sim 6'$ ) is dominated by the CV DAISY observations, while the outer region is covered by the PONG-900 observations.

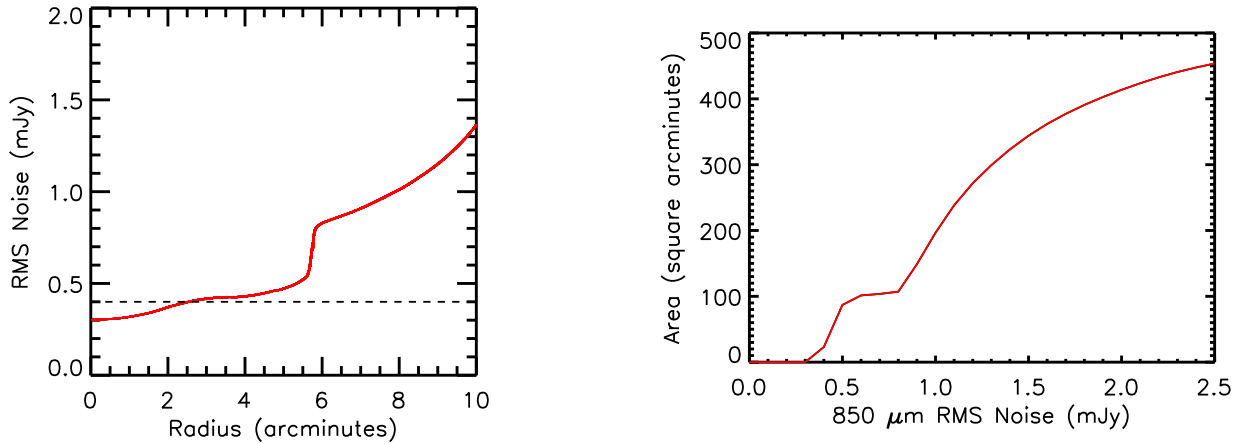


**Figure 2.** (Left) Azimuthally averaged  $850\ \mu\text{m}$  rms noise vs. radius. The more sensitive central region (radius less than  $\sim 6'$ ) is dominated by the CV DAISY observations, while the outer region is covered by the PONG-900 observations. The black dashed horizontal line shows the rms noise corresponding to a  $4\sigma$  detection threshold of  $1.6\ \text{mJy}$ , which is approximately the confusion limit for the JCMT at  $850\ \mu\text{m}$  of  $\sim 1.65\ \text{mJy}$ . (Right) Cumulative area covered vs.  $850\ \mu\text{m}$  rms noise.

noise versus radius (*left*), as well as the cumulative area observed below a given rms noise (*right*).

## 2.2. SCUBA-2 Source Catalog Construction

As in Paper I, we generated the source catalogs by identifying the peak S/N pixel, subtracting this peak pixel and its surrounding areas using the PSF scaled and centered on the value and position of that pixel, and

then searching for the next S/N peak. We iterated this process until we reached a S/N of 3.5. We then limited the sample to the sources with a S/N above 4, giving a sample of 146 sources at  $850\ \mu\text{m}$ , 123 with fluxes above  $2\ \text{mJy}$ .

We present and analyze this *full SCUBA-2 sample* in A. Barger et al. (2018, in preparation; Paper IV). Although we also occasionally make use of the full sample

in this paper (mainly when making comparisons with other samples), our primary goal here is to construct and analyze a complete SCUBA-2 sample.

We start with the 90 SCUBA-2 sources with fluxes  $> 1.65$  mJy that lie within the central region of the image where the SCUBA-2 noise is less than 0.56 mJy (a 100 arcmin<sup>2</sup> area, or roughly a radius of 5'.7, though the area is not perfectly circular); we refer to this as our *full central SCUBA-2 sample*. Given the noise of 0.56 mJy at the outer edges of this region (see Figure 2), the flux limit for our *complete central SCUBA-2 sample* is then 2.25 mJy ( $> 4\sigma$ ).

In Table 2, we list the 53 SCUBA-2 sources in this complete sample, along with their SCUBA-2 fluxes, their measured ALMA source positions (see Section 2.4), the offsets between the SCUBA-2 and ALMA source positions, and their measured ALMA fluxes. However, for 5 of the 53 sources, the ALMA observations yielded no ALMA detections; thus, for those 5 cases, we list the central  $1\sigma$  noise in the ALMA image (enclosed in square brackets) instead of an ALMA flux detection. For three of these sources, the central noise in the ALMA image is low enough ( $\sim 0.1$  mJy) that we should easily detect the SCUBA-2 source at the  $4.5\sigma$  level in the ALMA image, even if it were a double source where the two components lay near the half power radius of the ALMA image. The remaining two sources have noisier ALMA images, and the SCUBA-2 source might be missed if it had multiple components or were positioned in less sensitive portions of the ALMA beam.

### 2.3. Comparison with Previous Single-Dish Observations

The CDF-S was previously observed at 850  $\mu$ m with LABOCA on the APEX telescope (Weiß et al. 2009) and at 1.1 mm with AzTEC on the 10 m Atacama Submillimeter Telescope Experiment (ASTE; Scott et al. 2010). In Figure 3, we compare these samples with our complete central SCUBA-2 sample (blue solid circles), and with other secure ( $> 4\sigma$ ) SCUBA-2 sources from our full sample (blue open squares; these sources are either fainter than 2.25 mJy, or they lie outside the 5'.7 central region shown in green).

The LABOCA and AzTEC images are considerably shallower and lower resolution than the SCUBA-2 image, and all of their sources within the 5'.7 radius region have counterparts in our full central SCUBA-2 sample. The LABOCA (19".2 FWHM PSF) observations cover the much wider Extended CDF-S (ECDF-S) region, but their limiting  $4\sigma$  flux is around 5–6 mJy, and they find only eight sources within the central region. The AzTEC (30".0 FWHM PSF) observations are deeper and contain 20 sources in the central region, but because of the lower resolution and associated blending, the AzTEC source positions have substantial offsets relative to the SCUBA-2 source positions.

Using our full SCUBA-2 sample to give a substantial overlap, in Figure 4, we compare the LABOCA fluxes with the SCUBA-2 fluxes. Each SCUBA-2 source was matched to the nearest LABOCA source within a 6" radius, whenever such a source is present. Note that the plotted fluxes are direct LABOCA and SCUBA-2 flux measurements without any accounting for blending. Blending is only an issue for three sources in the LABOCA sample, but it is much more severe for the lower resolution AzTEC data, where 10 of the AzTEC sources correspond to multiple SCUBA-2 sources. Sources detected with AzTEC are shown in red and include most of the brighter SCUBA-2 and LABOCA sources.

Where LABOCA detects the SCUBA-2 source, the mean ratio of the LABOCA fluxes to the SCUBA-2 fluxes is  $0.96 \pm 0.04$ , which is well within the  $\sim 10\%$  calibration uncertainty on the SCUBA-2 data (Paper I) and the  $\sim 15\%$  calibration uncertainty on the LABOCA data (Hodge et al. 2013). However, both LABOCA and AzTEC miss bright submillimeter sources that they should have been able to detect (see Figure 4). For example, LABOCA, with its rms of 1.2 mJy, should have detected sources above 6 mJy at the  $5\sigma$  level, but of the 16 SCUBA-2 sources with detected fluxes above 6 mJy to rms noise less than 1 mJy, only 11 are included in the LABOCA sample. This substantial incompleteness will carry through to the follow-up observations with ALMA (ALESS).

### 2.4. ALMA Observations

As part of our ALMA program “BASIC: A Bright ALMA Survey of SMGs In the *Chandra* Deep Field-South” (ADS/JAO.ALMA #2015.1.00242.S; PI: F. Bauer), we observed 61 fields in the CDF-S between July 13 and November 25, 2016 with the C40-4 array configuration in band 7 (hereafter, the cycle3 program). We also observed a substantially overlapped sample of 60 fields (21 new and 39 repeats) in July and August, 2017 (ADS/JAO.ALMA #2016.1.01079.S; PI: F. Bauer) in the C40-3 array configuration in band 7 (hereafter, the cycle4 program). We refer to the combination of the cycle3 and cycle4 observations as “BASIC”. We analyzed an additional 12 fields observed as part of other ALMA band 7 projects (hereafter, “archival”). We processed all the ALMA data in a consistent manner.

We centered the BASIC observations on the targeted source positions and used a spectral setup configured with four 1.875 GHz spectral windows (using time division mode) placed around a central frequency of 343.5 GHz in order to sample crudely the same 850  $\mu$ m continuum as SCUBA-2. This returned a representative spectral resolution of  $\sim 28$  km s<sup>-1</sup>.

The cycle3 program consisted of three complete and one partially complete executions (hereafter, executions 1 through 4), with combined integration times between 2.4 min and 3.2 min for each source. We cal-

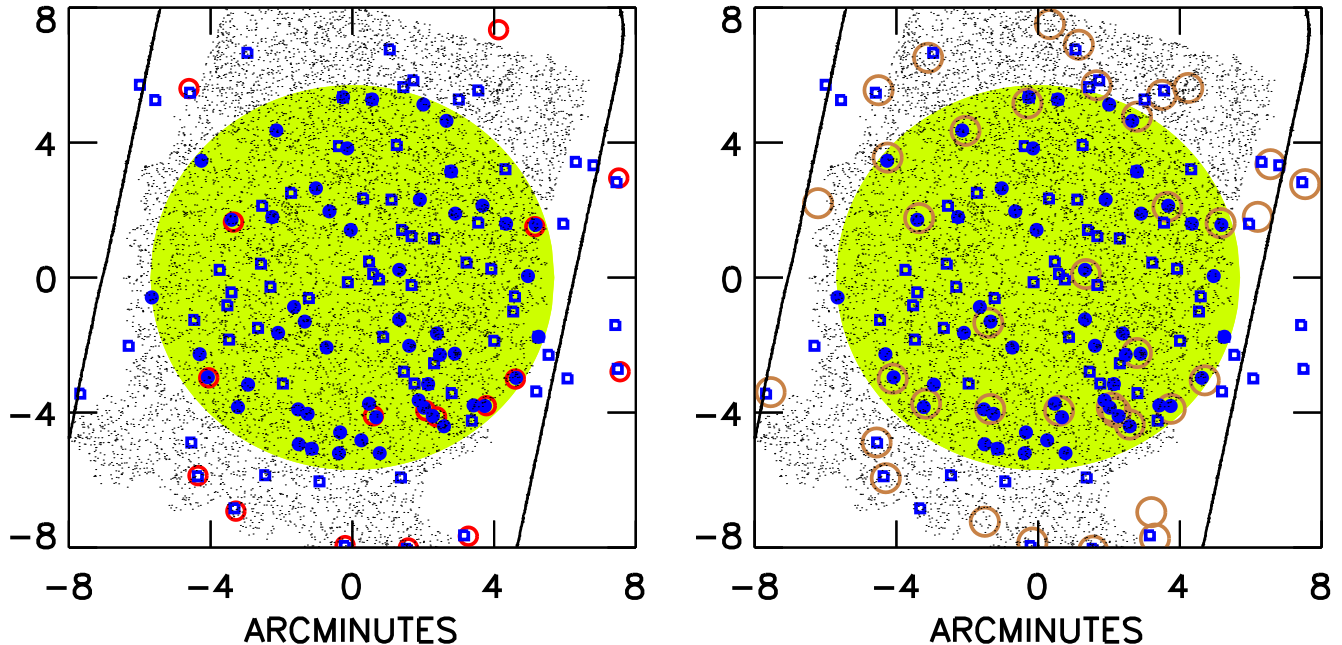


**Figure 3.** Comparison of our complete central SCUBA-2 sample (blue solid circles) with (*left*) the LABOCA 850  $\mu\text{m}$  sample of Weiß et al. (2009; red circles whose size illustrates the  $19''.2$  FWHM PSF) and with (*right*) the AzTEC 1.1 mm sample of Scott et al. (2010; golden circles whose size illustrates the  $30''.0$  FWHM PSF). In both panels, the green shading shows the central  $5''.7$  radius region that corresponds to the deepest SCUBA-2 data. Blue open squares show other secure ( $> 4\sigma$ ) SCUBA-2 sources from our full sample (these sources are either fainter than 2.25 mJy, or they lie outside the central region). The black speckled shading shows the *HST* ACS GOODS-S region (Giavalisco et al. 2004), and the black solid rectangle shows the GOODS-*Herschel* region (Elbaz et al. 2011).

ibrated the data and made images using CASA version 4.7.0 and the included pipeline. We used source J0522-3627 as the bandpass calibrator, Ceres and J0334-4008 as the flux calibrators, and J0329-2357 and J0348-2749 as the phase and gain calibrators. We performed manual flagging in addition to the pipeline processing to remove outlier baselines and/or antennas. We estimate the final error in the absolute flux calibration to be  $\sim 5\%$ .

After data calibration, we discovered that executions 1 and 2 had worse phase calibration than executions 3 and 4, especially for the targets observed at the beginning of the executions. Execution 1 showed a problem with the phase calibration that could not be corrected by the available water vapor radiometer data, resulting in an observed wandering offset in the positions of the first several sources when compared to the other three executions. Execution 2 also showed indications of a phase calibration problem, but this problem was considerably less severe than for execution 1. Because of this behavior, for the first six targets observed, we only used the data corresponding to executions 2 – 4, while for the rest of the targets, we included all of the available data.

The cycle4 program consisted of four complete executions, with a combined integration time of 2.7 min for each source. We calibrated the data and made images

using CASA version 4.7.2 and the corresponding included pipeline. We used sources J0522-3627 and J0006-0623 as the bandpass calibrators, J0334-4008 as the flux calibrator, and J0348-2749 as the phase and gain calibrator. The cycle4 observations did not show any of the problems seen in the cycle3 observations.

A nominal natural-weighted beam of  $0''.38 \times 0''.3$  was achieved for the cycle3 observations, while the cycle4 observations were taken with a slightly more extended antenna configuration, achieving a natural-weighted beam of  $0''.15 \times 0''.1$ . We combined the visibilities for the fields that were observed in both cycles using the CASA task concatenate, thereby obtaining a combined beam similar to the one from cycle3 ( $0''.38 \times 0''.31$ ). We made images of the targets using the task CLEAN. We made dirty images using natural weighting and a mild  $uv$ -taper to achieve a representative synthesized beam of  $0''.53 \times 0''.48$  and a position angle of  $-87^\circ.16$ . Based on the size estimates from Simpson et al. (2015), we adopted a beam size of  $\approx 0''.5$ , which offers the best trade-off between retaining a relatively low rms and increasing the sensitivity to extended sources in our data; tapering the data to larger beams means weighting toward shorter baselines and hence fewer antennas and lower sensitivity.

We included a further 14 sources from 12 band 7 archival images (there were 11 single sources and one

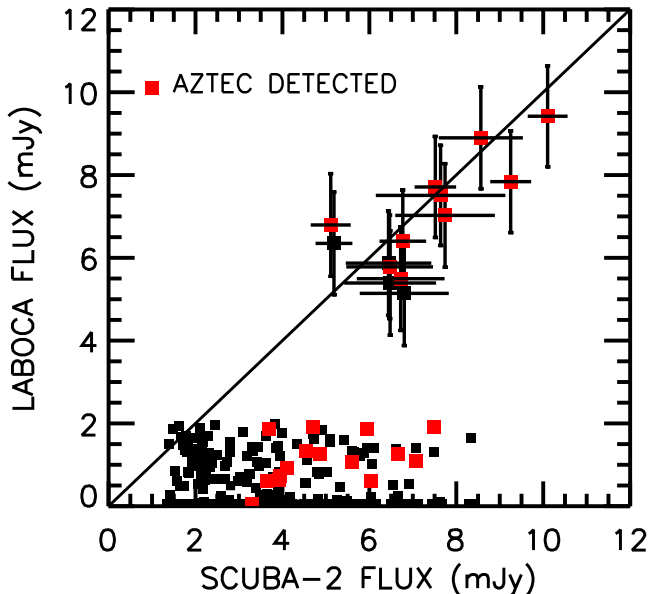


**Figure 4.** Comparison of the directly measured SCUBA-2 and LABOCA fluxes for our full SCUBA-2 sample. We compare to the nearest LABOCA match (whenever present) within a  $6''$  radius around each SCUBA-2 source, and we do not account for any blending. SCUBA-2 sources without LABOCA detections are shown randomly scattered at fluxes between 0 and 2 mJy at the bottom of the plot for clarity. Sources that are also detected in the longer wavelength AzTEC observations are shown in red. The mean ratio of the LABOCA fluxes to the SCUBA-2 fluxes is  $0.96 \pm 0.04$ .

triple source in these images). Since 11 of these images have extremely similar observational setups to BASIC, we used the same reduction procedures. We acquired four archival sources from the ALESS sample (Hodge et al. 2013; ADS/JAO.ALMA #2011.1.00294.S, ADS/JAO.ALMA #2012.1.00307.S), eight more from the X-ray AGN sample of Mullaney et al. (2015; ADS/JAO.ALMA #2012.1.00869.S), and one from the red nugget sample of P.I. G. Barro (ADS/JAO.ALMA #2013.1.00205.S). The 14th source was observed in an extended configuration as part of the ALMA Redshift 4 Survey (AR4S) of Schreiber et al. (2017; ADS/JAO.ALMA #2012.1.00983.S). We reduced it to match the current work as best as possible.

We calibrated the original “raw” datasets using CASA version 4.7.2 and either the pipeline for newer datasets or the reduction script provided for older datasets (updated for the correct CASA version). As above, we performed extra manual flagging, as necessary. In cases where the natural beam of the archival data was smaller than  $\approx 0''.5$ , we adopted a  $uv$ -taper to achieve a similar beam size. Otherwise, we used the natural-weighted images.

We performed an initial source search on the dirty images of both the BASIC and archival datasets prior

to primary beam correction, with the dual purpose of assessing the rms sensitivity and finding all secure detections. We produced cleaned images by placing  $2'' \times 2''$  clean boxes around all secure sources detected with  $S/N \geq 5$  in the dirty images. We stopped the final cleaning process after 1000 iterations, such that most of the emission associated with the sources was recovered.

The flux densities that we measured in the final images of the cycle3 program are in good agreement with the ones we obtained for the individual executions, suggesting that the phase calibration issue present in executions 1 and 2 does not affect our final flux density measurements.

### 2.5. ALMA Source Catalog Construction

We searched each of the  $0''.5$  cleaned images for significant sources. We restricted our search to the area contained within an  $8''.75$  radius, which corresponds to the ALMA half power. This also is well matched to the SCUBA-2 FWHM and should contain all sources contributing to the corresponding SCUBA-2 flux. The total searched area is  $6.3 \text{ arcmin}^2$  for the 82 unique BASIC images and 12 archival images.

We selected all sources with a peak flux  $S/N$  above 4.5 (see below). We determined the peak flux noise using the dispersion in 100 independent beam positions surrounding the source. We measured a median rms noise for the sources in the cycle3 program of 0.15 mJy with a minimum of 0.11 mJy and a maximum of 0.23 mJy. Sources that were only observed in the cycle4 program have a higher median rms noise of 0.29 mJy, with a range from 0.19 to 0.32 mJy. Sources with observations in both cycle3 and cycle4 may have a noise as low as 0.095 mJy.

The total searched area corresponds to 50,000 independent beams. For a Gaussian distribution in the noise, we expect 1.5 false sources above a  $S/N$  cut of 4, and 0.26 false sources above a  $S/N$  cut of 4.5. Since the Gaussian assumption may be questionable, we also made an empirical test by applying our detection method to the negative of each image. This gives two sources at  $S/N = 4 - 4.5$  and none above 4.5, consistent with the Gaussian expectation. We therefore restricted our final sample to the sources with  $S/N > 4.5$ , which we expect to be highly robust.

We found that the peak fluxes, even in the  $0''.5$  tapered images, slightly underestimate the total fluxes. The reason for this is that the sources are resolved. In order to estimate the total fluxes, we used two methods. In the first method, we took the ratio of aperture flux measurements made in a range of aperture radii to the peak flux measurements. As we show in Figure 5, the median multiplicative correction asymptotes beyond a radius of  $\approx 0''.6$ , and we used this as our preferred radius. For the sources where the ratio of the aperture flux to the peak flux exceeds 1.4, we used the aperture flux. For the remaining sources, we used the peak flux times the

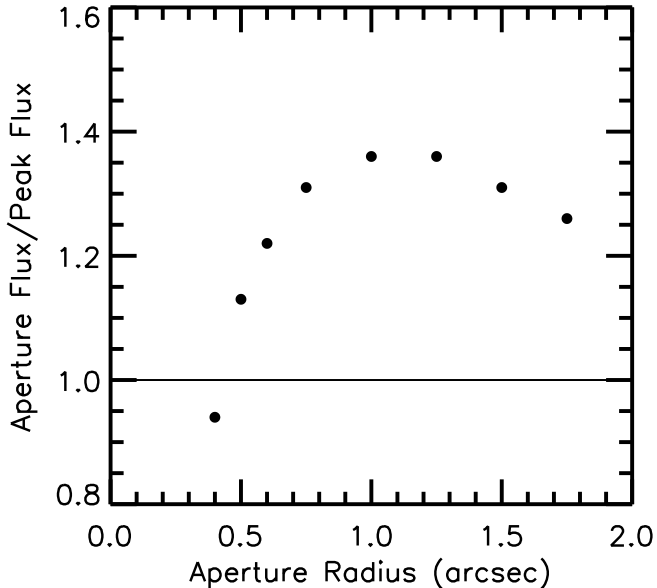


**Figure 5.** Median ratio of the aperture flux to the peak flux vs. the aperture radius for the 75 ALMA sources.

median correction of 1.22. We refer to these as our *best flux estimates*.

In the second method, we fitted the sources in the  $uv$  plane by adopting a Gaussian shape. J. González-López et al. (2018, in preparation) give more details on these fits, which are used to estimate the source shapes and sizes. As we show in Figure 6, the fluxes that we estimate from the  $uv$  fits agree extremely well with the more straightforward best flux estimates.

In Table 3, we give brief descriptions and numbers for the various samples that we use in this paper. The ALMA images cover all 53  $> 2.25$  mJy sources in the complete central SCUBA-2 sample (Table 2), together with a number of fainter SCUBA-2 sources. We note that the ALMA band 7 primary beam of  $\sim 17''$  is larger than the SCUBA-2 beam of  $\sim 14''$ , allowing ALMA to image all sources that contribute to the SCUBA-2 flux.

In total, we have 75  $> 4.5\sigma$  ALMA sources, which corresponds to a lower limit of 0.75 sources per arcmin<sup>2</sup> (since we have not uniformly sampled the area with ALMA). We summarize this sample, which we hereafter refer to as our *total ALMA sample*, in Table 4, where we provide the peak and best ALMA fluxes and errors, the S/N, the F18 1.13 mm ALMA flux when available (see Section 2.6), the SCUBA-2 source number from Table 2 whenever there is such a source located within a radius of  $5''$  of the ALMA position, and the offset between the SCUBA-2 and ALMA source positions for these sources. Only one of the detected sources in Table 4 has a S/N between 4.5 and 5, while the remainder all have S/N above 5.

The effects of blending and Eddington bias will only reduce the measured ALMA fluxes relative to the

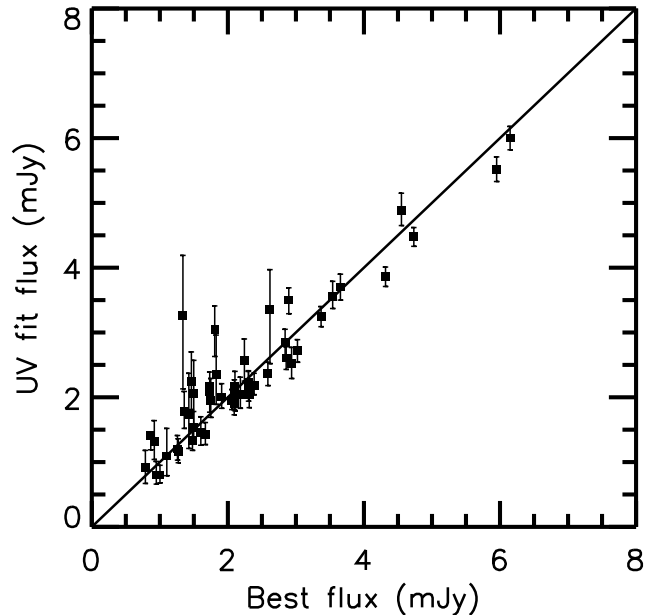


**Figure 6.** Comparison of the flux measured using fits to a Gaussian spatial profile in the  $uv$  plane vs. the simpler best flux estimate based on the peak and aperture fluxes, as described in the text.

SCUBA-2 fluxes. Thus, we hereafter refer to the ALMA sample of 41 sources above 2.25 mJy as our *complete ALMA sample*. The cumulative ALMA number density above 2.25 mJy is just over 1500 sources per deg<sup>2</sup>, compared with an expected value of just under 2200 based on incompleteness and Eddington bias corrected SCUBA-2 850  $\mu$ m number counts for a number of fields (e.g., Hsu et al. 2016). In a subsequent paper, we will provide incompleteness corrected ALMA counts to fainter fluxes and compare with the corrected SCUBA-2 counts in more detail.

## 2.6. Comparison with 1.13 mm ALMA sample

F18 obtained a sample of 1.13 mm galaxies based on a homogeneous scan of a 69 arcmin<sup>2</sup> region of the GOODS-S. This region is largely contained within our total ALMA area, with all 20 sources in their main catalog lying in our area, and only one of their three supplemental sources lying outside our area.

In terms of detections, 17 of their 20 main catalog sources are in our total ALMA sample. The remaining three are not detected in our SCUBA-2 image, and, indeed, correspond to sources that F18 consider likely to be false (these are their sources AGS14, AGS16, and AGS19). Their two supplemental sources that lie in our area are also detected in our total ALMA sample.

In Table 4, we give the F18 fluxes based on their GALFIT values and without applying any deboosting. However, in the region where there are also longer wavelength ALMA observations from Dunlop et al. (2017),



**Table 3.** CDF-S Central Region Details

Description	Covered Area (arcmin <sup>2</sup> )	Number		
		Total	Targeted by ALMA	At least 1 ALMA > 4.5 $\sigma$ Detection
SCUBA-2 > 4 $\sigma$ sources with flux > 1.65 mJy	100	90	79	60
... with SCUBA-2 flux > 2.25 mJy (see Table 2)		53	53	48
... with SCUBA-2 flux > 4 mJy		16	16	16
... with SCUBA-2 flux 2.25 – 4 mJy		37	37	32
... with SCUBA-2 flux 1.65 – 2.25 mJy		37	26	10
... add't just outside central region		3	3	3
Add't targets in central region but too faint for SCUBA-2 sample		3	3	3
Total ALMA > 4.5 $\sigma$ detections (see Table 4)	6.3	75		
... with flux > 2.25 mJy (see Table 4)		41		
... from targeting SCUBA-2 > 4 $\sigma$ sources with flux > 1.65 mJy	5.3	69		

NOTE—The 69 ALMA > 4.5 $\sigma$  sources from targeting 79 SCUBA-2 > 4 $\sigma$  sources with flux > 1.65 mJy include one triple, 7 doubles, 52 singles, and 19 fields with no detections.

we find that the F18 fluxes lie below the interpolation between our 850  $\mu$ m values and the Dunlop et al. 1.3 mm values, suggesting that the 1.13 mm data of F18 need to be corrected for extended flux. In our analysis (but not in Table 4), we apply a multiplicative correction of 1.35 to allow for this.

### 3. ALMA VERSUS SCUBA-2

In Figure 7, we show a simple flux comparison between the ALMA sources and the SCUBA-2 sources by plotting the nearest peak SCUBA-2 flux against the ALMA flux. Where more than one ALMA source corresponds to a SCUBA-2 source, we have added the ALMA fluxes together and surrounded the symbol with an open box. All the ALMA fluxes are consistent with the SCUBA-2 fluxes within our 10% estimated error in the SCUBA-2 fluxes and the similar estimated error in the ALMA fluxes.

We make a more precise comparison that properly allows for blending by constructing a simulated SCUBA-2 image that would be produced by the observed ALMA sources. Each ALMA source is convolved with the SCUBA-2 matched-filter PSF and added to form a final image. We show the simulated SCUBA-2 image in the bottom left panel of Figure 8 compared with the true SCUBA-2 image in the bottom right panel.

We subtracted the ALMA-constructed SCUBA-2 image from the real SCUBA-2 image to form a residual image, which we show in the upper left panel of Figure 8. We show the ALMA pointings in the upper right panel. We searched the differenced image the same way that we did when we generated the catalog of SCUBA-2

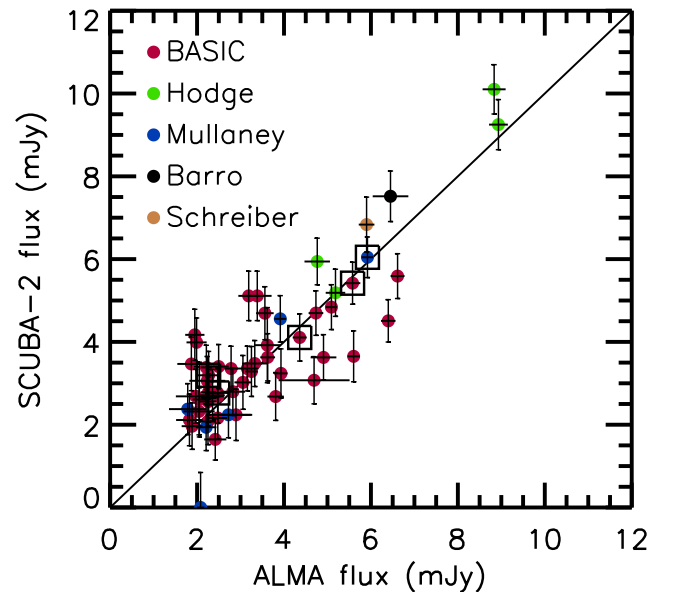


**Figure 7.** Comparison of the ALMA fluxes with the SCUBA-2 fluxes measured at the ALMA positions. Where there are multiple ALMA sources, we have added the individual ALMA fluxes and marked them with a large open square. The BASIC sources are shown in red, while the archival sources are color coded according to the legend.

sources from the observed SCUBA-2 image. This procedure detects seven sources with SCUBA-2 fluxes above 2.25 mJy in the differenced image. The only source in the differenced image with a flux substantially larger than 2.5 mJy has a flux of 3.4 mJy. This source is a close

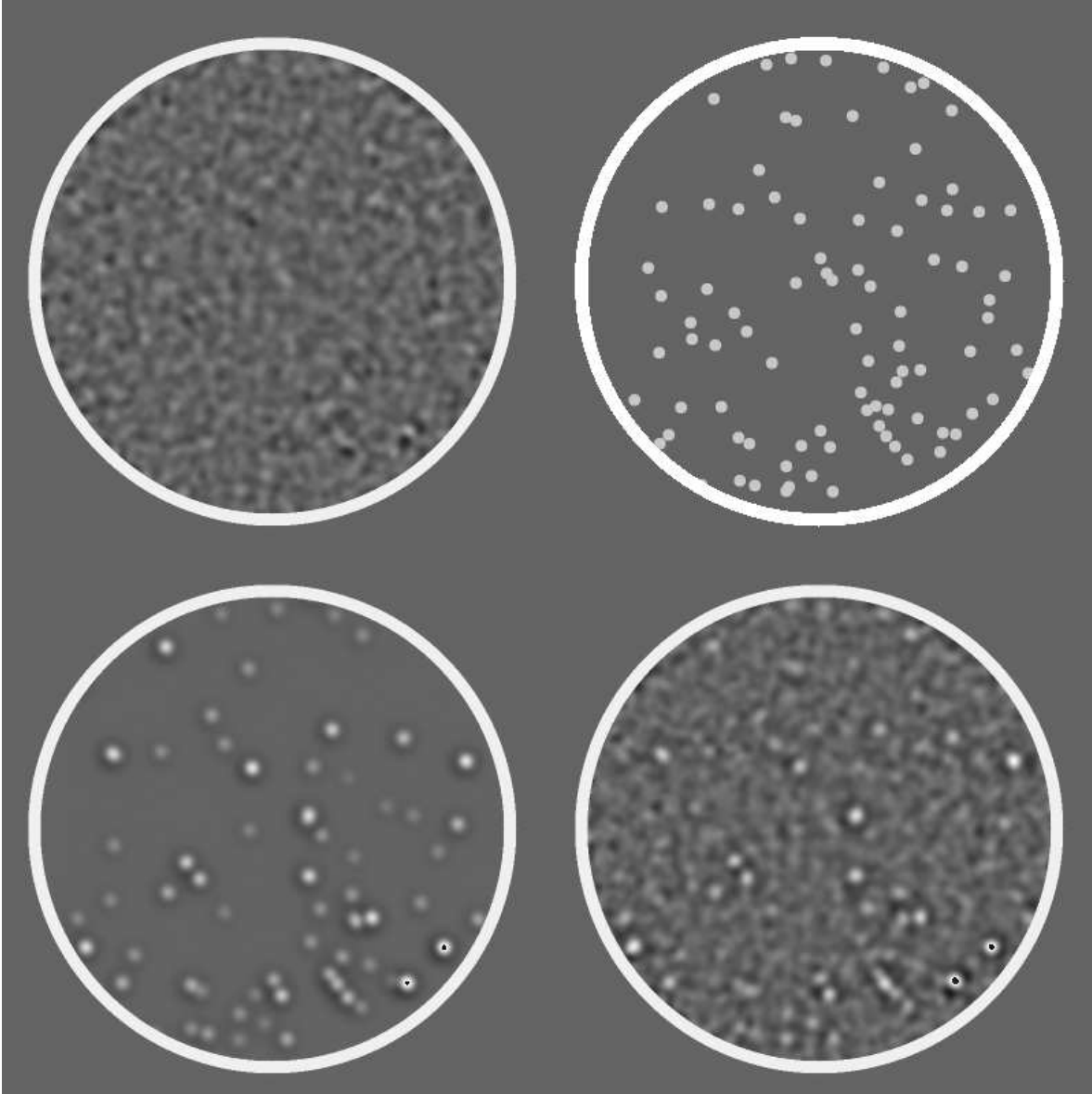


**Figure 8.** *Top left:* ALMA-constructed SCUBA-2 image subtracted from the actual SCUBA-2 image. *Top right:* ALMA pointings in the field. *Bottom left:* ALMA-constructed SCUBA-2 image. *Bottom right:* Actual SCUBA-2 image.

neighbor of the brightest source in the field and may be a residual from imprecise subtraction of the bright source. This is covered by an archival ALMA pointing, and while there may be a weak (0.7 mJy) source near this position, there is nothing (i.e., individual or a small grouping of sources) that would produce this much flux.

The remaining six sources have fluxes between 2.25 and just over 2.5 mJy. All of these correspond to sources in Table 2, and all were observed as part of BASIC. For source 15 in Table 2, the ALMA detection is faint compared to the SCUBA-2 flux, and for the remaining sources (44, 46, 49, 50, and 53), no ALMA sources were detected. This suggests that there may be several

ALMA counterparts to these SCUBA-2 sources, which we have not been able to detect.

Based on the mean offset of 39 isolated ALMA sources with fluxes greater than 2.25 mJy from the nearest SCUBA-2 peak, we find an absolute astrometric offset of  $0''.9$  in R.A. and  $-0''.3$  in Decl., which we applied to the SCUBA-2 positions. This is well within the expected uncertainty in the absolute SCUBA-2 astrometry.

In Figure 9, we show the offsets between the ALMA and SCUBA-2 positions for the complete central SCUBA-2 sample (Table 2), excluding only the 5 sources with no ALMA detections. Where there is a single ALMA counterpart, we show the offset with a

red square, and where there is more than one ALMA counterpart, we show the offsets with connected blue diamonds. The mean offset of the individual sources (i.e., the scatter) is  $2''.2$  for all SCUBA-2 sources with fluxes above  $2.25$  mJy and a single ALMA counterpart.

The overall percentage of SCUBA-2 sources above  $2.25$  mJy with multiple ALMA counterparts is 13% (68% confidence range 7–19%). Here each of the counterparts has to be above the ALMA  $4.5\sigma$  detection threshold. The median  $4.5\sigma$  detection limit is  $1.04$  mJy, and 52 of the 75 sources have limits less than  $1.25$  mJy. Thus, at the  $2.25$  mJy limit, we could detect two roughly equal sources, while at  $3$  mJy, we could detect a multiple with two sources with a 2:1 flux ratio. If the two sources in Table 2 with SCUBA-2 fluxes above  $2.25$  mJy, no ALMA counterpart, and a high noise ALMA image were also multiples, then this would rise to 16%.

This is a considerably smaller multiplicity than the  $\sim 30\%$  found in the ALESS followup of the LABOCA sample (Hodge et al. 2013; Simpson et al. 2015). In substantial part, this is due to the smaller SCUBA-2 beam, which has 64% of the area of the LABOCA beam (LABOCA was on the 12 m APEX telescope). The smaller beam will pick up a smaller fraction of multiples. There could also be a dependence on flux, and the lower multiplicity could be partly a consequence of the depth of the SCUBA-2 sample. If we restricted to sources with SCUBA-2 fluxes greater than  $4$  mJy, then the fraction would be 27%, with a range of 16 to 42%. This is highly uncertain, because of the small sample size, and, indeed, there could be no variation in the multiplicity as a function of flux. Note that Hill et al. (2018) found that  $\lesssim 15\%$  of 105 sources from the SCUBA-2 Cosmology Legacy Survey observed with the SMA at fluxes  $\gtrsim 10$  mJy were multiples (defined as bright SMGs that resolve into two or more galaxies with flux ratios close to 1).

#### 4. ANCILLARY INFORMATION

In this section, we consider the 75 ALMA sources in Table 4 (i.e., our total ALMA sample). While we acknowledge that this is not a complete sample below  $2.25$  mJy, completeness is not needed when trying to understand the properties of these securely detected ( $> 4.5\sigma$ ) ALMA sources. Indeed, the precise positions allow us to exploit the wealth of additional information available in the CDF-S/GOODS-S region, which is one of the most intensively studied regions on the sky. In particular, we can find the optical, near-infrared (NIR), and mid-infrared (MIR) counterparts to the SMGs, determine whether there are previous spectroscopic identifications, and calculate photometric redshifts for the sources.

##### 4.1. Optical and F160W Counterparts

All but one source in our total ALMA sample lie within the deep GOODS *HST* ACS optical imaging of

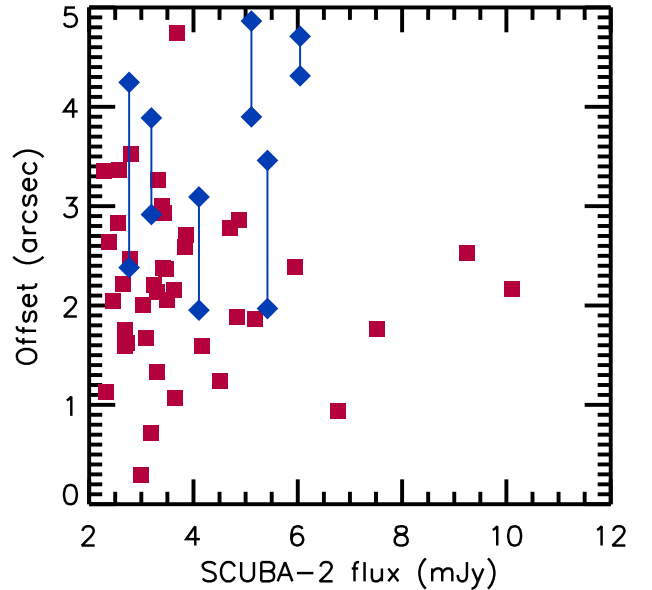


**Figure 9.** Offsets between the ALMA and SCUBA-2 positions vs. SCUBA-2 flux for the complete central SCUBA-2 sample, excluding only the 5 sources with no ALMA detections. Red squares show the SCUBA-2 sources with unique ALMA counterparts. Blue diamonds show the SCUBA-2 sources with multiple ALMA counterparts; here the offsets are joined by blue lines. The median offset is  $2''.2$  for the SCUBA-2 sources with unique ALMA counterparts. The fraction of sources with multiple counterparts is 13%, with a 68% confidence range of 7 to 19%.

Giavalisco et al. (2004) and the deep CANDELS *HST* WFC3 ultraviolet/optical channel and WFC3 infrared channel (WFC3/IR) imaging of Grogin et al. (2011) and Koekemoer et al. (2011).

In Figure 10, we show color thumbnail images made from the version 1.5 data release of the Hubble Legacy Fields by Illingworth et al. (2016), which combines 2442 orbits of the GOODS-S/CDF-S region ACS and WFC3/IR images. We overlay the ALMA data as white contours. The one ALMA source that lies outside the GOODS-S and CANDELS regions (source 27 or ALMA033203-275039 in Table 4) is omitted from the figure.

Comparing the ALMA positions with the CANDELS coordinates measured from the Hubble Legacy Fields F160W image gives an absolute astrometric offset of  $0''.06$  in R.A. and an offset of  $-0''.24$  in Decl. These are very similar to the offsets found by Chen et al. (2015) from their analysis of the ALESS sample in the ECDF-S ( $0''.11$  and  $-0''.25$ ). We apply these offsets throughout in comparing the various samples, including for the overlays in Figure 10.

After excluding source 27, 66 of the remaining 74 ALMA sources have counterparts within a  $1''$  matching

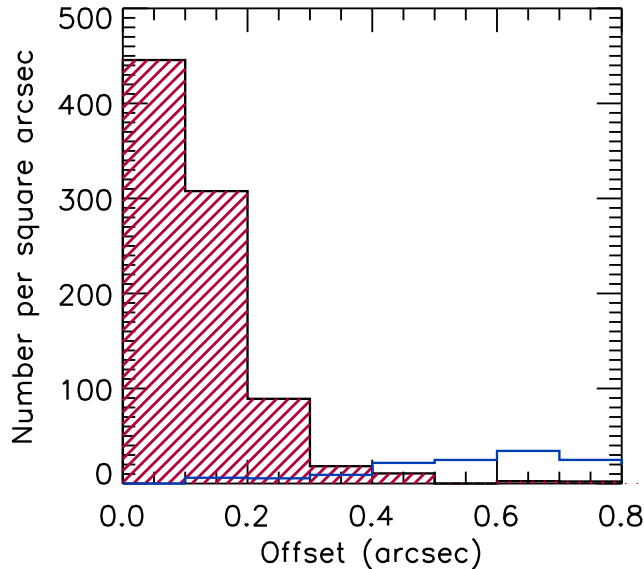


**Figure 11.** Distribution of offsets between the ALMA and G13 positions (red hatched histogram). The numbers are per unit area in  $0''.1$  stepped annuli. The blue histogram shows the expected distribution for a randomized sample with the same number of sources.

radius in the CANDELS catalog of G13, after applying the small astrometric correction. In Figure 11, we show the distribution of the offsets between the ALMA and G13 positions (red hatched histogram). (We include these offsets in Table 5.) We also show the expected distribution of a random sample of the same size (blue histogram). The mean of the offsets between the ALMA and G13 positions is  $0''.19$ , with 49 of the ALMA sources lying within  $0''.25$ . Beyond  $0''.4$ , there is a high probability that the source is a false match, and 5 of the 66 sources fall in this category.

The sources without counterparts (8 of them) or those that are probable false matches (5 of them) are sources 1, 2, 6, 13, 19, 29, 44, 51, 58, 61, 64, 68, and 75 in Table 4 (see Figure 10). For these sources, we measured the magnitudes directly at the ALMA positions using the imaging data, matching the zero points and the apertures to the G13 sample. However, for the 61 sources with counterparts closer than  $0''.4$ , we adopted the optical and NIR magnitudes from G13.

In some cases, the absence of a near counterpart in G13 to the ALMA source is due to the blending of a red galaxy with a bright near neighbor (e.g., source 6 or ALMA033246-275120 and source 29 or ALMA033232-274540; see Figure 10), which results in an overly large offset. Thus, as a second approach, we decided to measure directly from the image the offsets of the nearest F160W peaks from the ALMA positions. We only measured these offsets for sources that were clearly detected in the NIR, and we again excluded source 27 or

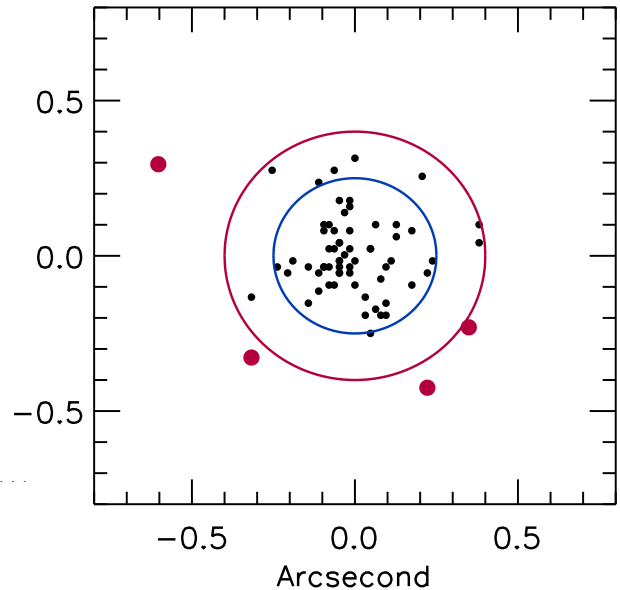


**Figure 12.** Offset in R.A. ( $x$  axis) and Decl. ( $y$  axis) between the ALMA position and the nearest NIR (F160W) peak. The blue large circle corresponds to  $0''.25$  and the red large circle to  $0''.4$ . Sources with separations larger than  $0''.4$  are shown with red circles. The positional uncertainties on both the ALMA sources and the F160W counterparts are much smaller than the measured offsets. The offsets may reflect whether the peak star formation is separated from the center of the NIR image (rest-frame optical at the redshifts of the sources), or, in some cases, whether the nearest NIR galaxy is actually the correct counterpart.

ALMA033203-275039. We found that 67 of the remaining 74 ALMA sources have counterparts within a  $1''$  matching radius. We show these offsets in Figure 12. In this case, we find 54 ALMA sources with a NIR peak within  $0''.25$  (blue circle in Figure 12), as compared to 49 when we matched to the G13 catalog. Note that the error in the determination of the ALMA centroids is extremely small by comparison, with the measured scatter typically around  $0''.015$  (see J. González-López et al. 2018, in preparation, for a more detailed discussion). Thus, the measured offsets relate primarily to a physical offset of the dust-emitting regions from the NIR peaks in the galaxies.

We also find that 4 of the 67 ALMA sources have a NIR peak separation larger than  $0''.4$  (red circles in Figure 12), as compared to 5 of the 66 when we matched to the G13 catalog. For these sources (1 or ALMA033207-275120<sup>1</sup>, 13 or ALMA033217-275233, 14 or ALMA033222-274936, and 32 or ALMA033211-

<sup>1</sup> This source is part of the ALESS survey. Hodge et al. (2013) assumed that the NIR peak was the correct counterpart and used its corresponding spectroscopic redshift from Danielson et

274615; see Figure 10), either the strongest star formation region is more strongly obscured and not coincident with the NIR peak (sources 14 and 32 might fall into this category), or we may be misidentifying a projected neighbor object as the counterpart. It is also possible that the ALMA source could be a background object lensed by a neighbor object, as, for example, might be the case for source 1.

In summary, the ALMA sources have extremely diverse optical/NIR counterparts that range from bright, low-redshift galaxies to sources invisible in the optical/NIR. These latter sources are the most plausible candidates for very high-redshift SMGs, and we shall return to them later in the paper.

#### 4.2. $K_s$ Counterparts

In order to compare uniformly the total ALMA sample to the main ALESS sample of Hodge et al. (2013) and the CDF-N sample of Paper I, we measured  $K_s$  magnitudes directly from the Canada-France-Hawaii Telescope  $K_s$  image of Hsieh et al. (2012). This  $K_s$  image covers the total ALMA sample (including source 27), as well as the ALESS main sample. We used 3'' diameter apertures, which provide a better approximation to the total magnitudes than smaller apertures. We chose the zeropoint to match the Very Large Telescope based  $K_s$  magnitudes given in the G13 CANDELS catalog.

In Figure 13, we compare the  $K_s$  magnitudes for the total ALMA sample (red circles) and the ALESS sample (green diamonds). We also compare with the GOODS-N SCUBA-2 850  $\mu\text{m}$  sample from Paper I down to the 5 mJy level (black squares), which has nearly complete, high-precision submillimeter positional identifications from SMA imaging. There is broad consistency among the samples, with all showing a wide range of  $K_s$  magnitudes from brighter than 20 to fainter than 25 at all submillimeter fluxes.

#### 4.3. Redshifts

We searched the literature for spectroscopic redshifts (hereafter, *speczs*) for the sources in the total ALMA sample. We summarize these in Table 5, noting the reference for each *specz* in the table notes. We excluded *speczs* where the measured galaxy was close to but appeared not to be the ALMA counterpart, or where we considered the spectral identification to be insecure. We rejected redshifts for sources 1, 6, and 29.

There have been numerous photometric redshifts (hereafter, *photzs*) compiled for the field (see Section 1). We take our *photzs* from S16, who used the EAZY code (Brammer et al. 2008) to fit the extensive and current ZFOURGE catalog from 0.3 to 8  $\mu\text{m}$ . Of the 75 sources in the total ALMA sample, 73 have counterparts within

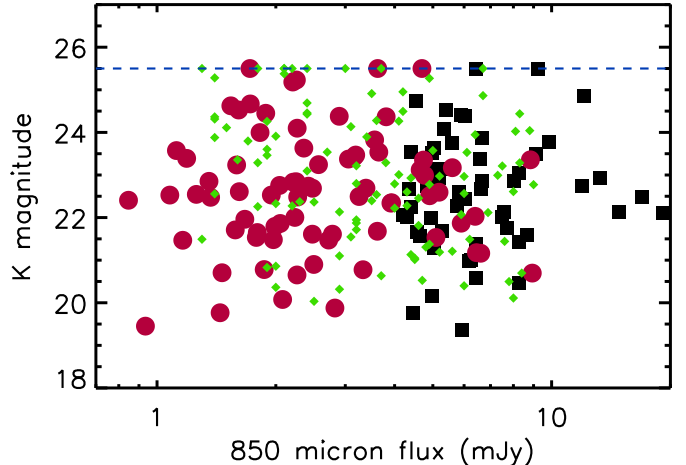


**Figure 13.**  $K_s$  magnitude vs. 850  $\mu\text{m}$  flux for the total ALMA sample (red circles), the ALESS sample (green diamonds), and the GOODS-N sample down to 5 mJy (black squares). Sources fainter than  $K_s = 25.5$  (blue dashed line) are shown at that value.

1''0 in the S16 catalog, after applying the astrometric corrections. However, a number of these are tagged with a very poor quality flag ( $Q$ ) from the EAZY code, reflecting the unusual SEDs of these high-redshift dusty galaxies and the limited number of band detections. If we restrict to the high-quality ( $Q < 3$ ) photzs, then this gives photzs for 59 of the ALMA sources, which we give in Table 5, together with the 95% confidence range.

In the top left panel of Figure 14, we plot redshift versus  $K_s$  magnitude for sources with *speczs* (black circles). For sources where there are no *speczs*, we plot *photzs* with  $Q < 3$  (red circles) and *photzs* with  $Q > 3$  (poor fits; blue circles) from S16. We hereafter use only the high-quality *photzs* from S16, unless specifically stated otherwise. The redshifts show a correlation with the  $K_s$  magnitudes, which has been demonstrated to be a crude redshift estimator (Barger et al. 2014; Simpson et al. 2014). This can also be seen when we use other photometric redshift estimates, such as those of Hsu et al. (2014) or Santini et al. (2015). However, there are large differences between the various *photz* estimates at the fainter magnitudes, as we illustrate in the top right panel of Figure 14 by plotting the difference between the various *photzs* as a function of  $K_s$  magnitude. Particularly at  $K_s > 23$  (blue shading), there are considerable uncertainties in the *photzs* and substantial variations between the groups' estimates. Despite this, the overall trend to higher redshifts with increasing  $K_s$  magnitude can still be seen in the bottom left panel, where we show simultaneously the three *photz* estimates for each source (black squares), connected with red lines. Finally, in the bottom right panel, we illustrate how even at bright

al. (2017). See Section 4.6 for another argument against this identification.

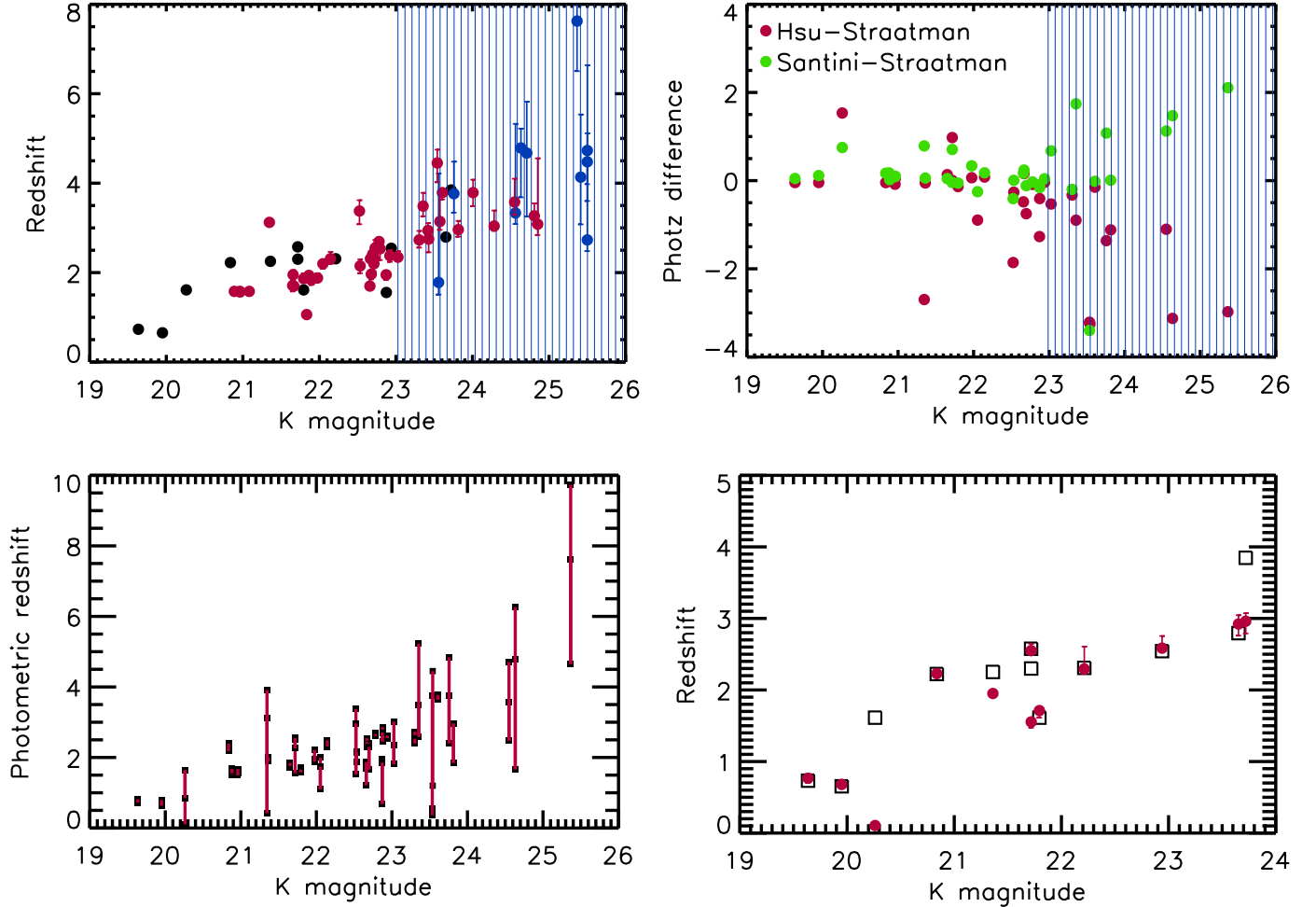


**Figure 14.** Redshift vs.  $K_s$ -band magnitude. *Top left:* Black circles show speczs. Where there are no speczs, red circles show photzs with  $Q < 3$  (high-quality) and blue circles show photzs with  $Q > 3$  (poor) from S16. The error bars show the 95% confidence range for the photzs. In the remaining panels, we use only the high-quality photzs from S16. *Top right:* Red circles show the Hsu et al. (2014) photzs minus the S16 photzs, and green circles show the Santini et al. (2015) photzs minus the S16 photzs. Blue shaded region (this panel and top left panel) shows the  $K_s > 23$  magnitude range above which the photzs become very uncertain. *Bottom left:* For each source, the photzs from all three papers are shown simultaneously (black squares), connected by red lines. *Bottom right:* Even at bright  $K_s < 22$  magnitudes, the photzs do not always reproduce the speczs, as demonstrated over the  $K_s$  range where there are speczs (black open squares); these are compared with the photzs from S16 (red circles).

$K_s < 22$  magnitudes, there are some large discrepancies between the speczs and the photzs.

In Figure 15(a), we show the distribution of  $K_s$  magnitudes for the total ALMA sample (gray shading) and for those sources with speczs (red shading). We show undetected sources at a nominal magnitude of  $K_s = 25.5$ . Three of the sample are undetected in  $K_s$  (sources 13 or ALMA033217-275233, 19 or ALMA033226-275208, and 58 or ALMA033244-275011). These are a subset of the sources that are very faint in the F160W band.

#### 4.4. MIR Counterparts and SMG Color Selections

We obtained  $3.6 \mu\text{m}$  and  $4.5 \mu\text{m}$  fluxes for the total ALMA sample from the S-CANDELS catalog of Ashby et al. (2015), supplemented with S-CANDELS fluxes from NED IPAC for the small number of sources not included in the Ashby et al. catalog. (The latter fluxes do not appear to have been published elsewhere.) We used the  $2''.4$  diameter aperture fluxes, which closely match the  $3.6 \mu\text{m}$  and  $4.5 \mu\text{m}$  fluxes of G13. We restricted to the 60 ALMA sources that are isolated in the S-CANDELS data to avoid photometric contamination. All but one of these sources are detected in both the  $3.6 \mu\text{m}$  and  $4.5 \mu\text{m}$  bands. The remaining source

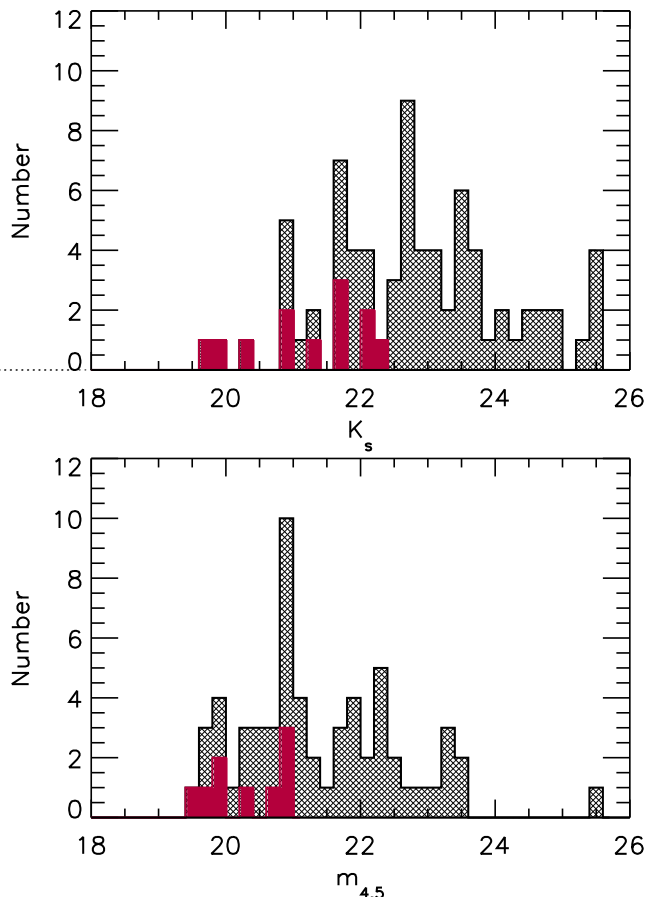


**Figure 15.** Histograms of the (a)  $K_s$  and (b)  $m_{4.5}$  magnitudes for the total ALMA sample. In (b), only the 60 ALMA sources that are isolated in the S-CANDELS data are shown in order to avoid photometric contamination. Undetected sources are shown at 25.5 in both panels. Red shading shows sources with speczs.

(source 75 or ALMA033217-274713) is not detected in either, but this is the faintest of the ALMA sources and may be spurious. In Figure 15(b), we show the distribution of the  $4.5 \mu\text{m}$  magnitudes for the 59 isolated and detected sources, plus the undetected source 75 plotted at a nominal  $4.5 \mu\text{m}$  magnitude of  $m_{4.5} = 25.5$ .

Infrared colors have been used to select high-redshift dusty galaxies (Wang et al. 2012; Chen et al. 2016; Wang et al. 2016). These methods rely on the fact that the colors asymptote at high redshifts (see Figure 4 of Wang et al. 2012), and high values can only be obtained with very large reddening. Wang et al. (2012) used a condition  $K_s - m_{4.5} > 1.6$  (KIEROs), while Wang et al. (2016) used  $m_{160W} - m_{4.5} > 2.25$  (HIEROs). These selections are extremely similar, as can be seen from Figure 16, where we plot  $m_{160W} - m_{4.5}$  versus  $K_s - m_{4.5}$ . For these analyses, in order to obtain optimally matched

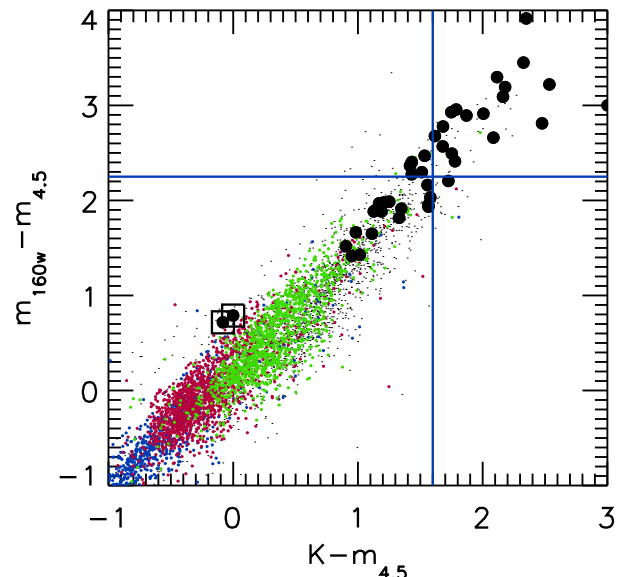


**Figure 16.** Comparison of the HIERO ( $m_{160W} - m_{4.5} > 2.25$ ) and KIERO ( $K_s - m_{4.5} > 1.6$ ) selections (blue lines). The black large circles show the 42 ALMA sources that have measured  $K_s$  magnitudes in the G13 catalog and are isolated in the IRAC bands. The different colored dots show the full GOODS-S data with  $K = 18 - 24$  divided into photometric redshift intervals (blue is  $z = 0 - 0.5$ , red is  $z = 0.5 - 1$ , green is  $z = 1 - 1.5$ , and black for the remainder). The two ALMA sources with specz  $0 < z \leq 1$  are marked with open squares.

fluxes, we use only sources with counterparts in the G13 catalog, and we take all of the magnitudes from this reference. We show the KIEROs and HIEROs selections as blue lines, and we use different colored dots to show the GOODS-S data between  $K_s = 18 - 24$  divided into photometric redshift intervals. We only plot the 42 ALMA sources that have measured  $K_s$  magnitudes in the G13 catalog and are isolated in the IRAC bands (black large circles). We find that 18 of these are selected by the KIEROs criterion, 22 by the HIEROs criterion, and 17 by both.

As an aside, we note that two of the fainter SMGs in Table 4 and Figure 15 (source 66 or ALMA033210-274807 and source 74 or ALMA033222-274935) fall at much bluer colors in Figure 16 and Figure 17 than might be expected. We mark them with open squares in both figures. Both have spectroscopic redshifts ( $z = 0.654$  and  $z = 0.732$ , respectively, with source 66 also being serendipitously detected in CO in BASIC) and bright  $K_s$  magnitudes ( $K_s < 20$ ). These sources lie above the main track of the galaxies in Figure 16 with red  $m_{160W} - K_s$  colors.

In Figure 17, we illustrate the three color selection of Chen et al. (2016) ( $m_{850LP} - K_s > 1.1$ ,  $K_s - m_{3.6} > 1.25$ , and  $m_{3.6} - m_{4.5} > 0.22$ ) by plotting  $m_{3.6} - m_{4.5}$  versus

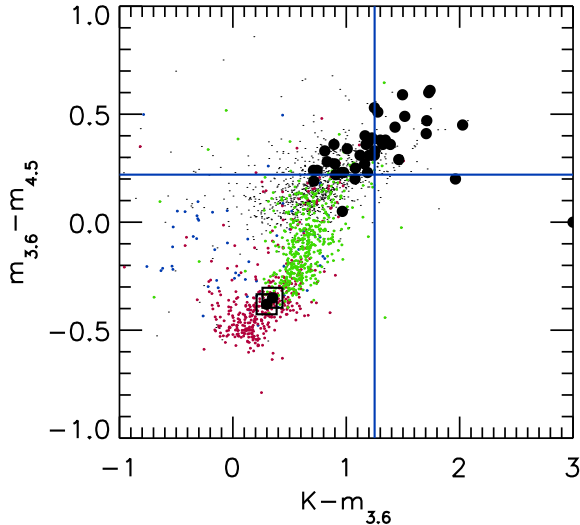


**Figure 17.** Chen et al. (2016) three color selection. Only sources with  $m_{850\text{LP}} - K > 1.1$  are shown. The plotted data are 42 ALMA sources with counterparts in the G13 catalog and that are isolated in the IRAC bands (black large circles), and GOODS-S sources with  $K = 18 - 24$  (dots); the latter are divided into photometric redshift intervals (blue is  $z = 0 - 0.5$ , red is  $z = 0.5 - 1$ , green is  $z = 1 - 1.5$ , and black for the remainder). The remaining two selections ( $K_s - m_{3.6} > 1.25$  and  $m_{3.6} - m_{4.5} > 0.22$ ) are shown by the blue lines. The two ALMA sources with  $\text{spec}z\ 0 < z \leq 1$  are marked with enclosing large open squares.

$K_s - m_{3.6}$  and only showing sources that satisfy  $m_{850\text{LP}} - K_s > 1.1$ . The plotted data are 42 ALMA sources with counterparts in the G13 catalog and that are isolated in the IRAC bands (black large circles), and GOODS-S sources with  $K = 18 - 24$ , divided into photometric redshift intervals (colored dots). We find that 15 of the ALMA sources are selected. These are a subset of the HIEROS selection.

However, the Chen et al. (2016) selection is sensitive to the  $K_s - m_{3.6}$  color and hence to the precise details of the ground-based and *Spitzer* photometry. For instance, Laporte et al. (2017) found a better selection with  $K_s - m_{3.6} > 0.8$  in their ALMA studies of the Frontier Fields. Using  $K_s - m_{3.6} > 1$  would result in 26 of the ALMA sources being selected.

In conclusion, infrared color selection methods are useful for narrowing down the fraction of the population that could be SMGs. However, photometric uncertainties remain a major drawback toward obtaining complete or even representative samples. There is also the issue of how many of the selected sources are not SMGs.

To examine the latter for each of the infrared color selection methods, we consider the GOODS-S region that is covered by the ALMA observations. Here the G13 catalog gives 31 KIEROs and 44 HIEROs with  $K_s$  magnitudes between 18 and 24. Of the 31 KIEROs, we have

ALMA detections for 13, and a further four are detected above a  $2\sigma$  threshold in the SCUBA-2 image cleaned of ALMA sources. In combination, this gives a 55% submillimeter detection rate. Of the 44 HIEROs, we have ALMA detections for 12, and a further seven have  $> 2\sigma$  SCUBA-2 detections. In combination, this gives a 43% submillimeter detection rate.

Likewise, the G13 catalog gives 39 sources for the Chen et al. (2016) three color selection, of which we have ALMA detections for 15, and a further three have  $> 2\sigma$  SCUBA-2 detections. In combination, this gives a 46% submillimeter detection rate. If we relax the three color selection criterion to  $K_s - m_{3.6} > 1$ , as discussed above, then the G13 catalog gives 93 sources, of which we have ALMA detections for 26, and a further 12 have  $> 2\sigma$  SCUBA-2 detections. This reduces the combined detection rate to 41%.

We conclude that all three of the infrared color selection methods are comparable in their SMG selections and contamination rates. We note that the KIEROs method may be more versatile, since it uses only ground-based and *Spitzer* data and hence avoids the need for deep *HST* data.

#### 4.5. FIR Counterparts

All but one source in the total ALMA sample lie within both the deep  $24\ \mu\text{m}$  *Spitzer* MIPS image (Gavalisco et al. 2004) and the deep  $100\ \mu\text{m}$  and  $160\ \mu\text{m}$  *Herschel* PACS images of the GOODS-S (Elbaz et al. 2011). All lie within the deep longer wavelength *Herschel* SPIRE images of the field (Elbaz et al. 2011; Oliver et al. 2012). In Figure 18, we mark the ALMA sources by overlaying open squares on the  $24\ \mu\text{m}$  (left) and  $100\ \mu\text{m}$  (right) images. We exclude the one source that lies at the edge of these images (source 27; red square in Figure 18) from our MIR analysis. This source also lies at the edge of the ACS and CANDELS images (see Section 4.1).

Where possible, we used the catalog from Elbaz et al. (2011) to obtain  $24\ \mu\text{m}$  and  $100 - 500\ \mu\text{m}$  fluxes. We first cross-identified the total ALMA sample against the  $24\ \mu\text{m}$  sources with fluxes  $> 20\ \mu\text{Jy}$ , which are what Elbaz et al. used as priors in measuring the *Herschel* PACS  $100\ \mu\text{m}$  fluxes. Most of the *Herschel* sources have  $24\ \mu\text{m}$  counterparts (Magnelli et al. 2011). We find that 61 of the remaining 74 ALMA sources (after excluding source 27) have a  $24\ \mu\text{m}$  prior in the Elbaz et al. (2011) catalog within a  $1''.5$  radius. This result is not sensitive to the choice of matching radius; for example, we recover the same result with a  $2''.5$  matching radius.

In Figure 18, ALMA sources with  $24\ \mu\text{m}$  fluxes from the Elbaz et al. (2011) catalog of  $> 20\ \mu\text{Jy}$  sources are shown as gold squares, and ALMA sources with measured  $24\ \mu\text{m}$  fluxes fainter than this are shown as blue squares. Many of the latter are also faint at  $100\ \mu\text{m}$ , as seen in the right panel of Figure 18. All very high redshift ( $z > 4$ ) sources within the ALMA sample are likely



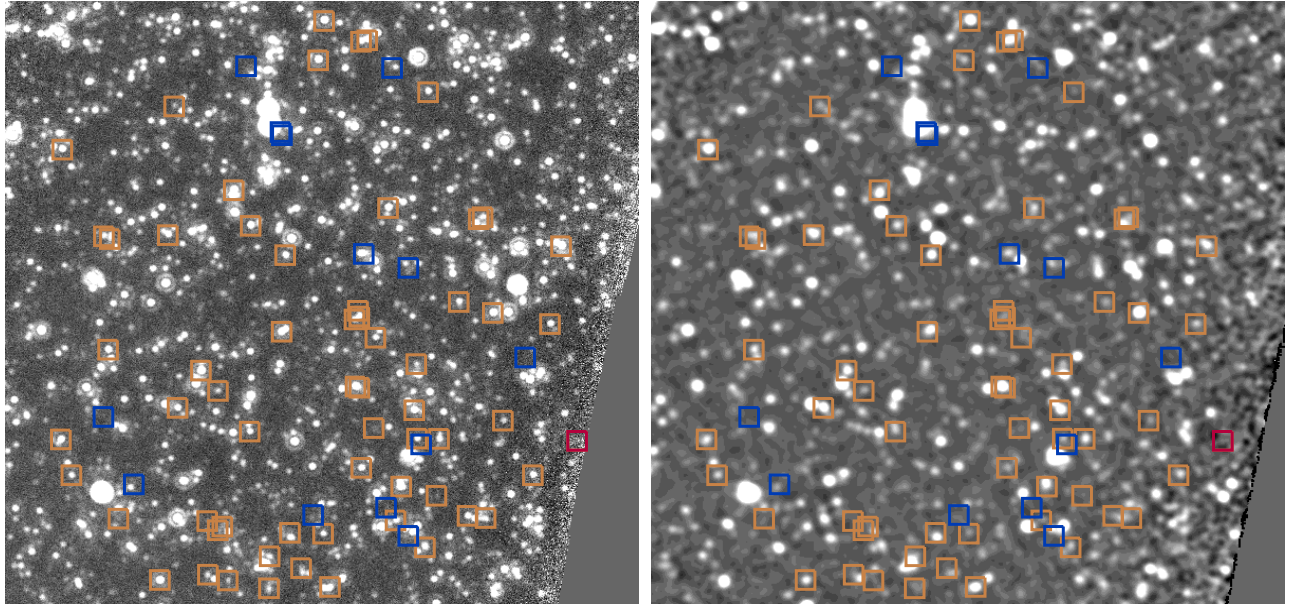


**Figure 18.** Overlay of the ALMA sources on the (*left*)  $24\ \mu\text{m}$  and (*right*)  $100\ \mu\text{m}$  images of the field. Sources with  $24\ \mu\text{m}$  counterparts in the Elbaz et al. (2011) catalog within a matching radius of  $1''.5$  and with fluxes  $> 20\ \mu\text{Jy}$  are shown in gold, while other ALMA sources are shown in blue. As discussed in the text, the differentiation between the blue and gold squares is not sensitive to the choice of matching radius. We exclude one source (27) that lies at the edge of the field; it is shown with a red square.

to be contained in this subsample. We shall return to consider this in detail in the discussion.

For the remaining unmatched sources, we measured fluxes in the  $24\ \mu\text{m}$  images at the ALMA positions using a  $3''$  diameter aperture, and in the longer wavelength data in matched-filter images after first removing the sources in the Elbaz et al. (2011) catalog from the images. We aperture corrected these  $24\ \mu\text{m}$  fluxes to match the measured  $24\ \mu\text{m}$  fluxes in the Elbaz et al. catalog. We excluded four sources (14, 34, 68, and 72) that are contaminated by a neighboring bright source in the  $24\ \mu\text{m}$  sample.

In Figure 19, we show individual images for the eight ALMA sources with an  $850\ \mu\text{m}$  flux  $> 1.65\ \text{mJy}$ , which is roughly the confusion limit of the SCUBA-2 image, and a measured  $24\ \mu\text{m}$  flux  $< 0.02\ \text{mJy}$ . We show *Spitzer* and *Herschel* three color images in the top panels ( $24$ ,  $100$ , and  $160\ \mu\text{m}$ ) and *Herschel* and SCUBA-2 three color images in the bottom panels ( $200$ ,  $350$ , and  $850\ \mu\text{m}$ ). In the top panels, we mark the ALMA sources with white squares and the  $24\ \mu\text{m}$  sources with fluxes  $> 20\ \mu\text{Jy}$  with red squares.

#### 4.6. FIR Photometric Redshifts

In Barger et al. (2012, 2014) and Paper I, we found that almost all of the spectroscopically identified SMGs with fluxes greater than  $2\ \text{mJy}$  in the GOODS-N can be reasonably fit by an Arp 220-like FIR SED. This also appears to be true in the GOODS-S. In Figure 20, we show

the rest-frame SEDs for the 9 uncontaminated sources with secure specz  $z > 1$  and  $24\ \mu\text{m}$  priors (4, 5, 9, 18, 25, 35, 40, 46, and 56). (We excluded from this list source 59 or ALMA033222-274815, which is confused with source 38 or ALMA033222-274811. We also excluded source 1 or ALMA033207-275120, which we discuss below.) Since we are only interested in the relative shapes, we normalized the SEDs to all have a peak flux of  $20\ \text{mJy}$ . We overlay the Arp 220 SED of Silva et al. (1998) in black.

In order to quantify the above, we measured the dust temperatures for each of the nine sources assuming a graybody with an emissivity  $\beta = 1.5$ . We fitted only above a rest-frame wavelength of  $40\ \mu\text{m}$  to minimize the effects of short wavelength power law contributions. In Figure 21, we show these dust temperatures. The mean (median) is  $39.4$  ( $40.3$ ) K, as compared with  $38.6$  K for Arp 220 fitted in the same way. Only one source (source 18 or ALMA033222-274804) has a temperature ( $T = 46.2 \pm 3.4$  K) that is more than  $2\sigma$  different than that of Arp 220. This is the only  $z > 3$  source among the nine. It may be that higher redshift sources are slightly hotter. Otherwise, the sources do not show any clear temperature dependence on the submillimeter flux or on the presence of an X-ray AGN (see Figure 21).

Given this, for the 59 sources with ALMA fluxes above  $1.65\ \text{mJy}$  (this flux limit was chosen to provide high S/N throughout the SED), we used the Arp 220 template to estimate FIR photometric redshifts (hereafter,

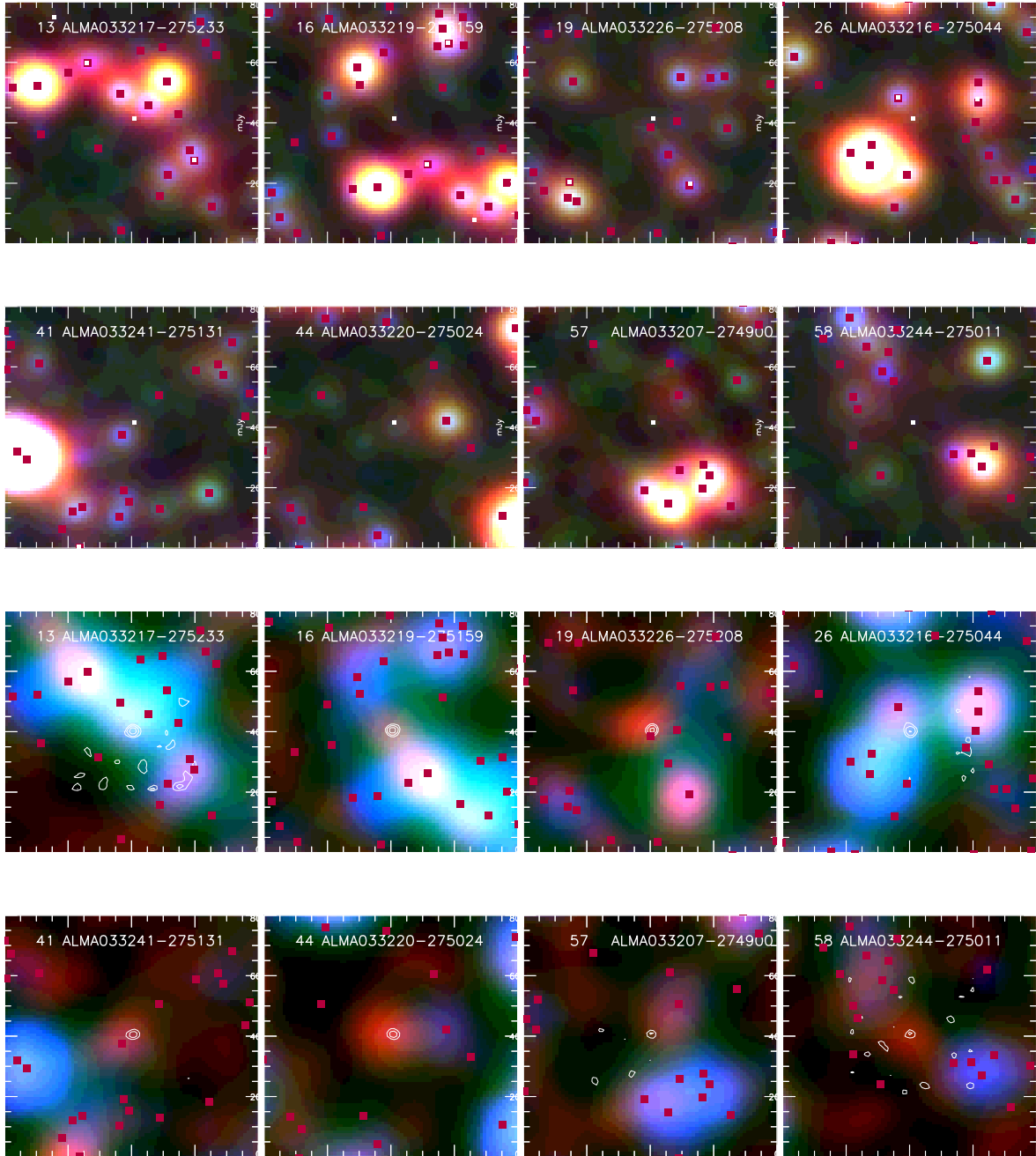


**Figure 19.** *Upper 8 panels:* Three-color *Spitzer* and *Herschel* images (24, 100, and 160  $\mu\text{m}$ ) for the brightest ALMA sources with 24  $\mu\text{m}$  fluxes less than 20  $\mu\text{Jy}$ . The thumbnails are  $80''$  on a side. The ALMA sources are shown with white squares, and the sources in the field with 24  $\mu\text{m}$  fluxes  $> 20 \mu\text{Jy}$  (Elbaz et al. 2011 used these as priors for the *Herschel* PACS 100  $\mu\text{m}$  data) are shown with red squares. We mark the ALMA positions with squares rather than overlaying contours to more clearly show the relative positions of the 24  $\mu\text{m}$  sources. The numbers refer to Table 4. *Lower 8 panels:* Three-color *Herschel* and SCUBA-2 images (250, 350, and 850  $\mu\text{m}$ ) for the same sources as above. The  $0''.5$  FWHM tapered ALMA images are overlaid as white contours at 0.6, 1.2, 2.4, and 4.8 mJy/beam.

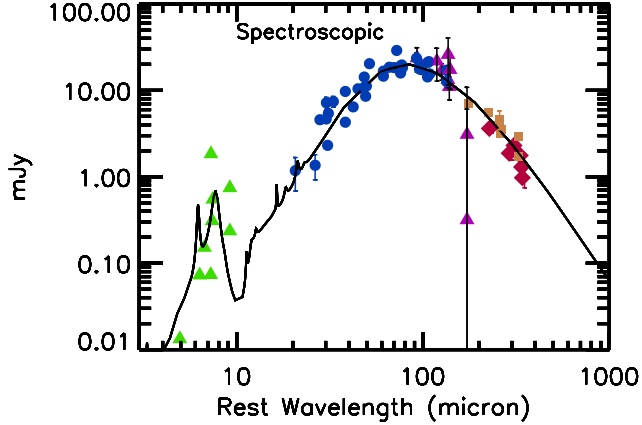


**Figure 20.** Flux vs. rest-frame wavelength for the 9 uncontaminated sources with secure specz  $z > 1$  and  $24 \mu\text{m}$  priors. Gold squares show our ALMA  $850 \mu\text{m}$  fluxes, red diamonds the ALMA  $1.13 \text{ mm}$  fluxes from F18, purple triangles our SCUBA-2  $450 \mu\text{m}$  fluxes, blue circles the *Herschel* fluxes, and green triangles the *Spitzer*  $24 \mu\text{m}$  fluxes. All of the SEDs are normalized to a peak flux of  $20 \text{ mJy}$ . The black overlay shows the Arp 220 SED from Silva et al. (1998).

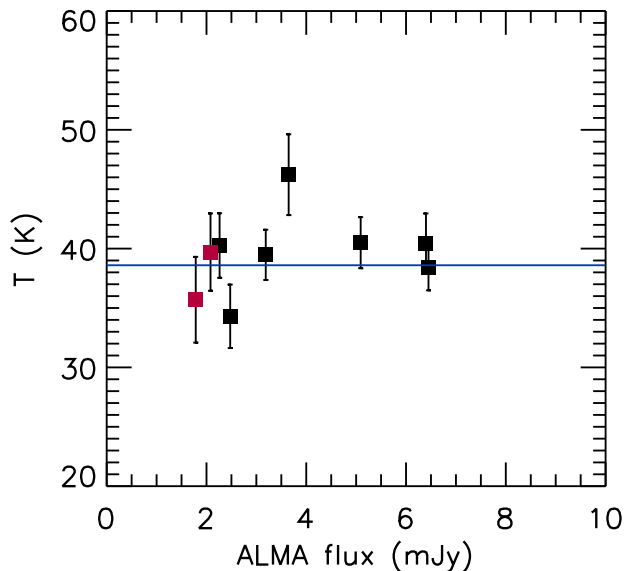


**Figure 21.** Dust temperatures for the 9 uncontaminated sources with secure specz  $z > 1$  and  $24 \mu\text{m}$  priors. The values are derived from a graybody fit with an emissivity  $\beta = 1.5$ , and the error bars are  $1\sigma$  around the best fit value. Only data at rest-frame wavelengths above  $40 \mu\text{m}$  were fitted. The blue line shows the value derived by fitting the Arp 220 SED from Silva et al. (1998) in the same way. Sources with rest-frame  $2 - 8 \text{ keV}$  luminosities above  $10^{43} \text{ erg s}^{-1}$  are shown in red.

FIRzs) using a  $\chi^2$  fit to the combined *Herschel*, SCUBA-2  $450 \mu\text{m}$ , ALMA  $850 \mu\text{m}$ , and F18 ALMA  $1.13 \text{ mm}$  (if available) data for each source. In addition to the measured noise, we also included a systematic error of 20% of the flux to allow for relative calibration errors between the bands. We exclude seven sources (26, 29, 37, 41, 57, 58, and 59) where the  $\chi^2$  fit is poor (probability less than 5%) and where there is likely contamination of the photometry from neighbors. We give the estimated FIRzs in Table 5, together with the 95% confidence range. The range of temperatures for the nine spectroscopic sources discussed above relative to that of Arp 220, which was used in the fitting, would add a further roughly  $\pm 10\%$  error to the FIRzs. In Figure 22, we show two sample fits, one at  $z \sim 2$  and one at  $z \sim 3$ .

For source 1 or ALMA033207-275120, the FIRz of  $z = 3.26$  is significantly higher than the specz of the nearby bright galaxy, which Danielson et al. (2017) place at  $z = 1.539$ . Removing photometric contamination by the bright galaxy in the shorter wavelength *Herschel* bands would only increase our estimate of the FIRz and hence the tension. Given that there is also a significant spatial offset of the bright galaxy and the ALMA source (see Section 4.1 and Figure 10), it is possible that the ALMA detection is of a background source. However, there appears to be an extension of the ALMA emission towards the bright galaxy, which may suggest that we are seeing emission from the bright galaxy, too. We therefore exclude this source from our subsequent analysis.

In Figure 23, we show FIRz versus specz (black circles) or photz (red circles) for sources with ALMA  $850 \mu\text{m}$  fluxes above  $1.65 \text{ mJy}$  and where there is a FIRz and a specz or a photz with quality flag  $Q < 3$  in S16. While there is some scatter, the overall correlation is reasonable for most of the sources. There is one seriously discrepant source (source 17 or ALMA033235-275215) where the FIRz places the galaxy at a very high redshift; we discuss this source in Section 5, together with other sources where the FIRz gives a high redshift but for which there is no reliable photz.

The FIRzs are only based on the SEDs above an observed wavelength of  $100 \mu\text{m}$  (the shortest wavelength *Herschel* data available), and we may compare the results with the shorter wavelength bands from *Spitzer*. Because of the negative  $K$ -correction at  $850 \mu\text{m}$ , we expect both the  $4.5 \mu\text{m}$  to  $850 \mu\text{m}$  flux ratio and the  $24 \mu\text{m}$  to  $850 \mu\text{m}$  flux ratio to drop rapidly with increasing redshift (see also Shu et al. 2016, who considered the  $24 \mu\text{m}$  to  $500 \mu\text{m}$  flux ratio).

In Figure 24, we plot the two ratios versus redshift, along with the expectation from the Arp 220 template (black curve). In the first two panels, we use the speczs (blue circles), then the FIRzs for sources with no specz (red circles), and finally the photzs (blue circles again) for sources with neither a specz nor a FIRz. In the last panel, we show the  $24 \mu\text{m}$  to  $850 \mu\text{m}$  flux ratio

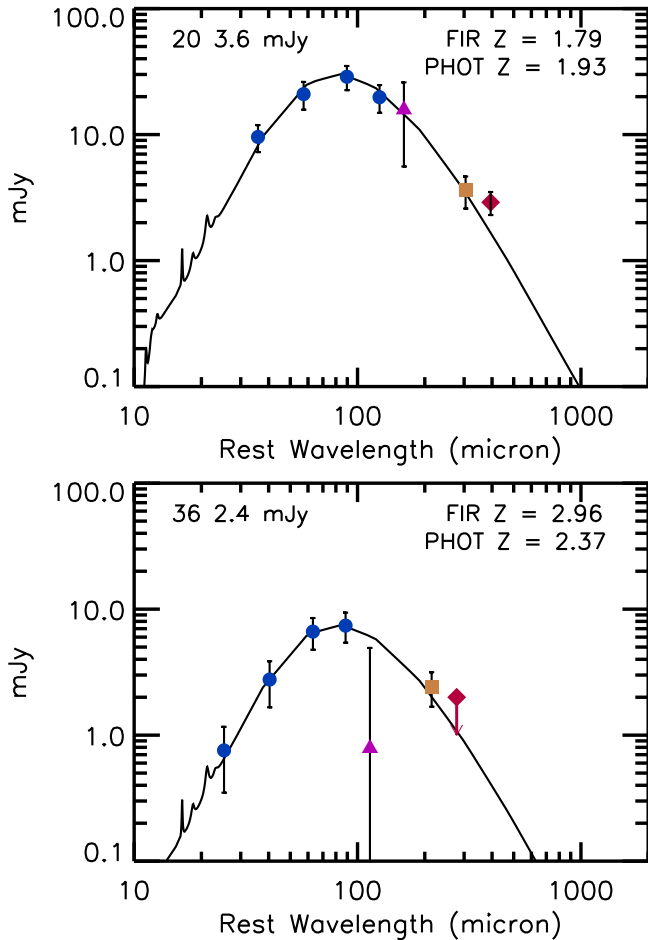


**Figure 22.** Sample fits used to determine the FIRzs, which are listed in the upper right corner of each plot, along with the photzs. Gold squares show our ALMA 850  $\mu\text{m}$  fluxes, red diamonds the F18 or AzTEC 1.1 mm fluxes, purple triangles our SCUBA-2 450  $\mu\text{m}$  fluxes, and blue circles the *Herschel* fluxes. The errors are  $\pm 1\sigma$ . Source 36 or ALMA033220274836 is not in the F18 or AzTEC catalogs, so we show a  $2\sigma$  upper limit (downward pointing arrow) at 1.1 mm based on the AzTEC data. The black overlay shows the Arp 220 template fit.

vs. redshift for a second time, but here we use only the speczs (blue circles) followed by the photzs (green circles). As an aside, we note that for a given redshift, most of the luminous X-ray AGNs (large squares in first panel) have high 24  $\mu\text{m}$  to 850  $\mu\text{m}$  flux ratios; however, there are only four such sources, and the value of one is low.

While the dispersion in the plots is too large to estimate accurate redshifts for individual sources, we see the expected decline with redshift. The highest redshift sources ( $z \gtrsim 4$ ) are faint at both 4.5  $\mu\text{m}$  and 24  $\mu\text{m}$ ,

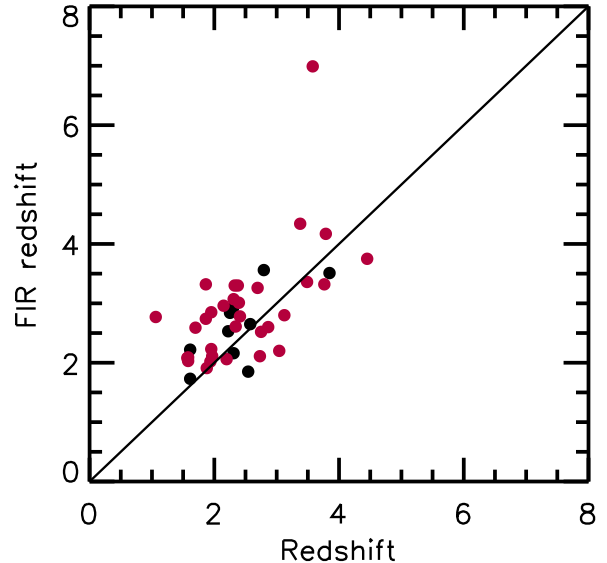


**Figure 23.** Comparison of FIRz with specz (black circles) or photz (red circles). Only sources from the total ALMA sample with fluxes above 1.65 mJy and where there is a FIRz and either a specz or a photz are shown. The one source (source 17 or ALMA033235-275215) with a very high FIRz estimate is shown at a nominal FIRz of 6.9 for clarity. Sources with FIRzs above 4 that do not have reliable photzs are not shown here.

as we illustrate with the horizontal lines plotted at the values of 0.001 (4.5  $\mu\text{m}$  to 850  $\mu\text{m}$  flux ratio plot) and 0.01 (24  $\mu\text{m}$  to 850  $\mu\text{m}$  flux ratio plots). The 24  $\mu\text{m}$  plot is more complex than the 4.5  $\mu\text{m}$  plot, because of the presence of the PAH 8  $\mu\text{m}$  features. At  $z \gtrsim 4$ , the 24  $\mu\text{m}$  band samples rest-frame wavelengths below the 8  $\mu\text{m}$  PAH peak, making the sources very faint.

For the last panel, the potential high-redshift sources seen in the other two panels (based on the FIRzs) are lost, because they do not have high-quality photz estimates. This emphasizes the difficulties with trying to find high-redshift sources using photzs. We conclude that when one has high-resolution 850  $\mu\text{m}$  observations that can be accurately matched to the 4.5  $\mu\text{m}$  or 24  $\mu\text{m}$  images, then one has a strong diagnostic of possible high-redshift sources without the need for a full long-wavelength SED.

## 5. CANDIDATE HIGH-REDSHIFT SOURCES

In Figure 25, we show redshift distributions for the sources in the total ALMA sample above 1.65 mJy (gray shading) and above 3 mJy (red shading). In the top panel, where there is a specz (except for source 1 or ALMA033207-275120; see Section 4.6), we use this, then the FIRz, and finally the photz. The median redshift is  $z = 2.74$ , while above 3 mJy, the median redshift is  $z = 3.26$ . In the bottom panel, we use only the speczs

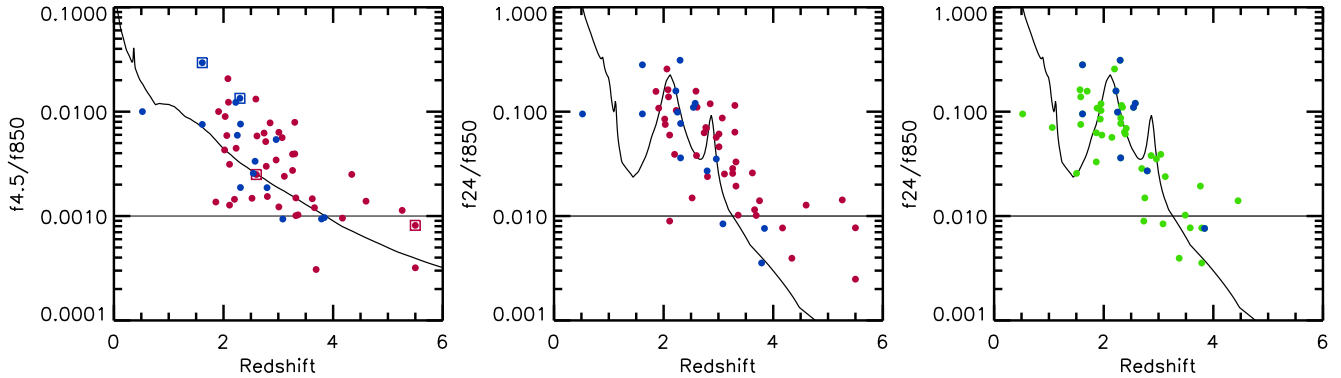


**Figure 24.** (a)  $4.5 \mu\text{m}$  to  $850 \mu\text{m}$  and (b)  $24 \mu\text{m}$  to  $850 \mu\text{m}$  flux ratios vs. redshift. We use specz (blue circles) where possible, then FIRzs (red circles), and finally photzs (blue circles). Sources with  $z > 5.5$  are shown at a nominal  $z = 5.5$ . In (a), we enclose sources with rest-frame  $2 - 8 \text{ keV}$  luminosities above  $10^{43} \text{ erg s}^{-1}$  in large squares. (c)  $24 \mu\text{m}$  to  $850 \mu\text{m}$  flux ratio vs. redshift, where this time we show only the specz (blue circles) or the photzs (green circles). In each panel, the black curve shows the path of the Arp 220 template with redshift, and the horizontal line shows the rough value of the ratio that can be used to select high-redshift sources.

and photzs. The median redshift is  $z = 2.32$ , while above  $3 \text{ mJy}$ , the median redshift is  $z = 2.86$ .

The FIRzs show a number of high redshifts for sources where the photzs are of poor quality ( $Q > 3$  from S16). The FIRzs place six of the sources with  $850 \mu\text{m}$  fluxes above  $1.65 \text{ mJy}$  at  $z > 4$  and two at  $z > 5.5$  (the latter are shown at a nominal redshift of  $z = 5.7$  in the figure). The photzs place seven sources at  $z > 4$ , though six of these are of poor quality. Only one source (source 19 or ALMA033226-275208) is found by both to be at  $z > 4$ .

We consider the six FIRz selected sources and the one high-quality photz (source 2 or ALMA033211275212) to be the most likely high-redshift candidates in the sample. We summarize the properties of these seven sources in Table 6, where we give the ratios of the  $4.5$ ,  $24$ ,  $100$ , and  $250 \mu\text{m}$  fluxes to the ALMA  $850 \mu\text{m}$  flux, the  $2 - 7 \text{ keV}$  flux, and the 95% confidence ranges for the photzs and the FIRzs. Source 17 or ALMA033235-275215 is an AGN, which we discuss further in Section 8. The most compelling very high-redshift candidate is source 19, where both the poor quality photz and the FIRz estimate are consistent within the uncertainties with  $z > 6$ . We show the full SED of this source in Figure 26. While they were not chosen in this way, all of the candidates have low flux ratios in  $24/850$  (at or near 0.01) and  $4.5/850$  (at or near 0.001), consistent with the high-redshift interpretation (see Section 4.6).

## 6. FLUX DEPENDENCE OF REDSHIFTS AND STAR FORMATION HISTORY

In Figure 27, we show the median redshift with 68% confidence as a function of  $850 \mu\text{m}$  flux for the total ALMA sample (red large circles) and for the wider sample of 186 sources in the GOODS-N (blue large circles; Paper I). We also show the individual data points for each sample (small circles). For the total ALMA sample, we plot sources that the FIRzs place at  $z > 5.5$  at

a nominal redshift of  $z = 5.7$ . The GOODS-N redshifts contain a much higher fraction of specz, including a number at  $z > 4$ , while the other redshifts for this field are based solely on the ratio of the  $250 \mu\text{m}$  to  $850 \mu\text{m}$  flux. The upper envelope seen in the figure consists of galaxies that have only a lower ( $2\sigma$ ) limit on the redshift. We show these with upward pointing arrows.

A least-squares fit to the individual data points in the combined samples gives the relation (black line in Figure 27)

$$z_{\text{median}} = 2.40 + 0.09(\pm 0.03) \times S_{850} \text{ (mJy)}. \quad (1)$$

This is consistent with the Equation 7 relation given in Paper I. The redshift distribution is clearly increasing with increasing flux. A Mann-Whitney test gives only a 0.05% probability that the combined  $4 - 16 \text{ mJy}$  sample is drawn from the same redshift distribution as the combined  $2 - 4 \text{ mJy}$  sample. These results are broadly consistent with recent modeling by Béthermin et al. (2015), who find lower redshift distributions for lower fluxes.

However, there are significant issues of cosmic variance with GOODS field sizes, and it is possible there may be evolution in the dust temperature with redshift (see, e.g., Schreiber et al. 2018 and also Section 4.6), which could change the redshift estimates. We postpone a more detailed discussion of this issue to a later paper in the series.

The total ALMA sample is still relatively small, and we postpone a more detailed discussion of the SFR density history to A. Barger et al. (2018, in preparation), where we combine the full SCUBA-2 samples from both fields. Here we simply show that the star formation history computed from the ALMA sources is fully consistent with that derived from the GOODS-N observations in Paper I.

In Figure 28, we plot the SFR density history for sources above  $2 \text{ mJy}$  in the GOODS-N (red circles). The

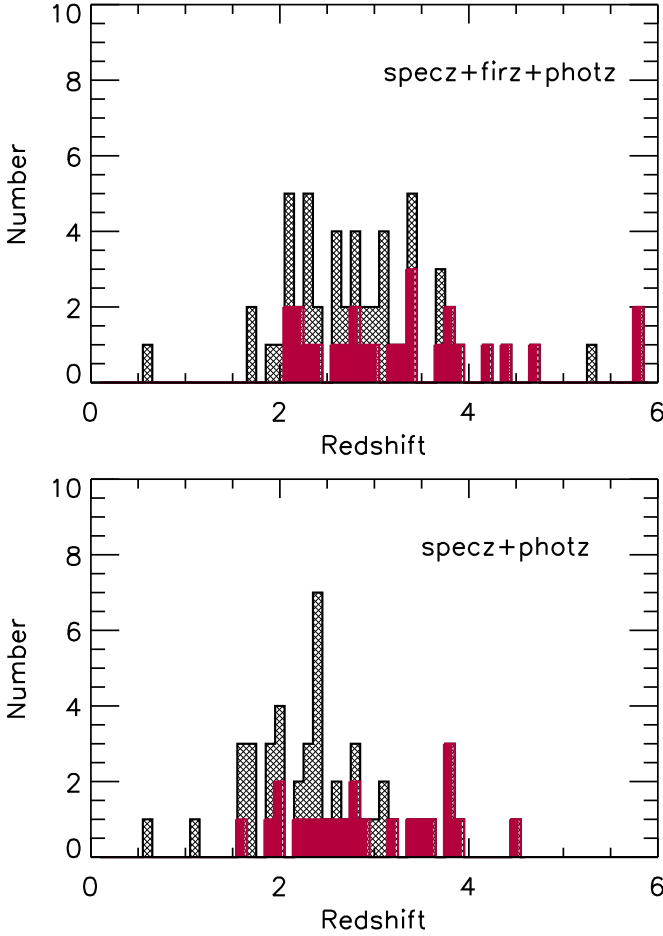


**Figure 25.** Redshift distributions for the sources in the total ALMA sample with fluxes above 1.65 mJy (gray shading). The red shading shows the distributions for sources brighter than 3 mJy. *Top:* We use speczs where possible, then FIRzs, and finally photzs, providing redshifts for 55 sources above 1.65 mJy and 25 above 3 mJy. Very high-redshift sources (FIRzs  $> 5.5$ ) are shown at a nominal value of  $z = 5.7$ . *Bottom:* We use only the speczs and photzs, providing redshifts for 47 sources above 1.65 mJy and 22 above 3 mJy.

computations were made at  $z = 1 - 2$ ,  $2 - 3$ ,  $3 - 4$ ,  $4 - 5$ , and  $5 - 6$  and are plotted at the mean redshift of each bin. After adding the total ALMA sample using the same redshift intervals to the figure (gold circles), we can see that, within the uncertainties, the ALMA values are consistent with the GOODS-N values.

As noted in Paper I, above  $z \sim 2$ , the SFR density history corresponds to 40% (red curve) of the total SFR density history compiled by Madau & Dickinson (2014), after converting their adopted Salpeter (1955) IMF to a Kroupa (2001) IMF (blue curve). However, as described in Paper I, we also need to take into account Paper I's

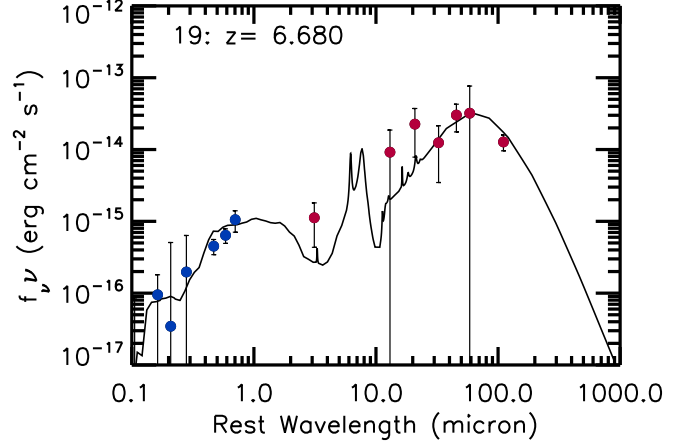


**Figure 26.** Fit to the SED of source 19 or ALMA033226-275208 shown in the frame of the FIRz fit. The blue circles show the data on which the photz is based, and the red circles the data on which the FIRz is based. We show the Arp 220 SED for comparison (black curve).

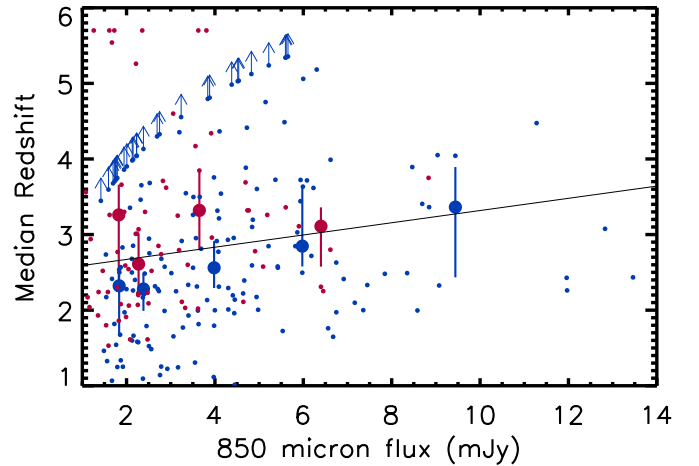


**Figure 27.** Median redshift vs. 850  $\mu\text{m}$  flux for the total ALMA sample (red large circles) and the wider GOODS-N sample (blue large circles; Paper I). The error bars show the 68% confidence intervals on the medians. The smaller circles indicate individual sources. The blue points with upward pointing arrows correspond to  $2\sigma$  lower limits on the redshifts in the GOODS-N sample. The black line shows a linear least squares fit (Equation 1) to the combined samples.

conversion from  $L_{8-1000 \mu\text{m}}$  to SFR, namely,

$$\log \text{SFR}(M_{\odot} \text{ yr}^{-1}) = \log L_{8-1000 \mu\text{m}} (\text{erg s}^{-1}) - 43.41, \quad (2)$$

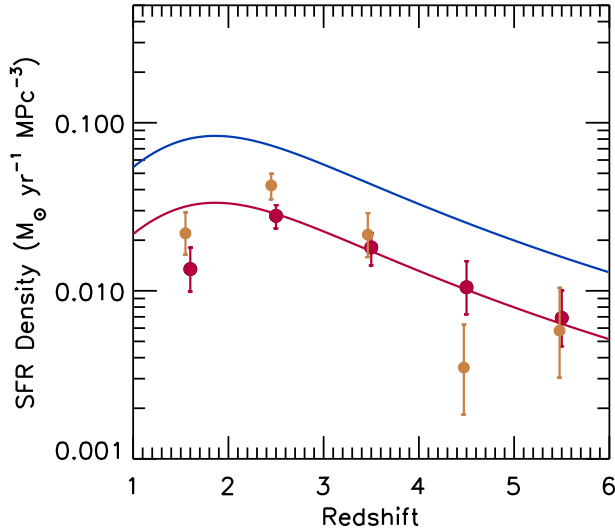


**Figure 28.** SFR density per unit comoving volume vs. redshift for the total ALMA sample for a Kroupa (2001) IMF (gold circles; the  $1\sigma$  error bars are Poissonian based on the number of sources in each bin). The computations were made at  $z = 1 - 2$ ,  $2 - 3$ ,  $3 - 4$ ,  $4 - 5$ , and  $5 - 6$  and are plotted at the mean redshift of each bin. The blue curve shows the SFR density history computed by Madau & Dickinson (2014), after conversion to a Kroupa IMF. We also show the SFR density history for sources above 2 mJy in the GOODS-N (Paper I; red circles), which we matched by multiplying the Madau & Dickinson results by 0.4 (red curve). However, once we take into account the different FIR calibrations used in both works, the GOODS-N data are only 0.29 times the Madau & Dickinson curve.

when comparing to Madau & Dickinson, who used a slightly lower conversion of  $-43.55$  (after the IMF conversion). Once we do so, then we find that the GOODS-N and GOODS-S data are only 0.29 times the Madau & Dickinson curve.

## 7. MORPHOLOGIES AND MERGERS

The total ALMA sample is the largest existing sample with deep optical and NIR data from *HST*, with roughly double the number of sources in the ALESS based sample of Chen et al. (2015; though five of the brightest sources overlap with the Chen et al. sample) and much more extensive wavelength coverage. The bulk of the ALMA sources are detected in the F160W band, which is the longest wavelength with high spatial resolution imaging.

In Figure 29, we show the  $850\ \mu\text{m}$  flux distribution for the 74 ALMA sources (again excluding source 27 or ALMA033203-275039, which lies off the *HST* images). We use red shading to indicate the sources that are either undetected in F160W (sources 2, 19, 44, 61, 68, 75) or whose F160W counterparts may be misidentifica-

tions (sources 1, 11, 13, 58, 64). Although the latter are substantially overlapped with the sources whose separations between the F160W peak flux and the ALMA position are  $> 0''.4$ , as discussed in Section 4.1, not all of those sources are included here, since, in some cases, the galaxy still extends across the ALMA emission (e.g., source 14 or ALMA033222-274936 and source 32 or ALMA033211-274615; see Figure 10). We note that source 11 or ALMA033219-275214 has two low-redshift sources in its vicinity, neither of which is likely the correct counterpart. We hereafter refer to these 11 sources as our undetected sample.

We do not detect at F160W 29% (68% confidence range 15–51%) of the sources above 4 mJy, and 12% (68% confidence range 7–18%) of the sources below 4 mJy. If we take the 5 sources where we suspect we do not have the correct counterpart out of the undetected category, then we do not detect at F160W 7% (68% confidence range 1–23%) of the sources above 4 mJy and 8% (68% confidence range 5–14%) of the sources below 4 mJy. In either case, we do not see any significant increase in the fraction of undetected sources as we move to lower submillimeter fluxes. This differs from Hodge et al. (2013) and Chen et al. (2015), who found a substantial increase in the fraction of F160W undetected sources in the ALESS sample at fainter fluxes relative to higher fluxes. Quantitatively, Chen et al. (2015) found that 36% (68% confidence range 25–52%) of the  $850\ \mu\text{m}$  sources below 4 mJy were undetected, which is significantly higher than measured here. However, all of the samples are small, and the depth of the F160W observations may also affect the results. Larger samples are clearly required to resolve the issue of whether the fraction of F160W faint sources increases with decreasing submillimeter flux.

Even with the very deep F160W data, morphological classification of the galaxies is extremely difficult. This is true whether we use visual or automated classification schemes (Chen et al. 2015). In the present paper, we only visually classify the galaxies. We postpone a quantitative morphological analysis to L. Jones et al. (2018, in preparation).

We find that, in addition to the undetected sample, the F160W images of a further 11 galaxies are too faint to classify ( $m_{160} > 25$ ). This leaves 52 galaxies that we can morphologically classify, of which 24 show what appears to be clear evidence of merging in the F160W images, either as extended tidal tails, multiple nuclei with bridges, or highly asymmetric images. Some sources, such as the ring galaxy (source 23 or ALMA033237-275000) or the extended tidal tail galaxy (source 43 or ALMA033220-275247), are impressive examples of merging, while other sources are more subtle, and the subjective nature of the classification should be kept in mind. In particular, multiple nuclei may be confused with clumpy disks.

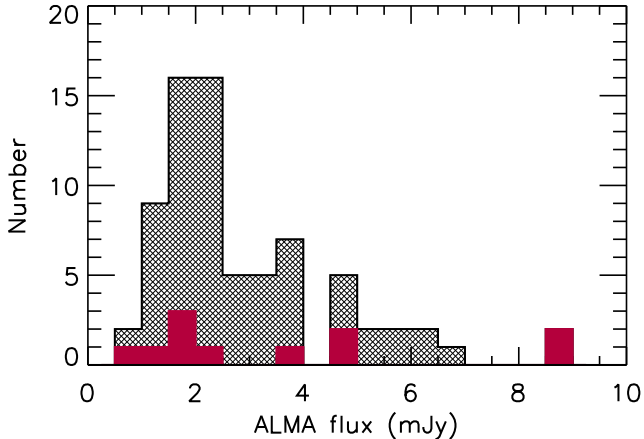


**Figure 29.** Histogram of the  $850\ \mu\text{m}$  flux distribution of the total ALMA sample (gray shading), excluding source 27 or ALMA033203-275039. The red shading shows the distribution of the 11 sources without F160W counterparts.

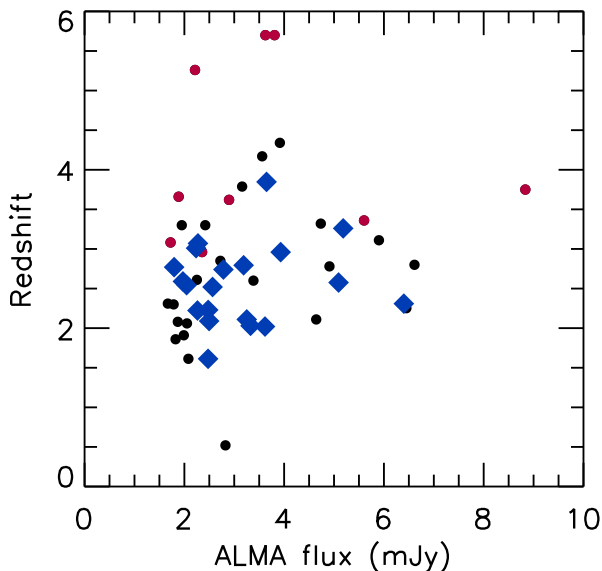


**Figure 30.** Redshift vs.  $850\ \mu\text{m}$  flux for the sources in the total ALMA sample with fluxes above  $1.65\ \text{mJy}$ , excluding only the 5 sources whose F160W counterparts we consider to be misidentifications (sources 1, 11, 13, 58, 64). We use speczs when available, followed by FIRzs, then photzs. We used the  $1.65\ \text{mJy}$  flux limit, because only those sources have FIRzs. Red circles show sources whose F160W fluxes are too faint to classify, blue diamonds sources with a merger signature, and black circles the remaining sources.

To illustrate which sources can be classified, in Figure 30, we show redshift versus flux for the sources in the total ALMA sample with fluxes above  $1.65\ \text{mJy}$ , excluding only the 5 sources whose F160W counterparts we consider to be misidentifications (sources 1, 11, 13, 58, 64). We restricted to fluxes  $> 1.65\ \text{mJy}$ , because sources fainter than that do not have FIRzs. We show the galaxies that are too faint to classify with red circles. These galaxies lie at  $z \gtrsim 3$ , where the observed  $1.6\ \mu\text{m}$  corresponds to a rest-frame wavelength that lies below the  $4000\ \text{\AA}$  break. Chen et al. (2015) found a similar result for their ALESS sample and hence truncated their sample to consider only  $z < 3$  galaxies. We did not make such a redshift cut, but we restricted to the sources that can be classified. In practice, as the figure shows, the two selections are very similar. The blue diamonds show the sources with clear evidence of merging. The remaining galaxies (black circles) we have not attempted to classify, noting only that they are primarily extended and contain a mixture of smooth and irregular structures. Only one source (source 26 or ALMA033216-275044) appears compact based on the SExtractor star-galaxy classifier. However, we note the curious chain galaxy (Cowie et al. 1995) structure of source 22 or ALM033244-274635. While this may be a chance projection, the morphologies of the components are curiously similar, and the sequence terminates in the ALMA source. Barger et al. (2012) noted a similar source in the GOODS-N (GOODS-7). It is possible that these sources are sequential star formers, with the SMG being the most recently formed stage.

Overall, we obtain a merger fraction of 44% (68% confidence range 35–53%). The errors are Poissonian based on the number of sources and do not include uncertainties in the classifications. We should also bear in mind that at least some of the unclassified sources may also be mergers.

The merger fraction is smaller if we consider only the sources with  $850\ \mu\text{m}$  fluxes  $> 4\ \text{mJy}$ . Here we have 3 mergers out of 10 classified sources, or a merger fraction 25% (68% confidence range 12–49%).

Our high merger fraction is at odds with recent quantitative analyses, which have generally found the SMGs to be massive disks (e.g., Targett et al. 2013) and not preferentially major mergers (Swinbank et al. 2010). As Chen et al. (2015) argue, the quantitative methods can miss many merging or disturbed sources, which are easily distinguished in a visual inspection. It is not straightforward to directly compare our results with Chen et al., who only give the fraction of disturbed (irregular or merging systems) rather than attempting to distinguish mergers. However, their high fraction of such systems (82%) also suggests that mergers are common. However, once again, we emphasize the uncertainties in the classifications. It is likely that this issue will only be resolved with JWST.



A detailed comparison of the ALMA sizes and morphologies with the optical and NIR images of the galaxies is given in J. González-López et al. (2018, in preparation).

### 8. X-RAY LUMINOSITIES AND AGN ACTIVITY VS. STAR FORMATION

The total ALMA sample lies in the deepest region of the 7 Ms *Chandra* X-ray exposure (Luo et al. 2017). At the largest off-axis angle for the ALMA sources, the detection threshold in the Luo et al. catalog is  $10^{-16}$  erg cm $^{-2}$  s $^{-1}$  in the 2 – 7 keV band, and  $2 \times 10^{-17}$  erg cm $^{-2}$  s $^{-1}$  in the deeper 0.5 – 2 keV band. In the centermost regions, the detection threshold is roughly three times lower than these values. Just over half (41) of the ALMA sources are detected in the Luo et al. catalog using a 1''5 matching radius: 39 are detected in the 0.5 – 2 keV band, and 24 are detected in the shallower 2 – 7 keV band. Only two sources are detected in the 2 – 7 keV band and not in the 0.5 – 2 keV band. The matching is relatively insensitive to the choice of radius. If we instead used a 1''0 radius (based on the  $2\sigma$  positional uncertainties of the fainter *Chandra* sources in the Luo et al. region), then we would only reduce the number of matches by one source.

In Figure 31, we show the observed 0.5 – 2 keV flux versus the 850  $\mu$ m flux for the total ALMA sample. The black line shows the soft X-ray flux limit above which sources would have been included in the Luo et al. (2017) catalog. The green dotted line shows the same for the 2 Ms CDF-N (Xue et al. 2016), and the blue dashed line for the 4 Ms CDF-S (Xue et al. 2011). We see immediately that the bulk of the X-ray counterparts to the ALMA sources could only be detected in a field as deep as the 7 Ms image. At 2 Ms, where the flux limits are 3.5 times higher, most of the sources would be missed.

We note that the fraction of detected sources is much higher at higher submillimeter fluxes. Above 4 mJy, 12 of the 14 ALMA sources have X-ray counterparts (86%, with a 68% confidence range 67–95%), while below this, it drops to 29 out of 61 (48%, with a 68% confidence range 38–57%). (See also Ueda et al. 2017.) The dependence on the submillimeter flux suggests that we are seeing either star formation contributions to the X-ray emission or enhanced AGN activity in the stronger SMGs.

Given that the median redshift of the ALMA sources is just below  $z = 3$  (we have used the specz, if available, followed by the FIRz, and then the photz), we compute the rest-frame 2 – 8 keV luminosities,  $L_{2-8 \text{ keV}}$ , from the observed-frame 0.5 – 2 keV fluxes with no absorption correction and  $\Gamma = 1.8$  using

$$L_{2-8 \text{ keV}} = 4\pi d_L^2 f_{0.5-2 \text{ keV}} ((1+z)/4)^{\Gamma-2} \text{ erg s}^{-1}. \quad (3)$$

Using the 0.5 – 2 keV flux to calculate the 2 – 8 keV luminosities minimizes the  $K$ -corrections for sources at

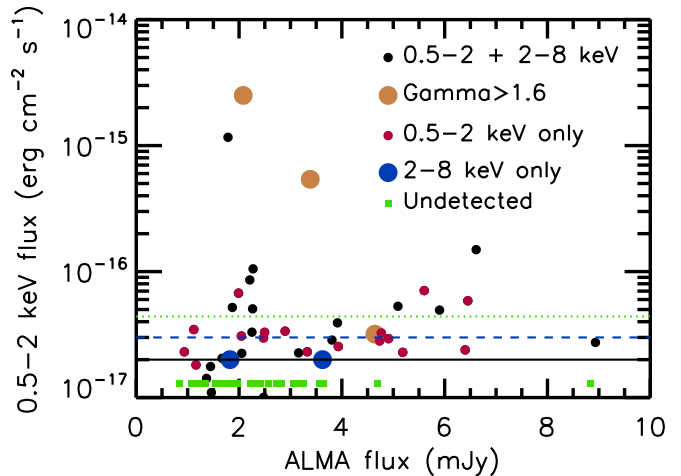


**Figure 31.** 0.5 – 2 keV flux vs. 850  $\mu$ m flux for the total ALMA sample. Black circles show sources detected at both 0.5 – 2 keV and 2 – 7 keV, with those having  $\Gamma > 1.6$  denoted by gold large circles. Red circles show sources detected only at 0.5 – 2 keV, and blue large circles show sources detected only at 2 – 7 keV and placed at a nominal soft flux limit of  $2 \times 10^{-17}$  erg cm $^{-2}$  s $^{-1}$ . This is the 7 Ms CDF-S detection threshold from Luo et al. (2017; black line). The 4 Ms CDF-S flux detection threshold from Xue et al. (2011; blue dashed line) and the 2 Ms CDF-N flux detection threshold from Xue et al. (2016; green dotted line) are shown for comparison. Sources not detected in either band are shown as green squares at a nominal flux of  $1.3 \times 10^{-17}$  erg cm $^{-2}$  s $^{-1}$ .

these redshifts. This is important, given the variation in  $\Gamma$ . We take  $L_{2-8 \text{ keV}} > 10^{44}$  erg s $^{-1}$  as the threshold for a source to be classified as an X-ray quasar.

The poorer sensitivity 2 – 7 keV observations probe higher luminosities. They correspond to higher rest-frame energies,

$$L_{8-28 \text{ keV}} = 4\pi d_L^2 f_{2-7 \text{ keV}} ((1+z)/4)^{\Gamma-2} \text{ erg s}^{-1}. \quad (4)$$

We expect the X-ray binaries produced during star formation to have soft X-ray photon indices. (Sazonov & Khabibullin 2017 give an X-ray photon index of  $2.1 \pm 0.1$  for the collective X-ray spectrum of luminous high-mass X-ray binaries.) Thus, in Figure 32, we plot  $L_{2-8 \text{ keV}}$  versus ALMA flux for the sources in the total ALMA sample that are detected only in the 0.5 – 2 keV band, or, if detected in both bands, have  $\Gamma > 1.2$ , or are not detected in either band (shown as upper limits).

Combining the SFR versus X-ray luminosity relation of Mineo et al. (2014) with the SFR versus 850  $\mu$ m flux relation of Barger et al. (2014) gives the relation (plotted as the black curve in Figure 32)

$$L_{2-8 \text{ keV}} = 3 \times 10^{41} f_{850}(\text{mJy}) \text{ erg s}^{-1}. \quad (5)$$

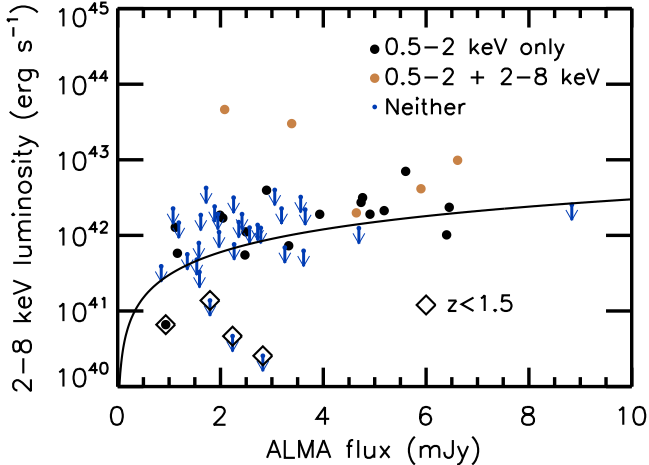


**Figure 32.** Rest-frame 2–8 keV luminosity vs. 850  $\mu\text{m}$  flux for sources in the total ALMA sample that do not have hard X-ray spectra. Black circles show sources detected at 0.5–2 keV but not at 2–7 keV. Gold circles show sources with detections in both bands but having  $\Gamma > 1.2$ . Blue downward pointing arrows show upper limits for sources not detected in either X-ray band, assuming the Luo et al. (2017) catalog 0.5–2 keV flux detection threshold of  $2 \times 10^{-17}$  erg  $\text{cm}^{-2}$   $\text{s}^{-1}$ . Sources with  $z < 1.5$  are marked with open diamonds. Black curve shows the relation between  $L_{2-8 \text{ keV}}$  and 850  $\mu\text{m}$  flux for star-forming galaxies discussed in the text (Equation 5).

Since the submillimeter flux is not linearly related to the SFR at  $z \lesssim 1.5$ , we mark the low-redshift sources in Figure 32 with open diamonds; nearly all the other sources are consistent with the star formation relation. This suggests that the 7 Ms *Chandra* X-ray exposure is finally deep enough to start to probe the star formation taking place in the most intensely star-forming galaxies in the universe. However, two of the  $\Gamma > 1.2$  sources detected in both bands (two of the gold circles; source 22 or ALMA033244274635 and source 46 or ALMA033225274219) are too luminous to be interpreted in this way and appear to be relatively unobscured AGNs.

Of the 24 ALMA sources with hard band detections, we show 21 in Figure 33, excluding the three sources found to be consistent with being star-forming galaxies from Figure 32 (i.e., the gold circles that lie relatively close to the black curve). We plot rest-frame 8–28 keV luminosity versus 850  $\mu\text{m}$  flux for the 21 sources. We summarize the properties of these 21 sources in Table 7.

The flux detection threshold in the 2–7 keV band corresponds to a luminosity threshold of near  $10^{43}$  erg  $\text{s}^{-1}$  for all but the lowest redshift sources. This is well above the luminosity that could be accounted for by star formation based on the Mineo et al. (2014) relation (black

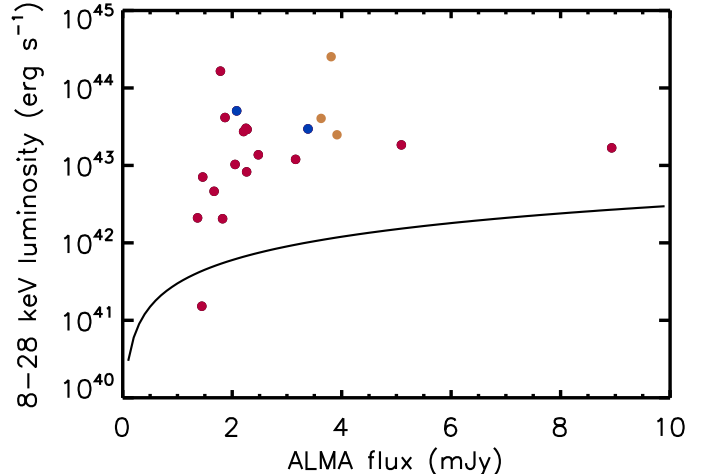


**Figure 33.** Rest-frame 8–28 keV luminosity for 21 of the 24 ALMA sources detected in the observed-frame 2–7 keV band, excluding the three sources found to be consistent with being star-forming galaxies from Figure 32. Blue circles show relatively unobscured sources ( $\log N_H < 22 \text{ cm}^{-2}$ ), and gold circles show potentially Compton thick sources (also high redshift; see text). The remaining sources are shown in red. Black curve shows the relation between  $L_{2-8 \text{ keV}}$  and 850  $\mu\text{m}$  flux for star-forming galaxies discussed in the text (Equation 5).

curve), which does not change appreciably for higher X-ray luminosities. The lowest luminosity source is the low-redshift source 66 or ALMA033210-274807, which has a spectroscopic redshift of  $z = 0.654$ . Its optical spectrum is characteristic of a star-forming galaxy and does not show any AGN signatures. We will consider it to be a star-forming galaxy subsequently.

Of the remaining 20 sources, most are moderate luminosity AGNs that lie just above the detection threshold. The optical spectra for two (source 9 or ALMA033235-274916 and source 46 or ALMA033225-274219) classify them as type 2 AGNs, and for two others (source 40 or ALMA033231-274623 and source 59 or ALMA033222-274815) as star-forming galaxies. For these last two galaxies we do not see AGN signatures in the optical spectra. Only two have quasar luminosities (source 17 or ALMA033235-275215 and source 56 or ALMA033225-274305). For source 17, such a high luminosity is a consequence of the high-redshift FIRz (see Section 5).

Most are also substantially obscured ( $\log N_H \gg 22 \text{ cm}^{-2}$ ) but not Compton thick. Only two are unobscured (blue circles in Figure 33), and only the two potentially high-redshift ones (source 17 and source 19 or ALMA033226-275208; see Section 5) could be Compton thick (gold circles), though this depends on the FIRzs being correct for these sources.

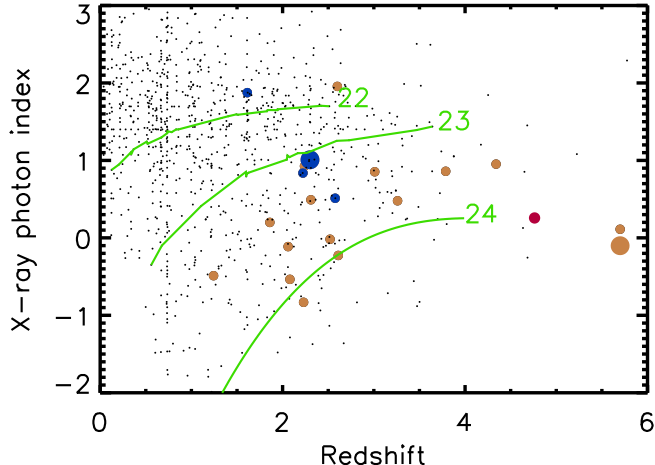


**Figure 34.** Distribution of X-ray photon index vs. redshift for 20 of the 24 ALMA sources detected in the 2–7 keV band, excluding the three sources found to be consistent with being star-forming galaxies from Figure 32 and the one low-redshift source below the star formation relation in Figure 33 with a star-forming galaxy optical spectrum. Gold circles denote sources with a FIRz or a photz, and blue circles denote those with a specz. Sources with a very high redshift FIRz estimate are shown at a nominal redshift of 5.7. Larger circles show sources with quasar X-ray luminosities. The black dots show the full Luo et al. (2017) sample. The green curves from top to bottom show absorption of  $\log N_H = 22, 23,$  and  $24 \text{ cm}^{-2}$ .

We show this in more detail in Figure 34, where we plot X-ray photon index versus redshift for the 20 sources. Larger symbols denote the two sources with quasar luminosities. Sources with a specz are denoted by blue circles, and sources with a FIRz or a photz are denoted by gold circles. We also show all of the sources from the Luo et al. (2017) catalog using the redshifts from their catalog (black dots), distinguishing the Gilli et al. (2011) high-redshift, Compton thick source with a red circle. The green curves correspond to obscuring column densities of  $\log N_H =$  (top curve), 23 (middle), and  $24 \text{ cm}^{-2}$  (bottom).

Nearly all of the submillimeter sources lie at positions consistent with  $\log N_H = 23 - 24 \text{ cm}^{-2}$ , and the median  $\log N_H$  of the sample is  $23.5 \text{ cm}^{-2}$ . Only the two potentially high FIRz sources (17 and 19) would be identified as Compton thick. Indeed, a substantial fraction (17%) of the 106 hard X-ray selected AGNs with  $\log N_H > 23 \text{ cm}^{-2}$  in the central SCUBA-2 region are detected in the submillimeter, while none of the 90 hard X-ray sources in the region with  $\log N_H = 22 - 23 \text{ cm}^{-2}$  are. This suggests that for these sources, the submillimeter emission is related to the AGN activity, or, perhaps more simply, to the obscuration level.

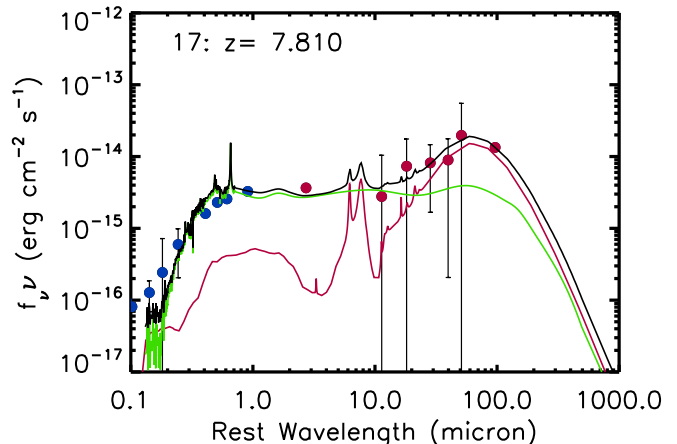


**Figure 35.** Fit to the SED of source 17 or ALMA033235-275215. The blue circles show the data on which the photz is based, and the red circles the data on which the FIRz is based. The fit is for the FIRz and shows that a combination of a type 2 quasar (green curve) and a star former (red curve) can provide a good fit to all the observations (black curve) at this redshift.

In order for the sources (sources 17 and 19) not to be Compton thick, we would have to reduce their redshifts to  $z < 2.5$ . This is extremely difficult to do, given that, in each case, the ALMA flux is brighter than the shorter wavelength *Herschel* fluxes. Including an AGN contribution, which contributes preferentially to rest-frame wavelengths shortward of  $100 \mu\text{m}$ , will only make this worse.

In Figure 35, we show a fit to source 17 with contributions from a type 2 quasar and a star former at longer wavelengths. This provides a good description of the SED for the high FIRz. We conclude that both sources 17 and 19 may be high-redshift Compton thick sources, similar to the high-redshift Compton thick source of Gilli et al. (2011). However, the fits depend on the assumed temperatures and the template, making them substantially uncertain. Millimeter spectroscopic measurements of the redshifts will ultimately determine whether these sources are indeed Compton thick AGN.

## 9. SUMMARY

In this third paper in the SUPER GOODS series on powerfully star-forming galaxies in the two GOODS fields, we analyzed the  $> 4\sigma$  sources in the most sensitive  $100 \text{ arcmin}^2$  area ( $\text{rms} < 0.56 \text{ mJy}$ ) of a deep SCUBA-2 survey of the GOODS-S and presented the 75 band 7 ALMA sources ( $> 4.5\sigma$ ) obtained from high-resolution interferometric follow-up observations. Based on the noise level of the SCUBA-2 image in the  $100 \text{ arcmin}^2$  area, we expect the SCUBA-2 sample to be complete to the  $4\sigma$  level of  $2.25 \text{ mJy}$ . Since the SCUBA-2—but

not ALMA—flux may be biased upwards due to Eddington bias and source blending, we also expect the ALMA sample to be complete to this level. The main results of our analysis are as follows:

- Only five of the 53 SCUBA-2 sources in the complete sample above 2.25 mJy have no ALMA counterparts, and only 13% (68% confidence range 7–19%) have multiple counterparts. Given the larger primary beam size of  $\sim 17''$  for ALMA in band 7 versus  $\sim 14''$  for SCUBA-2 at 850  $\mu\text{m}$ , ALMA should be able to image all the sources that contribute to the SCUBA-2 flux. Indeed, when we summed the individual ALMA fluxes in cases where there were multiple ALMA counterparts, we found that the ALMA and SCUBA-2 fluxes were consistent with one another. This also emphasizes that our best ALMA fluxes are not missing flux due to resolution issues (that is, we have not resolved out the flux), so they can be used to generate accurate ALMA number counts.
- The ALMA sources have diverse optical/NIR counterparts ranging from bright, low-redshift galaxies to sources which remain undetected even in extremely deep optical/NIR images. The latter sources are the most plausible candidates for very high-redshift SMGs.
- Using known spectroscopic and photometric redshifts from the literature, we confirmed the known correlation of redshift with  $K_s$  magnitude for the ALMA sources. Thus, as previously noted (e.g., Barger et al. 2014; Simpson et al. 2014),  $K_s$  magnitude can be used as a crude redshift estimator.
- We compared and tested the KIEROS (Wang et al. 2012), HIEROS (Wang et al. 2016), and three color (Chen et al. 2016) techniques for selecting high-redshift dusty galaxies. Although all of the methods are very comparable in their ability to select SMGs, their detection rates are only at the 40 – 55% level and depend strongly on the photometry methods employed.
- Consistent with Barger et al. (2012, 2014) and Paper I, we found that an Arp 220 template provides a good representation of the multiwavelength SEDs of the ALMA sources, so we used it to estimate FIR photometric redshifts. While there is some scatter, the overall correlation of these redshifts with the spectroscopic and photometric redshifts is reasonable for most of the sources.
- We also compared the 4.5  $\mu\text{m}$  and 24  $\mu\text{m}$  to 850  $\mu\text{m}$  flux ratios to the redshifts. We found a tight correlation, with both ratios showing the expected decline with redshift, and the highest redshift sources being faint at both 4.5  $\mu\text{m}$  and 24  $\mu\text{m}$ . These flux

ratios can therefore be used to find high-redshift ( $z \gtrsim 4$ ) candidates, even in the absence of full long-wavelength SEDs.

- For the ALMA sources above 1.65 mJy (the flux limit above which we had high S/N throughout the SEDs and hence could estimate FIR photometric redshifts), the median redshift is  $z = 2.74$ , and for those above 3 mJy, the median redshift is  $z = 3.26$ . However, these rely on mostly estimated redshifts, which may be problematic if there is AGN activity or if sources lie at high redshift. Based on both the FIR and standard photometric redshifts, we found a total of seven candidate  $z \gtrsim 4$  sources.
- Consistent with Paper I, we found that the redshift distribution of the ALMA sources increases with increasing 850  $\mu\text{m}$  flux, and the contribution of dusty, powerfully star-forming galaxies observed here by SCUBA-2 and ALMA to the overall star formation history is impressively large (of order 30%).
- All but 11 of the 74 ALMA sources (excluding the one source that is not on the *HST* GOODS-S area) are detected in the F160W band, the longest wavelength at which we can make high spatial resolution imaging. Unlike previous work (Hodge et al. 2013; Chen et al. (2016)), we see little dependence of the F160W undetected fraction on submillimeter flux. We made visual morphological classifications using the F160W data of the 52 sources that were bright enough to do so. We found that 24 showed clear evidence of merging for a merger rate of at least (since some of the unclassified sources may also be mergers) 44% (68% confidence range 35–53%).
- We found that just over half (41) of the total ALMA sample are detected in the Luo et al. (2017) X-ray catalog of the 7 Ms CDF-S. The fraction of X-ray detected sources is much higher at higher submillimeter fluxes: 86% (68% confidence range 67–95%) above 4 mJy versus 48% (68% confidence range 38–57%) below 4 mJy. Without such deep data, many, if not most, X-ray detections of ALMA sources would be missed (e.g., the 2 Ms data in the CDF-N).
- We computed the rest-frame 2 – 8 keV luminosities,  $L_{2-8 \text{ keV}}$ , from the observed 0.5 – 2 keV fluxes and the rest-frame 8 – 28 keV luminosities,  $L_{8-28 \text{ keV}}$ , from the shallower observed 2 – 7 keV fluxes for the ALMA sources. Since X-ray binaries produced during star formation should have soft X-ray photon indices, we first considered only the sources detected in the soft band (39), or, if detected in both bands, then having a photon index  $\Gamma > 1.2$  (5). Combining the Mineo et al.

(2014) SFR versus X-ray luminosity relation with the Barger et al. (2014) SFR versus 850  $\mu\text{m}$  flux relation, we obtained  $L_{2-8 \text{ keV}} = 3 \times 10^{41} f_{850}(\text{mJy}) \text{ erg s}^{-1}$ . We found that nearly all of the  $z > 1.5$  sources are consistent with this star formation relation. This suggests that the 7 Ms image is deep enough to start to probe the star formation taking place in the most intensely star-forming galaxies in the universe.

- The  $L_{8-28 \text{ keV}}$  for 20 of the 24 hard band detections (the other four were consistent with the star formation relation discussed in the previous bullet) are all well above the luminosity that could be accounted for by star formation. Most are moderate luminosity AGNs that lie just above the detection threshold. They have substantial obscuration ( $\log N_H = 23 - 24 \text{ cm}^{-2}$ ) but are not Compton thick.
- Two of our high-redshift candidates could be Compton thick, similar to the high-redshift Compton thick source found by Gilli et al. (2011). The only way for these two sources not to be Compton thick would be if their redshifts were  $z < 2.5$ . However, their ALMA fluxes are considerably brighter than the shorter wavelength *Herschel* fluxes, making such redshifts difficult to achieve.

We gratefully acknowledge support from NASA grant NNX17AF45G (L. L. C.), NSF grants AST-1313309 (L. L. C.) and AST-1313150 (A. J. B.), CONICYT grants Basal-CATA PFB-06/2007 (F. E. B, J. G.-L.), FONDECYT Regular 1141218 (F. E. B, J. G.-L.) and Programa de Astronomia FONDO ALMA 2016

31160033 (JG-L), and the Ministry of Economy, Development, and Tourism's Millennium Science Initiative through grant IC120009, awarded to The Millennium Institute of Astrophysics, MAS (F. E. B.). A. J. B. acknowledges additional support from the John Simon Memorial Guggenheim Foundation, the Trustees of the William F. Vilas Estate, and the University of Wisconsin-Madison Office of the Vice Chancellor for Research and Graduate Education with funding from the Wisconsin Alumni Research Foundation. ALMA is a partnership of ESO (representing its member states), NSF (USA) and NINS (Japan), together with NRC (Canada), MOST and ASIAA (Taiwan), and KASI (Republic of Korea), in cooperation with the Republic of Chile. The Joint ALMA Observatory is operated by ESO, AUI/NRAO and NAOJ. The James Clerk Maxwell Telescope is operated by the East Asian Observatory on behalf of The National Astronomical Observatory of Japan, Academia Sinica Institute of Astronomy and Astrophysics, the Korea Astronomy and Space Science Institute, the National Astronomical Observatories of China and the Chinese Academy of Sciences (Grant No. XDB09000000), with additional funding support from the Science and Technology Facilities Council of the United Kingdom and participating universities in the United Kingdom and Canada. The W. M. Keck Observatory is operated as a scientific partnership among the California Institute of Technology, the University of California, and NASA, and was made possible by the generous financial support of the W. M. Keck Foundation. The authors wish to recognize and acknowledge the very significant cultural role and reverence that the summit of Mauna Kea has always had within the indigenous Hawaiian community. We are most fortunate to have the opportunity to conduct observations from this mountain.

## REFERENCES

- Aravena, M., Decarli, R., Walter, F., et al. 2016, *ApJ*, 833, 68  
 Ashby, M. L. N., Willner, S. P., Fazio, G. G., et al. 2015, *ApJS*, 218, 33  
 Balestra, I., Mainieri, V., Popesso, P., et al. 2010, *A&A*, 512, 12  
 Barger, A. J., Cowie, L. L., Chen, C.-C., et al. 2014, *ApJ*, 784, 9  
 Barger, A. J., Cowie, L. L., Owen, F. N., Hsu, L.-Y., & Wang, W.-H. 2017, *ApJ*, 835, 95 (Paper II)  
 Barger, A. J., Cowie, L. L., & Richards, E. A. 2000, *AJ*, 119, 2092  
 Barger, A. J., Cowie, L. L., Sanders, D. B., et al. 1998, *Nature*, 394, 248  
 Barger, A. J., Wang, W.-H., Cowie, L. L., et al. 2012, *ApJ*, 761, 89  
 Beckwith, S. V. W., Stiavelli, M., Koekemoer, A. M., et al. 2006, *AJ*, 132, 1729  
 Brammer, G. B., van Dokkum, P. G., & Coppi, P. 2008, *ApJ*, 686, 1503  
 Brammer, G. B., van Dokkum, P. G., Franx, M., et al. 2012, *ApJS*, 200, 13  
 Cardamone, C. N., van Dokkum, P. G., Urry, C. M., et al. 2010, *ApJS*, 189, 270  
 Casey, C. M., Berta, S., Béthermin, M., et al. 2012, *ApJ*, 761, 140  
 Casey, C. M., Chen, C.-C., Cowie, L. L., et al. 2013, *MNRAS*, 436, 1919  
 Casey, C. M., Narayanan, D., & Cooray, A., 2014, *PhR*, 541, 45  
 Chapman, S. C., Barger, A. J., Cowie, L. L., et al. 2003, 585, 57  
 Chapman, S. C., Blain, A. W., Smail, I., & Ivison, R. J. 2005, *ApJ*, 622, 772  
 Chen, C.-C., Cowie, L. L., Barger, A. J., et al. 2013, *ApJ*, 776, 131  
 Chen, C.-C., Smail, I., Swinbank, A. M., et al. 2015, *ApJ*, 799, 194  
 Chen, C.-C., Smail, I., Swinbank, A. M., et al. 2016, *ApJ*, 831, 91  
 Cooper, M. C., Yan, R., Dickinson, M., et al. 2012, *MNRAS*, 425, 2116  
 Cowie, L. L., Barger, A. J., Hsu, L.-Y., et al. 2017, *ApJ*, 837, 139 (Paper I)  
 Cowie, L. L., Hu, E. M., & Songaila, A. 1995, *AJ*, 110, 1576  
 da Cunha, E., Walter, F., Smail, I. R., et al. 2015, *ApJ*, 806, 110  
 Dahlen, T., Mobasher, B., Faber, S. M., et al. 2013, *ApJ*, 775, 93  
 Danielson, A. L. R., Swinbank, A. M., Smail, I., et al. 2017, *ApJ*, 840, 78  
 Dunlop, J. S., McLure, R. J., Biggs, A. D., et al. 2017, *MNRAS*, 466, 861  
 Eales, S., Lilly, S., Gear, W., et al. 1999, *ApJ*, 515, 518  
 Elbaz, D., Dickinson, M., Hwang, H. S., et al. 2011, *A&A*, 533, A119  
 Fontana, A., Dunlop, J. S., Paris, D., et al. 2014, *A&A*, 570, A11

- Franco, M., Elbaz, D., Bethermin, M., et al. 2018, arXiv:1803.00157 (F18)
- Giavalisco, M., Dickinson, M., Ferguson, H. C., et al. 2004, *ApJ*, 600, L93
- Grogin, N. A., Kocevski, D. D., Faber, S. M., et al. 2011, *ApJS*, 197, 35
- Guo, Y., Ferguson, H. C., Giavalisco, M., et al. 2013, *ApJS*, 207, 24 (G13)
- Hatsukade, B., Kohno, K., Umehata, H., et al. 2016, *PASJ*, 68, 36
- Hildebrandt, H., Erben, T., Dietrich, J. P., et al. 2006, *A&A*, 452, 1121
- Hill, R., Chapman, S. C., Scott, D., et al. 2018, *MNRAS*, 477, 2042
- Ho, P. T. P., Moran, J. M., & Lo, K. Y. 2004, *ApJ*, 616, L1
- Hodge, J. A., Karim, A., Smail, I., et al. 2013, *ApJ*, 768, 91
- Holland, W. S., Bintley, D., Chapin, E. L., et al. 2013, *MNRAS*, 430, 2513
- Holland, W. S., Robson, E. I., Gear, W. K., et al. 1999, *MNRAS*, 303, 659
- Hsieh, B.-C., Wang, W.-H., Hsieh, C.-C., et al. 2012, *ApJS*, 203, 23
- Hsu, L.-T., Salvato, M., Nandra, K., et al. 2014, *ApJ*, 796, 60
- Hsu, L.-Y., Cowie, L. L., Chen, C.-C., Barger, A. J., & Wang, W.-H. 2016, *ApJ*, 829, 25
- Hughes, D. H., Serjeant, S., Dunlop, J., et al. 1998, *Nature*, 394, 241
- Illingworth, G., Magee, D., Bouwens, R., et al. 2016, arXiv:1606.00841
- Inami, H., Bacon, R., Brinchmann, J., et al. 2017, *A&A*, 608, A2
- Ivson, R. J., Greve, T. R., Smail, I., et al. 2002, *MNRAS*, 337, 1
- Karim, A., Swinbank, M., Hodge, J., et al. 2013, *MNRAS*, 432, 2
- Koekemoer, A. M., Ellis, R. S., McLure, R. J., et al. 2013, *ApJS*, 209, 3
- Koekemoer, A. M., Faber, S. M., Ferguson, H. C., et al. 2011, *ApJS*, 197, 36
- Kriek, M., Shapley, A. E., Reddy, N. A., et al. 2015, *ApJ*, 218, 15
- Kroupa, P. 2001, *MNRAS*, 322, 231
- Kurk, J., Cimatti, A., Daddi, E., et al. 2013, *A&A*, 549, A63
- Laporte, N., Bauer, F. E., Troncoso-Iribarren, P., et al. 2017, *A&A*, 604, A132
- Larson, D., Dunkley, J., Hinshaw, G., et al. 2011, *ApJS*, 192, 16
- Le Fèvre, O., Vettolani, G., Garilli, B., et al. 2005, *A&A*, 439, 845
- Luo, B., Brandt, W. N., Xue, Y. Q., et al. 2017, *ApJS*, 228, 2
- Madau, P., & Dickinson, M. 2014, *ARA&A*, 52, 415
- Magnelli, B., Elbaz, D., Chary, R. R., Dickinson, M., Le Borgne, D., Frayer, D. T., & Willmer, C. N. A. 2011, *A&A*, 528, A35
- Magnelli, B., Popesso, P., Berta, S., et al. 2013, *A&A*, 553, 132
- Miettinen, O., Novak, M., Smolčić, V., et al. 2015, *A&A*, 584, 32
- Mignoli, M., Cimatti, A., Zamorani, G., et al. 2005, *A&A*, 437, 883
- Mineo, S., Gilfanov, M., Lehner, B. D., Morrison, G. E., & Sunyaev, R. 2014, *MNRAS*, 437, 1698
- Momcheva, I. G., Brammer, G. V., van Dokkum, P. G., et al. 2016, *ApJS*, 225, 27
- Mullaney, J. R., Alexander, D. M., Aird, J., et al. 2015, *MNRAS*, 453, L83
- Nonino, M., Dickinson, M., Rosati, P., et al. 2009, *ApJS*, 183, 244
- Oesch, P., Montes, M., & HDUV Survey Team 2015, IAU General Assembly #29, id.2252813
- Oliver, S. J., Bock, J., Altieri, B., et al. 2012, *MNRAS*, 424, 1614
- Owen, F. N. 2018, *ApJS*, 235, 34
- Popesso, P., Dickinson, M., Nonino, M., et al. 2009, *A&A*, 494, 443
- Rafferty, D. A., Brandt, W. N., Alexander, D. M., et al. 2011, *ApJ*, 742, 3
- Reddy, N. A., & Steidel, C. C. 2009, *ApJ*, 692, 778
- Retzlaff, J., Rosati, P., Dickinson, M., et al. 2010, *A&A*, 511, A50
- Salpeter, E. E. 1955, *ApJ*, 121, 161
- Santini, P., Ferguson, H. C., Fontana, A., et al. 2015, *ApJ*, 801, 97
- Santini, P., Fontana, A., Grazian, A., et al. 2009, *A&A*, 504, 751
- Sazonov, S. & Khabibullin, I. 2017, *MNRAS*, 468, 2249
- Schreiber, C., Elbaz, D., Pannella, M., et al. 2018, *A&A*, 609, A30
- Schreiber, C., Pannella, M., Leiton, R., et al. 2017, *A&A*, 599, A134
- Scott, K. S., Yun, M. S., Wilson, G. W., et al. 2010, *MNRAS*, 405, 2260
- Scoville, N., Sheth, K., Aussel, H., et al. 2016, *ApJ*, 820, 83
- Serjeant, S., et al. 2003, *MNRAS*, 344, 887
- Shu, X. W., Elbaz, D., Bourne, N., et al. 2016, *ApJS*, 222, 4
- Silva, L., Granato, G. L., Bressan, A., & Danese, L. 1998, *ApJ*, 509, 103
- Silverman, J. D., Mainieri, V., Salvato, M., et al. 2010, *ApJS*, 191, 124
- Simpson, J. M., Smail, I., Swinbank, A. M., et al. 2015, *ApJ*, 799, 81
- Simpson, J. M., Swinbank, A. M., Smail, I., et al. 2014, *ApJ*, 788, 125
- Siringo, G., Kreysa, E., Kovács, A., et al. 2009, *A&A*, 497, 945
- Skelton, R., Whitaker, K. E., Momcheva, I. G., et al. 2014, *ApJS*, 214, 24
- Smail, I., Ivson, R. J., Blain, A. W. 1997, *ApJL*, 490, L5
- Smolčić, V., Aravena, M., Navarrete, F., et al. 2012, *A&A*, 548, 4
- Straatman, C. M. S., Spitler, L. R., Quadri, R. F., et al. 2016, *ApJ*, 830, 51 (S16)
- Suh, H., Hasinger, G., Steinhardt, C., Silverman, J. D., & Schramm, M. 2015, *ApJ*, 815, 129
- Swinbank, A. M., Simpson, J. M., Smail, I., et al. 2014, *MNRAS*, 438, 1267
- Swinbank, A. M., Smail, I., Chapman, S. C., et al. 2010, *MNRAS*, 405, 234
- Szokoly, G. P., Bergeron, J., Hasinger, G., et al. 2004, *ApJS*, 155, 271
- Targett, T. A., Dunlop, J. S., Cirasuolo, M., et al. 2013, *MNRAS*, 432, 2012
- Teplitz, H. I., Rafelski, M., Kurczynski, P., et al. 2013, *AJ*, 146, 159
- Treister, E., Virani, S., Gawiser, E., et al. 2009, *ApJ*, 693, 1713
- Ueda, Y., Hatsukade, B., Kohno, K., et al. 2017, *ApJ*, in press (arXiv:1712.03350)
- van der Burg, R. F. J., Hildebrandt, H., & Erben, T. 2010, *A&A*, 523, A74
- Wang, T., Elbaz, D., Schreiber, C., et al. 2016, *ApJ*, 816, 84
- Wang, W.-H., Barger, A. J., & Cowie, L. L. 2012, *ApJ*, 744, 155
- Wang, W.-H., Cowie, L. L., Barger, A. J., & Williams, J. P. 2011, *ApJ*, 726, L18
- Wardlow, J. L., Smail, I., Coppin, K. E. K., et al. 2011, *MNRAS*, 415, 1479
- Weiß, A., Kovács, A., Coppin, K., et al. 2009, *ApJ*, 707, 1201
- Windhorst, R. A., Cohen, S. H., Hathi, N. P., et al. 2011, *ApJS*, 193, 27
- Xue, Y. Q., Luo, B., Brandt, W. N., et al. 2011, *ApJS*, 195, 10
- Xue, Y. Q., Luo, B., Brandt, W. N., et al. 2016, *ApJS*, 224, 15

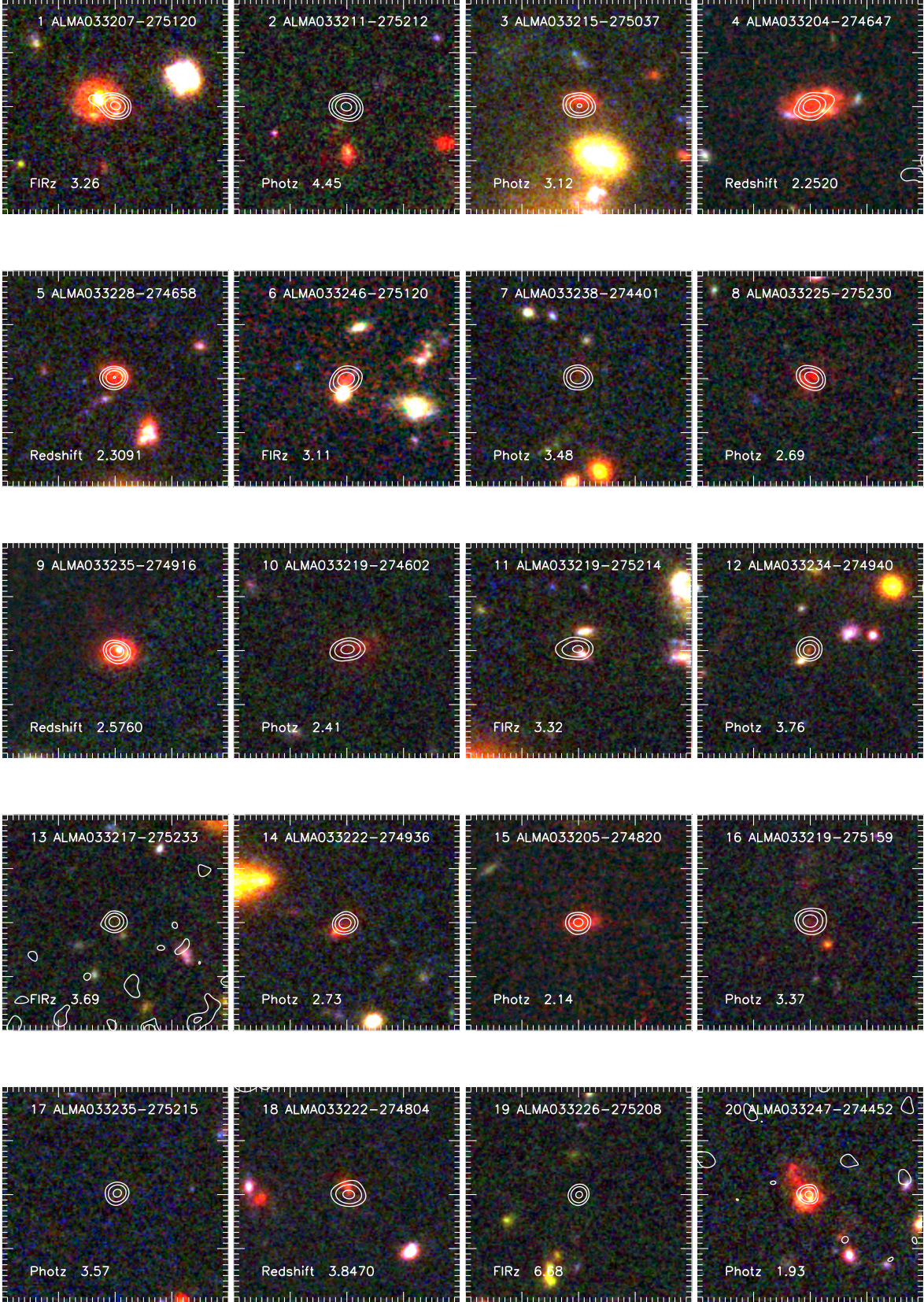


**Figure 10.** Three color *HST* images (blue = F450W, green = F814W, and red = F160W) for the ALMA sources in Table 4. The thumbnails are  $8''$  on a side, or roughly 70 kpc at  $z = 2$ . The ALMA continuum emission is shown with white contours using the  $0''.5$  FWHM tapered images contoured at 0.6, 1.2, 2.4 and 4.8 mJy/beam. The numbers refer to Table 4, and the redshifts are marked as spectroscopic (Redshift), standard photometric (Photz), or FIR photometric (FIRz). Sources with none of these are marked with “Photz ?”. The redshift given was chosen in the order of first specz, then  $Q < 3$  photz from S16, and finally FIRz when there was no available specz or photz.

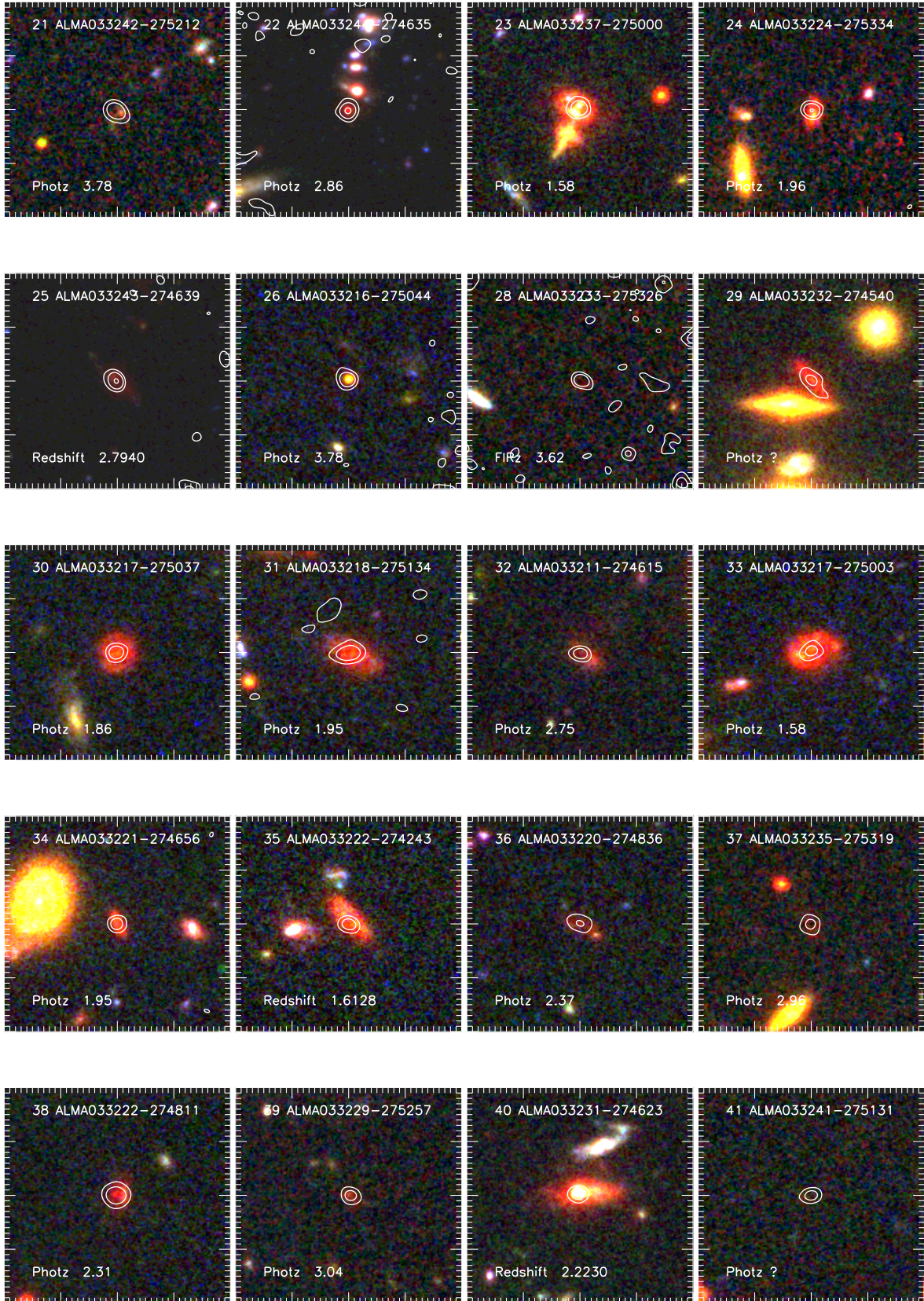


Figure 10. Continued



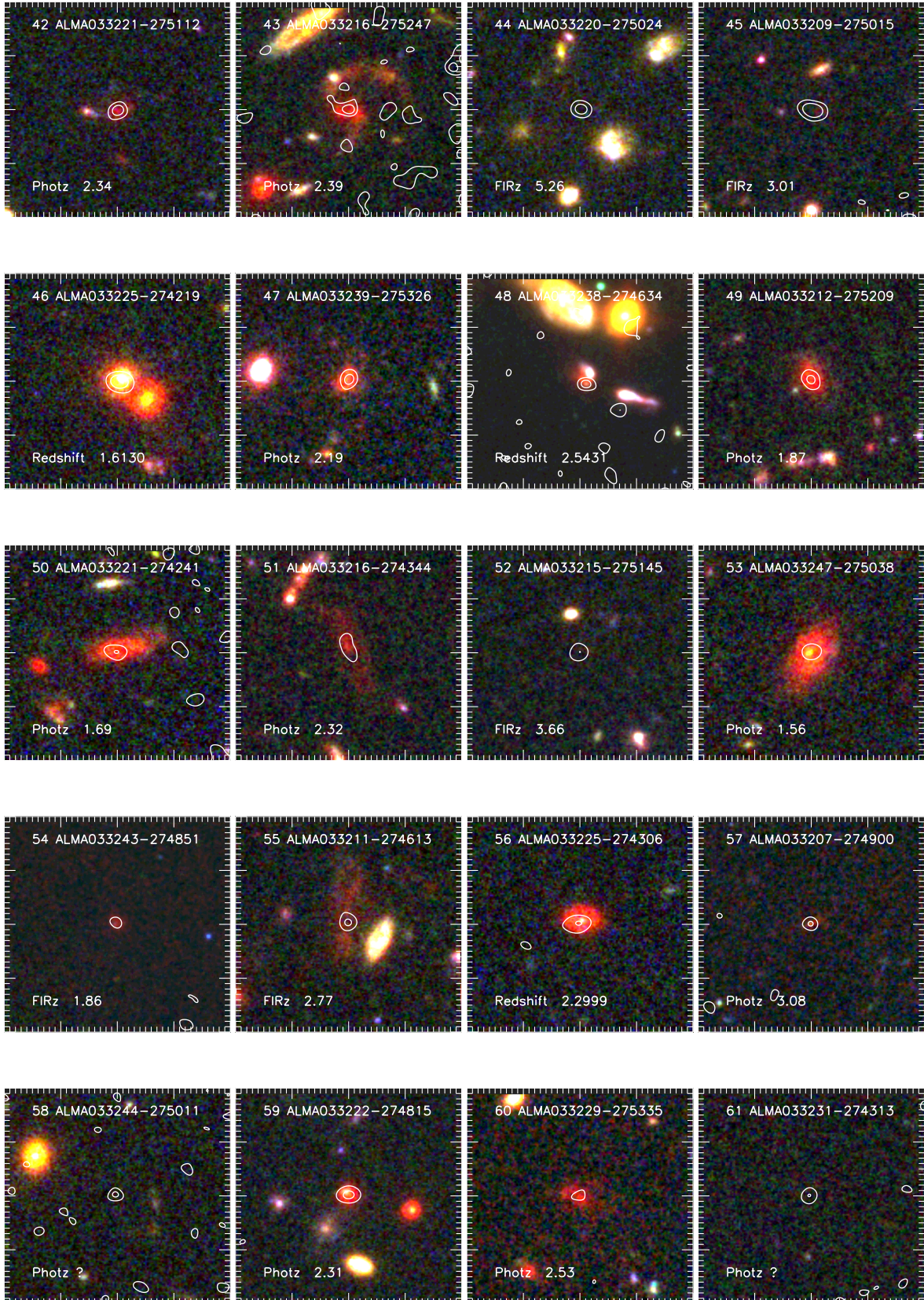


Figure 10. Continued

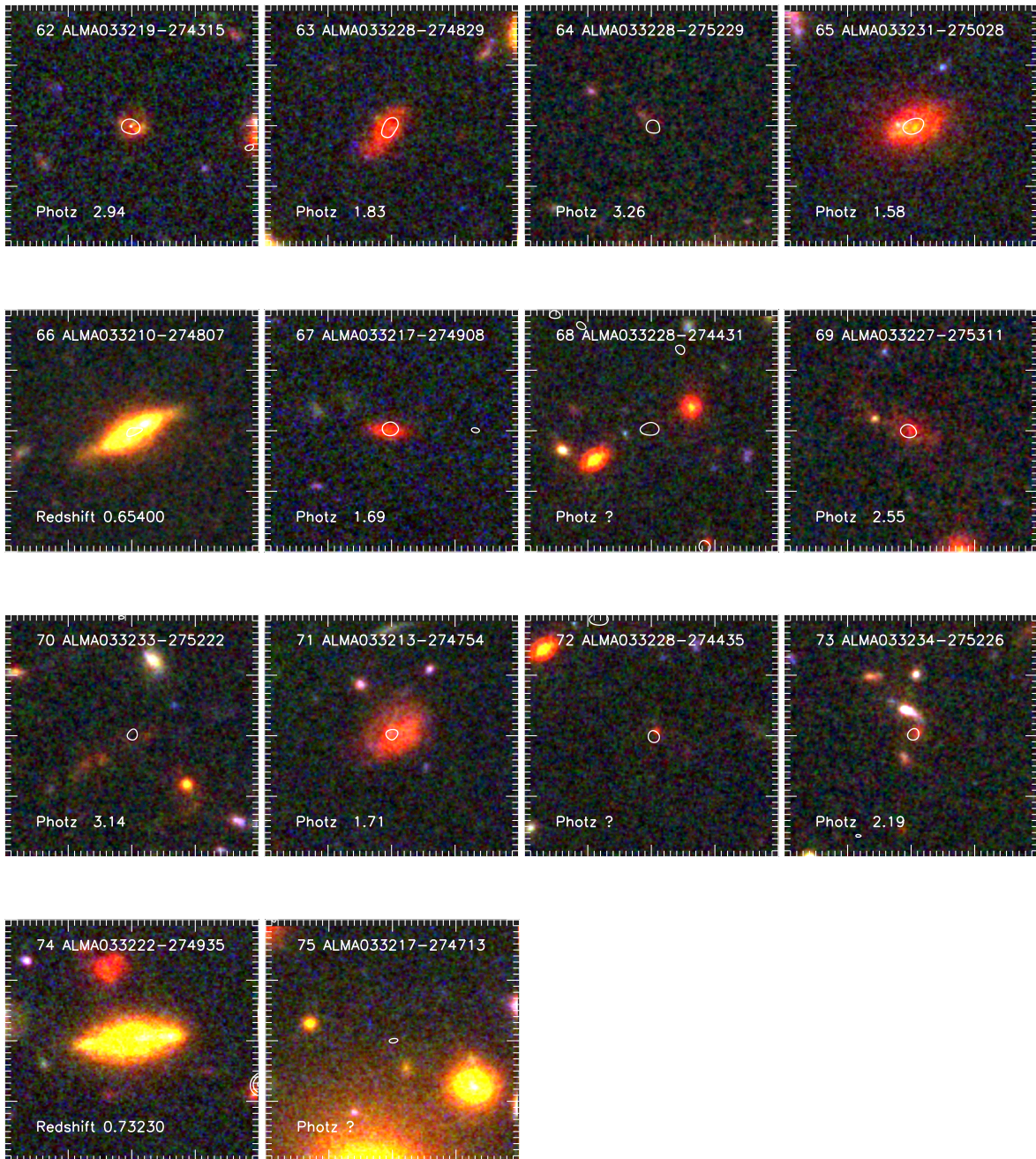


Figure 10. Continued

**Table 2.** Central CDF-S 850  $\mu\text{m}$  Sample (rms < 0.56 mJy, flux > 2.25 mJy)

No.	Name	R.A.	Decl.	Flux	Error	R.A. (ALMA)	Decl.	offset	Flux (ALMA)
(1)	(2)	J2000.0	J2000.0	(mJy)	(mJy)	J2000.0	J2000.0	(arcsec)	(mJy)
(1)	(2)	(3)	(4)	(5)	(6)	(7)	(8)	(9)	(10)
1	SMM033211-275210	3 32 11.47	-27 52 10.8	10.10	0.45	3 32 11.33	-27 52 12.0	2.2	8.8
2	SMM033207-275120	3 32 7.490	-27 51 20.8	9.25	0.47	3 32 7.289	-27 51 20.8	2.6	8.9
3	SMM033205-274648	3 32 5.019	-27 46 48.8	7.51	0.47	3 32 4.889	-27 46 47.7	2.0	6.4
4	SMM033246-275119	3 32 46.85	-27 51 19.9	6.76	0.53	3 32 46.83	-27 51 20.8	1.0	5.9
5	SMM033222-274808	3 32 22.41	-27 48 8.99	6.04	0.31	3 32 22.16	-27 48 11.6	4.3	2.2
5	...	...	...	6.04	0.31	3 32 22.28	-27 48 4.79	4.5	3.6
6	SMM033219-275214	3 32 19.24	-27 52 14.0	5.93	0.41	3 32 19.05	-27 52 14.9	2.7	4.7
7	SMM033215-275038	3 32 15.33	-27 50 38.0	5.58	0.38	3 32 15.33	-27 50 37.6	0.4	6.6
8	SMM033222-274936	3 32 22.41	-27 49 36.9	5.41	0.33	3 32 22.47	-27 49 35.2	1.9	0.93
8	...	...	...	5.41	0.33	3 32 22.16	-27 49 36.6	3.4	4.6
9	SMM033225-275231	3 32 25.36	-27 52 31.0	5.18	0.42	3 32 25.25	-27 52 30.7	1.3	5.1
10	SMM033243-274639	3 32 43.82	-27 46 39.9	5.11	0.46	3 32 43.53	-27 46 39.2	3.9	3.1
10	...	...	...	5.11	0.46	3 32 44.03	-27 46 35.8	4.8	3.3
11	SMM033234-274941	3 32 34.48	-27 49 41.0	4.86	0.38	3 32 34.27	-27 49 40.3	2.8	4.7
12	SMM033235-274914	3 32 35.83	-27 49 14.9	4.84	0.38	3 32 35.73	-27 49 16.2	1.8	5.0
13	SMM033243-275212	3 32 43.00	-27 52 12.8	4.69	0.51	3 32 42.80	-27 52 12.7	2.7	3.5
14	SMM033228-274658	3 32 28.60	-27 46 58.0	4.50	0.34	3 32 28.50	-27 46 58.3	1.2	6.3
15	SMM033216-274344	3 32 16.39	-27 43 44.0	4.17	0.48	3 32 16.27	-27 43 44.0	1.5	1.9
16	SMM033211-274614	3 32 11.80	-27 46 14.8	4.10	0.42	3 32 11.94	-27 46 15.4	1.9	2.5
16	...	...	...	4.10	0.42	3 32 11.61	-27 46 13.1	3.0	1.7
17	SMM033217-275039	3 32 17.22	-27 50 39.9	3.85	0.38	3 32 17.21	-27 50 37.2	2.7	2.7
18	SMM033226-275206	3 32 26.27	-27 52 6.99	3.84	0.42	3 32 26.11	-27 52 8.50	2.5	3.6
19	SMM033218-275228	3 32 18.12	-27 52 28.9	3.68	0.42	3 32 17.96	-27 52 33.2	4.7	4.6
20	SMM033238-274401	3 32 38.08	-27 44 1.00	3.65	0.48	3 32 38.00	-27 44 1.00	1.0	5.6
21	SMM033219-274604	3 32 19.79	-27 46 4.00	3.62	0.39	3 32 19.70	-27 46 2.20	2.1	4.9
22	SMM033237-275000	3 32 37.87	-27 50 0.99	3.49	0.40	3 32 37.72	-27 50 0.59	2.0	3.3
23	SMM033247-275038	3 32 47.90	-27 50 38.9	3.48	0.52	3 32 47.73	-27 50 38.2	2.3	1.8
24	SMM033230-275334	3 32 30.11	-27 53 34.9	3.42	0.47	3 32 29.90	-27 53 35.8	2.9	1.6
25	SMM033217-275002	3 32 17.60	-27 50 2.00	3.42	0.37	3 32 17.45	-27 50 3.40	2.4	2.4
26	SMM033221-275024	3 32 21.13	-27 50 24.0	3.38	0.37	3 32 20.91	-27 50 24.7	2.9	2.2
27	SMM033224-275334	3 32 24.91	-27 53 34.9	3.31	0.46	3 32 24.66	-27 53 34.2	3.2	3.2
28	SMM033216-275247	3 32 16.69	-27 52 47.0	3.30	0.44	3 32 16.52	-27 52 47.0	2.1	2.2
29	SMM033227-275312	3 32 27.24	-27 53 12.0	3.29	0.44	3 32 27.15	-27 53 11.8	1.3	1.2
30	SMM033205-274819	3 32 5.990	-27 48 19.8	3.23	0.45	3 32 5.830	-27 48 20.5	2.2	3.9

*Table 2 continued*

Table 2 (continued)

No.	Name	R.A.	Decl.	Flux	Error	R.A. (ALMA)	Decl.	offset	Flux (ALMA)
(1)	(2)	J2000.0	J2000.0	(mJy)	(mJy)	J2000.0	J2000.0	(arcsec)	(mJy)
		(3)	(4)	(5)	(6)	(7)	(8)	(9)	(10)
31	SMM033234-275225	3 32 34.11	-27 52 25.0	3.19	0.43	3 32 34.28	-27 52 26.7	2.9	1.0
31	...	...	...	3.19	0.43	3 32 33.90	-27 52 22.2	3.8	1.1
32	SMM033212-275209	3 32 12.91	-27 52 9.89	3.17	0.44	3 32 12.88	-27 52 9.40	0.71	1.9
33	SMM033219-275201	3 32 19.92	-27 52 1.00	3.08	0.41	3 32 19.86	-27 51 59.7	1.5	3.9
34	SMM033203-275039	3 32 3.349	-27 50 39.8	3.02	0.52	3 32 3.500	-27 50 39.8	1.9	3.0
35	SMM033219-274314	3 32 19.33	-27 43 14.9	2.98	0.49	3 32 19.36	-27 43 15.1	0.29	1.5
36	SMM033233-274544	3 32 33.04	-27 45 44.0	2.80	0.42	3 32 32.91	-27 45 40.9	3.5	2.8
37	SMM033231-274624	3 32 31.32	-27 46 24.9	2.78	0.40	3 32 31.46	-27 46 23.5	2.4	2.2
38	SMM033229-274433	3 32 29.04	-27 44 33.0	2.76	0.47	3 32 28.91	-27 44 31.4	2.3	1.3
38	...	...	...	2.76	0.47	3 32 28.78	-27 44 35.2	4.1	1.1
39	SMM033235-275318	3 32 35.24	-27 53 18.9	2.71	0.49	3 32 35.13	-27 53 19.7	1.6	2.3
40	SMM033229-275258	3 32 29.96	-27 52 58.0	2.68	0.44	3 32 29.83	-27 52 57.7	1.6	2.2
41	SMM033221-274244	3 32 21.90	-27 42 44.0	2.68	0.52	3 32 22.01	-27 42 43.7	1.5	2.4
42	SMM033235-275217	3 32 35.32	-27 52 17.0	2.64	0.43	3 32 35.19	-27 52 15.7	2.1	3.8
43	SMM033241-275133	3 32 41.71	-27 51 33.0	2.57	0.45	3 32 41.47	-27 51 31.8	3.3	2.2
44	SMM033215-274629	3 32 15.27	-27 46 29.0	2.55	0.40	...	...	...	[ 0.12]
45	SMM033231-275027	3 32 31.69	-27 50 27.0	2.54	0.39	3 32 31.55	-27 50 28.9	2.7	1.4
46	SMM033229-274301	3 32 29.57	-27 43 1.99	2.49	0.49	...	...	...	[ 0.22]
47	SMM033233-275326	3 32 33.58	-27 53 26.9	2.45	0.49	3 32 33.42	-27 53 26.6	2.0	2.8
48	SMM033225-274306	3 32 25.88	-27 43 6.00	2.38	0.48	3 32 25.69	-27 43 6.00	2.6	1.7
49	SMM033204-275007	3 32 4.629	-27 50 7.89	2.32	0.47	...	...	...	[ 0.10]
50	SMM033215-274514	3 32 15.80	-27 45 14.0	2.32	0.41	...	...	...	[ 0.12]
51	SMM033238-274634	3 32 38.61	-27 46 34.9	2.32	0.42	3 32 38.55	-27 46 34.5	0.94	2.0
52	SMM033218-275131	3 32 18.72	-27 51 31.9	2.29	0.40	3 32 18.57	-27 51 34.6	3.3	2.7
53	SMM033208-274646	3 32 8.789	-27 46 46.8	2.25	0.45	...	...	...	[ 0.37]

NOTE—The columns are (1) the SCUBA-2 source number, (2) the SCUBA-2 source name, (3 and 4) the SCUBA-2 R.A. and Decl., (5 and 6) the flux and error measured from the SCUBA-2 matched-filter image, (7 and 8) the R.A. and Decl. of the corresponding ALMA source(s), (9) the offset between the SCUBA-2 and ALMA source positions, and (10) the ALMA 850  $\mu\text{m}$  flux. In Column (10), for the 5 cases where the ALMA observations yielded no ALMA detections, we list the central  $1\sigma$  noise of the ALMA image (enclosed in square brackets) instead of an ALMA flux detection.

**Table 4.** CDF-S Band 7 ALMA  $> 4.5\sigma$

No.	Name	R.A.	Decl.	Pk Flux	Error	S/N	Flux	Error	1.13 mm	SCUBA-2	offset
(1)	(2)	J2000.0	J2000.0	(mJy)	(mJy)	(7)	(mJy)	(mJy)	(mJy)	No.	(arcsec)
		(3)	(4)	(5)	(6)		(8)	(9)	(10)	(11)	(12)
1	ALMA033207-275120	3 32 7.289	-27 51 20.8	5.97	0.14	42.1	8.93 H	0.21	...	2	2.6
2	ALMA033211-275212	3 32 11.33	-27 52 12.0	6.00	0.12	47.2	8.83 H	0.26	...	1	2.2
3	ALMA033215-275037	3 32 15.33	-27 50 37.6	5.02	0.12	41.1	6.61	0.16	2.1	7	0.39
4	ALMA033204-274647	3 32 4.889	-27 46 47.7	4.39	0.15	28.1	6.45 B	0.41	1.9	3	2.0
5	ALMA033228-274658	3 32 28.50	-27 46 58.3	4.86	0.12	38.2	6.39	0.16	1.9	14	1.2
6	ALMA033246-275120	3 32 46.83	-27 51 20.8	4.10	.084	48.7	5.90 S	0.18	...	4	1.0
7	ALMA033238-274401	3 32 38.00	-27 44 1.00	4.25	0.10	39.7	5.60	0.14	1.4	20	1.0
8	ALMA033225-275230	3 32 25.25	-27 52 30.7	3.45	0.10	32.5	5.18 H	0.22	...	9	1.3
9	ALMA033235-274916	3 32 35.73	-27 49 16.2	3.86	.096	39.9	5.09	0.12	2.1	12	1.8
10	ALMA033219-274602	3 32 19.70	-27 46 2.20	3.15	0.14	21.8	4.90	0.29	1.0	21	2.1
11	ALMA033219-275214	3 32 19.05	-27 52 14.9	2.79	0.14	19.3	4.76 H	0.29	1.3	6	2.7
12	ALMA033234-274940	3 32 34.27	-27 49 40.3	3.59	0.12	28.0	4.73	0.16	1.6	11	2.8
13	ALMA033217-275233	3 32 17.96	-27 52 33.2	3.56	0.30	11.7	4.69	0.81	0.64	19	4.7
14	ALMA033222-274936	3 32 22.16	-27 49 36.6	3.52	0.13	25.9	4.64	0.17	1.1	8	3.4
15	ALMA033205-274820	3 32 5.830	-27 48 20.5	2.98	0.11	25.8	3.93	0.15	...	30	2.1
16	ALMA033219-275159	3 32 19.86	-27 51 59.7	3.52	0.11	31.7	3.91 M	0.13	1.2	33	1.5
17	ALMA033235-275215	3 32 35.19	-27 52 15.7	2.89	0.14	20.1	3.80	0.18	...	41	2.1
18	ALMA033222-274804	3 32 22.28	-27 48 4.79	2.87	0.12	22.8	3.64 M	0.13	1.3	5	4.5
19	ALMA033226-275208	3 32 26.11	-27 52 8.50	2.75	0.12	21.2	3.62	0.17	1.5	18	2.5
[20]	ALMA033247-274452	3 32 47.59	-27 44 52.3	2.88	0.24	11.7	3.61	0.30	...	...	...
21	ALMA033242-275212	3 32 42.80	-27 52 12.7	2.36	.098	24.0	3.55	0.20	...	13	2.7
22	ALMA033244-274635	3 32 44.03	-27 46 35.8	2.69	0.26	10.2	3.38	0.32	1.2	10	4.8
23	ALMA033237-275000	3 32 37.72	-27 50 0.59	2.33	0.14	16.4	3.32	0.29	...	22	2.0
24	ALMA033224-275334	3 32 24.66	-27 53 34.2	2.47	0.10	22.7	3.25	0.14	...	27	3.2
25	ALMA033243-274639	3 32 43.53	-27 46 39.2	2.54	0.18	13.3	3.18	0.23	0.79	10	3.8
26	ALMA033216-275044	3 32 16.86	-27 50 44.2	2.40	0.19	12.3	3.15	0.25	0.88	...	...
27	ALMA033203-275039	3 32 3.500	-27 50 39.8	2.32	0.14	15.5	3.05	0.19	...	34	1.9
28	ALMA033233-275326	3 32 33.42	-27 53 26.6	2.30	0.29	7.7	2.89	0.37	...	46	2.0
29	ALMA033232-274540	3 32 32.91	-27 45 40.9	1.56	0.13	11.4	2.82	0.28	...	36	3.4
30	ALMA033217-275037	3 32 17.21	-27 50 37.2	2.11	0.11	18.1	2.78	0.15	...	17	2.6
31	ALMA033218-275134	3 32 18.57	-27 51 34.6	1.96	0.19	10.0	2.72 M	0.51	...	51	3.3
32	ALMA033211-274615	3 32 11.94	-27 46 15.4	1.95	0.12	15.9	2.56	0.16	...	16	1.9
33	ALMA033217-275003	3 32 17.45	-27 50 3.40	1.63	0.11	14.4	2.49	0.23	...	25	2.4
34	ALMA033221-274656	3 32 21.78	-27 46 56.9	1.88	0.16	11.5	2.47	0.21	...	...	...

*Table 4 continued*

Table 4 (continued)

No.	Name	R.A.	Decl.	Pk Flux	Error	S/N	Flux	Error	1.13 mm	SCUBA-2	offset
(1)	(2)	J2000.0	J2000.0	(mJy)	(mJy)	(7)	(mJy)	(mJy)	(mJy)	No.	(arcsec)
		(3)	(4)	(5)	(6)		(8)	(9)	(10)	(11)	(12)
35	ALMA033222-274243	3 32 22.01	-27 42 43.7	1.88	0.10	17.9	2.47	0.13	...	...	...
36	ALMA033220-274836	3 32 20.78	-27 48 36.8	1.30	0.12	10.5	2.41	0.25	1.0	...	...
37	ALMA033235-275319	3 32 35.13	-27 53 19.7	1.52	0.13	11.0	2.35	0.28	...	39	1.6
38	ALMA033222-274811	3 32 22.16	-27 48 11.6	2.16	.091	23.5	2.27 M	.090	...	5	4.2
39	ALMA033229-275257	3 32 29.83	-27 52 57.7	1.72	0.14	12.1	2.26	0.18	...	40	1.6
40	ALMA033231-274623	3 32 31.46	-27 46 23.5	1.72	0.13	12.8	2.26	0.17	0.47	37	2.4
41	ALMA033241-275131	3 32 41.47	-27 51 31.8	1.71	0.14	11.8	2.25	0.18	...	42	3.3
42	ALMA033221-275112	3 32 21.99	-27 51 12.2	1.71	0.13	12.4	2.25	0.18	...	54	3.1
43	ALMA033216-275247	3 32 16.52	-27 52 47.0	1.78	0.32	5.4	2.23	0.41	...	28	2.1
44	ALMA033220-275024	3 32 20.91	-27 50 24.7	1.68	.096	17.3	2.21	0.12	...	26	2.9
45	ALMA033209-275015	3 32 9.860	-27 50 15.7	2.05	0.19	10.5	2.20 M	0.23	...	...	...
[46]	ALMA033225-274219	3 32 25.17	-27 42 19.0	1.88	.069	26.9	2.08 M	.085	...	...	...
[47]	ALMA033239-275326	3 32 39.24	-27 53 26.0	1.56	0.11	13.0	2.05	0.15	...	...	...
48	ALMA033238-274634	3 32 38.55	-27 46 34.5	1.63	0.28	5.6	2.04	0.36	1.1	50	0.93
49	ALMA033212-275209	3 32 12.88	-27 52 9.40	1.41	0.11	12.5	1.98	0.23	...	32	0.71
50	ALMA033221-274241	3 32 21.49	-27 42 41.9	1.23	0.22	5.4	1.97	0.45	...	...	...
51	ALMA033216-274344	3 32 16.27	-27 43 44.0	0.85	0.10	7.9	1.94	0.22	...	15	1.5
52	ALMA033215-275145	3 32 15.55	-27 51 45.4	1.20	0.11	10.2	1.88	0.24	...	...	...
53	ALMA033247-275038	3 32 47.73	-27 50 38.2	1.09	0.15	6.9	1.86	0.32	...	23	2.3
54	ALMA033243-274851	3 32 43.67	-27 48 51.1	1.45	0.24	5.9	1.82	0.30	...	...	...
55	ALMA033211-274613	3 32 11.61	-27 46 13.1	1.36	0.11	11.8	1.79	0.15	...	16	3.0
56	ALMA033225-274306	3 32 25.69	-27 43 6.00	1.24	0.16	7.6	1.78 M	0.43	...	47	2.6
57	ALMA033207-274900	3 32 7.950	-27 49 0.40	1.30	0.20	6.4	1.72	0.26	...	...	...
58	ALMA033244-275011	3 32 44.07	-27 50 11.4	1.37	0.24	5.5	1.72	0.31	...	...	...
59	ALMA033222-274815	3 32 22.57	-27 48 15.1	1.43	0.13	10.2	1.66 M	0.13	...	...	...
60	ALMA033229-275335	3 32 29.90	-27 53 35.8	0.73	0.12	5.9	1.61	0.25	...	24	2.9
[61]	ALMA033231-274313	3 32 31.86	-27 43 13.0	1.22	0.19	6.4	1.61	0.25	...	...	...
62	ALMA033219-274315	3 32 19.36	-27 43 15.1	1.20	0.13	8.8	1.59	0.17	...	35	0.29
63	ALMA033228-274829	3 32 28.80	-27 48 29.7	0.76	0.12	5.9	1.57	0.26	...	...	...
[64]	ALMA033228-275229	3 32 28.10	-27 52 29.7	0.82	0.15	5.3	1.53	0.31	...	...	...
65	ALMA033231-275028	3 32 31.55	-27 50 28.9	1.11	0.11	9.7	1.46	0.14	...	44	2.7
66	ALMA033210-274807	3 32 10.73	-27 48 7.29	0.67	0.13	5.1	1.44	0.26	...	...	...
[67]	ALMA033217-274908	3 32 17.28	-27 49 8.40	1.03	0.14	7.0	1.36	0.19	...	...	...
68	ALMA033228-274431	3 32 28.91	-27 44 31.4	1.02	0.18	5.5	1.35	0.24	...	38	2.3
69	ALMA033227-275311	3 32 27.15	-27 53 11.8	0.78	0.13	5.7	1.25	0.27	...	29	1.3
70	ALMA033233-275222	3 32 33.90	-27 52 22.2	0.73	0.12	5.7	1.18	0.25	...	31	3.8

Table 4 continued

**Table 4** (*continued*)

No.	Name	R.A.	Decl.	Pk Flux	Error	S/N	Flux	Error	1.13 mm	SCUBA-2	offset
		J2000.0	J2000.0	(mJy)	(mJy)		(mJy)	(mJy)	(mJy)	No.	(arcsec)
(1)	(2)	(3)	(4)	(5)	(6)	(7)	(8)	(9)	(10)	(11)	(12)
71	ALMA033213-274754	3 32 13.64	-27 47 54.2	0.77	0.14	5.2	1.16	0.30	...	...	...
72	ALMA033228-274435	3 32 28.78	-27 44 35.2	0.75	0.14	5.2	1.11	0.29	...	38	4.1
73	ALMA033234-275226	3 32 34.28	-27 52 26.7	0.81	0.13	6.1	1.07	0.17	...	31	2.8
74	ALMA033222-274935	3 32 22.47	-27 49 35.2	0.55	0.11	4.8	0.93	0.23	...	8	1.9
75	ALMA033217-274713	3 32 17.96	-27 47 13.6	0.64	0.11	5.6	0.84	0.14	...	...	...

NOTE— The columns are (1) ALMA source number, (2) ALMA source name, (3 and 4) ALMA R.A. and Decl., (5, 6, and 7) peak flux, error, and S/N measured from the ALMA images, (8 and 9) best ALMA flux estimates and errors (see text for details), (10) ALMA 1.13 mm flux from F18 based on their GALFIT values and without applying any deboosting, (11) SCUBA-2 counterpart source number from Table 2 (for offsets less than 5''), and (12) offset between the nearest SCUBA-2 source position and the ALMA position for these sources. In Column 1, six ALMA source numbers (20, 46, 47, 61, 64, 67) are in square brackets, since they do not come from the full central SCUBA-2 sample (see Table 3 for description). In Column 8, the four archival sources from Hodge et al. (2013) are marked with an ‘H’, the eight Mullaney et al. (2015) sources with an ‘M’, the Barro source with a ‘B’, and the Schreiber et al. (2017) source with an ‘S’.

**Table 5.** ALMA Redshifts

No.	Name	$m_{850lp}$	$m_{160w}$	$K_s$	$4.5 \mu m$	$8 \mu m$	CANDELS offset (arcsec)	Specz	Photz	FIRz
(1)	(2)	(3)	(4)	(5)	(6)	(7)	(8)	(9)	(10)	(11)
1	ALMA033207275120	...	21.3	20.8	19.8	20.0	0.67	...	...	3.26
2	ALMA033211275212	...	...	23.5	...	...	0.33	...	4.45	3.75
3	ALMA033215275037	...	22.3	21.3	21.1	20.2	0.17	...	3.12	2.80
4	ALMA033204274647	25.1	21.9	21.3	19.7	19.7	0.14	2.252 4	1.95	2.84
5	ALMA033228274658	25.7	22.9	22.2	20.9	20.6	0.08	2.309 7	2.29	2.16
6	ALMA033246275120	23.5	22.7	22.0	20.8	20.2	0.15	...	...	3.11
7	ALMA033238274401	...	24.4	23.3	21.7	20.8	0.15	...	3.48	3.36
8	ALMA033225275230	27.3	23.7	22.7	20.8	20.3	0.10	...	2.69	3.26
9	ALMA033235274916	24.4	22.2	21.7	20.6	19.6	0.11	2.576 5	2.55	2.65
10	ALMA033219274602	...	23.6	22.6	20.7	20.4	0.39	...	2.41	2.78
11	ALMA033219275214	26.0	24.5	23.1	21.5	21.0	0.20	...	...	3.32
12	ALMA033234274940	25.4	24.3	23.5	21.9	21.1	0.05	...	3.76	3.32
13	ALMA033217275233	27.1	26.3	26.3	23.2	22.6	0.47	...	[ 2.73]	3.69
14	ALMA033222274936	26.7	23.9	23.3	21.7	21.2	0.45	...	2.73	2.11
15	ALMA033205274820	...	23.4	22.5	20.8	20.7	0.09	...	2.14	2.96
16	ALMA033219275159	26.9	24.2	22.5	21.2	20.9	0.19	...	3.37	4.34
17	ALMA033235275215	...	26.3	24.5	22.4	21.5	0.13	...	3.57	7.99
18	ALMA033222274804	26.8	24.2	23.7	22.3	21.6	0.31	3.847 8	2.96	3.51
19	ALMA033226275208	...	...	-25.7	23.5	...	...	...	[ 4.47]	6.68
20	ALMA033247274452	24.9	22.4	21.8	20.7	20.8	0.07	...	1.93	2.02
21	ALMA033242275212	26.6	24.7	24.0	22.3	21.3	0.18	...	3.78	4.17
22	ALMA033244274635	24.3	24.8	22.8	21.3	20.7	0.08	...	...	2.60
23	ALMA033237275000	23.3	21.8	20.9	19.9	20.2	0.14	...	1.58	2.03
24	ALMA033224275334	25.4	23.1	22.6	21.1	21.2	0.25	...	1.96	2.11
25	ALMA033243274639	...	24.6	23.6	21.7	21.0	0.13	2.794 8	2.92	3.56
26	ALMA033216275044	25.2	24.3	23.6	22.5	21.7	0.02	...	3.78	...
27	ALMA033203275039	...	...	23.5	22.1	...	...	...	[ 1.78]	4.60
28	ALMA033233275326	...	25.8	24.5	22.1	21.4	0.21	...	[ 3.33]	3.62
29	ALMA033232274540	21.6	20.3	20.0	20.0	20.2	0.06	...	...	...
30	ALMA033217275037	25.2	22.5	21.7	20.5	20.8	0.01	...	1.86	2.74
31	ALMA033218275134	26.9	22.3	21.6	20.3	20.4	0.19	...	1.95	2.85
32	ALMA033211274615	25.8	23.6	23.4	22.2	21.8	0.41	...	2.75	2.52
33	ALMA033217275003	24.1	21.8	21.0	19.9	20.1	0.21	...	1.58	2.09
34	ALMA033221274656	26.1	23.5	22.8	21.0	21.3	0.12	...	1.95	2.23

Table 5 continued



Table 5 (continued)

No.	Name	$m_{850lp}$	$m_{160w}$	$K_s$	4.5 $\mu\text{m}$	8 $\mu\text{m}$	CANDELS offset (arcsec)	Specz	Photz	FIRz
(1)	(2)	(3)	(4)	(5)	(6)	(7)	(8)	(9)	(10)	(11)
35	ALMA033222274243	24.0	22.3	21.7	20.5	20.4	0.18	1.612 7	1.71	2.22
36	ALMA033220274836	26.9	24.1	22.9	21.2	20.9	0.24	...	2.37	3.30
37	ALMA033235275319	...	24.7	23.8	20.9	20.9	0.12	...	2.96	...
38	ALMA033222274811	26.3	23.6	22.6	20.9	20.6	0.05	...	2.31	3.07
39	ALMA033229275257	...	25.0	24.2	22.3	21.6	0.03	...	3.04	2.20
40	ALMA033231274623	22.8	21.3	20.8	20.0	19.1	0.06	2.223 5	2.22	2.53
41	ALMA033241275131	...	26.5	25.4	23.3	22.3	0.34	...	[ 4.13]	...
42	ALMA033221275112	25.6	24.1	23.0	20.8	20.8	0.12	...	2.34	2.61
43	ALMA033216275247	25.8	22.8	22.1	20.8	20.8	0.11	...	2.39	3.01
44	ALMA033220275024	...	...	23.0	22.6	...	...	...	...	5.26
45	ALMA033209275015	...	26.3	25.3	22.6	21.0	0.22	...	[ 7.62]	3.01
46	ALMA033225274219	22.1	21.4	20.2	19.2	18.8	0.11	1.613 1	1.69	1.73
47	ALMA033239275326	25.4	22.8	22.0	20.9	19.5	0.08	...	2.19	2.06
48	ALMA033238274634	24.4	23.3	22.9	21.8	21.3	0.32	2.543 6	2.58	1.85
49	ALMA033212275209	25.9	22.9	21.9	20.4	20.6	0.10	...	1.87	1.91
50	ALMA033221274241	25.2	22.1	21.6	20.1	20.2	0.14	...	1.69	2.59
51	ALMA033216274344	...	23.1	22.7	20.7	20.4	0.28	...	2.32	3.30
52	ALMA033215275145	...	26.7	24.6	22.7	22.0	0.23	...	[ 4.78]	3.66
53	ALMA033247275038	23.7	21.5	20.9	19.7	19.9	0.07	...	1.56	2.08
54	ALMA033243274851	...	25.3	24.1	22.6	20.8	0.05	...	[ 9.42]	1.86
55	ALMA033211274613	22.7	22.9	21.8	21.2	21.3	0.26	...	...	2.77
56	ALMA033225274305	24.8	22.3	21.7	20.2	18.3	0.12	2.299 3	[ 1.55]	2.92
57	ALMA033207274900	...	25.0	24.8	23.1	22.2	0.05	...	3.08	...
58	ALMA033244275011	...	26.1	26.9	22.9	99.0	...	...	[ 4.73]	...
59	ALMA033222274815	25.8	23.2	22.1	20.9	20.8	0.06	...	2.31	...
60	ALMA033229275335	...	23.4	22.7	21.0	20.8	0.05	...	2.53	...
61	ALMA033231274313	...	...	24.7	23.5	...	...	...	[ 4.67]	...
62	ALMA033219274315	25.4	23.7	23.4	21.9	21.4	0.17	...	2.94	...
63	ALMA033228274829	26.3	22.7	21.8	20.3	20.4	0.20	...	1.83	...
64	ALMA033228275229	...	25.5	24.8	23.3	22.6	0.37	...	3.26	...
65	ALMA033231275028	23.9	21.3	20.8	19.7	19.9	0.10	...	1.58	...
66	ALMA033210274807	21.9	20.6	19.9	19.8	19.4	0.05	0.6540 5	0.680	...
67	ALMA033217274908	27.1	23.5	22.6	21.2	21.3	0.19	...	1.69	...
68	ALMA033228274431	27.3	...	23.0	...	...	...	...	...	...
69	ALMA033227275311	26.3	23.1	22.7	21.5	21.2	0.03	...	2.55	...
70	ALMA033233275222	27.9	25.1	23.5	22.3	21.7	0.38	...	3.14	...

Table 5 continued

**Table 5** (*continued*)

No.	Name	$m_{850lp}$	$m_{160w}$	$K_s$	4.5 $\mu\text{m}$	8 $\mu\text{m}$	CANDELS offset (arcsec)	Specz	Photz	FIRz
(1)	(2)	(3)	(4)	(5)	(6)	(7)	(8)	(9)	(10)	(11)
71	ALMA033213274754	23.7	22.0	21.6	20.5	20.7	0.10	...	1.71	...
72	ALMA033228274435	...	25.3	23.7	21.8	20.8	0.16	...	[ 3.76]	...
73	ALMA033234275226	26.1	25.6	22.7	21.8	22.5	0.19	...	2.19	...
74	ALMA033222274935	21.5	20.2	19.6	19.5	19.4	0.10	0.7323 1	0.766	...
75	ALMA033217274713	25.0	...	22.5	...	...	...	...	...	...

NOTE— The columns are (1) ALMA source number, (2) ALMA source name, (3 and 4) *HST* ACS F850LP and WFC3 F160W magnitudes from G13, (5) ground-based  $K_s$  magnitude measured from the image of Hsieh et al. (2012), (6 and 7) *Spitzer* 4.5 and 8  $\mu\text{m}$  magnitudes from Ashby et al. (2015), (8) offset between the ALMA and G13 source positions, (9) specz and reference number (see details below), (10) photz from S16 (poor quality flag  $Q > 3$  estimates are in square brackets to distinguish them from the more reliable  $Q < 3$  estimates; see Section 4.3), and (11) FIRz for the 59 sources with ALMA fluxes above 1.65 mJy. There is no entry in Column (11) for the seven excluded sources (26, 29, 37, 41, 57, 58, and 59) with probability  $< 5\%$  for the  $\chi^2$  fits, as discussed in Section 4.6. In Column 9, ‘1’ indicates the redshift is from our own Keck DEIMOS observations, ‘2’ from K20 (Mignoli et al. 2005), ‘3’ from MOSDEF (Kriek et al. 2015), ‘4’ from Casey et al. (2012), ‘5’ from Szokoly et al. (2004), ‘6’ from Inami et al. (2017), ‘7’ from Kurk et al. (2013), and ‘8’ from F18 (private communications from Mobasher and Brammer).

**Table 6.** Candidate High-Redshift ALMA Sources Above 1.65 mJy

No.	Name	$f_{850\ \mu\text{m}}$ (mJy)	$f_{4.5}/f_{850}$	$f_{24}/f_{850}$	$f_{100}/f_{850}$	$f_{250}/f_{850}$	$\log f_{2-7\ \text{keV}}$ ( $\text{erg cm}^{-2}\ \text{s}^{-1}$ )	Photz	FIRz
(1)	(2)	(3)	(4)	(5)	(6)	(7)	(8)	(9)	(10)
2	ALMA033211275212	8.83	0.00069	0.011	0.113	1.81	...	4.45 (4.02 - 4.74)	3.75 (3.30 - 4.71)
16	ALMA033219275159	3.91	0.0030	0.0039	0.0309	1.50	-15.8	3.37 (3.08 - 3.61)	4.34 (4.23 - 4.50)
17	ALMA033235275215	3.80	0.00097	0.0069	0.0243	0.179	-15.4	3.57 (3.29 - 4.09)	7.99 (5.79 - 7.99)
19	ALMA033226275208	3.62	0.00038	0.0024	0.0847	0.287	-16.0	4.47 (3.60 - 6.63)	6.68 (5.07 - 7.99)
21	ALMA033242275212	3.55	0.0011	0.0047	0.140	1.79	...	3.78 (3.48 - 4.07)	4.17 (3.05 - 5.50)
27	ALMA033203275039	3.05	0.0016	0.011	0.163	1.12	...	1.78 (1.50 - 4.21)	4.60 (3.05 - 5.79)
44	ALMA033220275024	2.21	0.0013	0.0057	0.198	1.08	...	...	5.26 (3.23 - 7.26)

NOTE— The columns are (1) ALMA source number, (2) ALMA source name, (3) ALMA 850  $\mu\text{m}$  flux, (4-7) 4.5, 24, 100, and 250  $\mu\text{m}$  to 850  $\mu\text{m}$  flux ratios, (8) logarithm of the observed 2 – 7 keV flux, (9) photz and 95% confidence range, and (10) FIRz and 95% confidence range.

**Table 7.** Hard Band Detected X-ray Subsample of 21 Sources

No.	Name	Luo+17	$f_{850\ \mu\text{m}}$ (mJy)	$\log L_{8-28\ \text{keV}}$ ( $\text{erg s}^{-1}$ )	$\Gamma$	Spectral Class
(1)	(2)	(3)	(4)	(5)	(6)	(7)
1	ALMA033207-275120	161	8.93	43.1	0.47	...
9	ALMA033235-274916	665	5.09	43.2	0.51	Type 2
16	ALMA033219-275159	355	3.91	43.2	0.95	...
17	ALMA033235-275215	656	3.80	44.3	0.10	...
19	ALMA033226-275208	471	3.62	43.4	0.11	...
22	ALMA033244-274635	804	3.38	43.4	1.9	...
26	ALMA033216-275044	298	3.15	42.8	0.85	...
34	ALMA033221-274656	385	2.47	43.0	0.83	...
38	ALMA033222-274811	392	2.27	43.6	0.49	...
40	ALMA033231-274623	586	2.26	42.9	0.83	SF
42	ALMA033221-275112	386	2.25	43.3	0.22	...
45	ALMA033209-275015	194	2.20	43.4	0.85	...
46	ALMA033225-274219	448	2.08	43.7	1.8	Type 2
47	ALMA033239-275326	738	2.05	43.2	0.11	...
53	ALMA033247-275038	853	1.86	43.5	0.53	...
54	ALMA033243-274851	801	1.82	42.1	0.19	...
56	ALMA033225-274305	457	1.78	44.2	1.0	...
59	ALMA033222-274815	400	1.66	42.7	0.48	SF
65	ALMA033231-275028	587	1.46	42.6	.017	...
66	ALMA033210-274807	202	1.44	41.1	0.88	SF
67	ALMA033217-274908	309	1.36	42.2	0.92	...

NOTE— The columns are (1) ALMA source number, (2) ALMA source name, (3) corresponding Luo et al. (2017) X-ray catalog source number, (4) ALMA 850  $\mu\text{m}$  flux, (5) logarithm of the 8 – 28 keV luminosity, (6) photon index  $\Gamma$ , and (7) classification from spectroscopy.